Chair of Petroleum and Geothermal Energy Recovery

Master Thesis

Frequency-Elastic Operations of Sucker Rod Pumps

Energy Efficiency, Start-up and Rod Load Optimization

Written by:
Philipp Knauhs, BSc
0914560

Advisor:
Univ.-Prof. Dipl.-Ing. Dr.mont. Herbert Hofstätter
Dipl.-Ing. Dipl.-Ing. Dr.mont. Clemens Langbauer
Dipl.-Ing. Patrick Bürßner, MBA

Leoben, 03.03.2017

EIDESSTATTLICHE ERKLÄRUNG

Ich erkläre an Eides statt, dass ich die vorliegende Diplomarbeit selbständig und ohne fremde Hilfe verfasst, andere als die angegebenen Quellen und Hilfsmittel nicht benutzt und die den benutzten Quellen wörtlich und inhaltlich entnommenen Stellen als solche erkenntlich gemacht habe.

Datum

Unterschrift

AFFIDAVIT

I hereby declare that the content of this work is my own composition and has not been submitted previously for any higher degree. All extracts have been distinguished using quoted references and all information sources have been acknowledged.

Acknowledgement

I would like to thank all the people who contributed in some way to my work and made it possible for me to write this Master Thesis:

Foremost, I would like to express my sincere gratitude to my supervisor Prof. Hofstätter, for his engagement, guidance and continuous support along my studies, especially during this thesis.

Furthermore, I am very grateful to Dr. Clemens Langbauer for helping me with the methodical approach of this work and introducing me to his simulation software. I want to thank him for his time, support and insightful comments.

My sincere thanks also go to OMV for their financial support and the opportunity to carry out my research at their branch office in Gaenserndorf. In particular, I would like to thank Dipl.-Ing. Patrick Bürßner and his team of the Production Technology Department for providing me the topic of my thesis as well as their encouragement, knowledge and great contribution to my work.

Last but not least, I would like to thank my family and friends, especially my parents Maria and Johann Knauhs who enabled my studies and supported me throughout my life, as well as my sister Stefanie Luegger who was always an inspiring role model for me.

Kurzfassung

Die große Menge an Energieverlusten ist eines der größten Defizite von Gestängetiefpumpen und führt dazu, dass der Energieverbrauch und folglich die Betriebskosten von ölfördernden Unternehmen in die Höhe getrieben werden. Angesichts dessen bietet diese Arbeit eine exakte Analyse der Arbeitsweise und Leistung von Gestängetiefpumpen. Basierend auf dem Verlauf von Polierstangenlast und Energieverbrauch wird ein optimiertes Verfahren entwickelt, das die Antriebsgeschwindigkeit der Pumpe während eines Hubs verändert und somit die Effizienz des Systems verbessert. Für die Durchführung dieses optimierten Verfahrens wird ein Geschwindigkeitsprofil mit Hilfe von harmonischen Funktionen entworfen, das die Verwendung eines Frequenzumrichters voraussetzt. Es wird bewiesen, dass diese Methode für niedrige bis mittlere Pumpgeschwindigkeiten technisch realisierbar ist und zu mehreren Verbesserungen des Systems führt. Zum Vergleich werden für die herkömmliche und die optimierte Arbeitsweise Simulationen mit verschiedenen Pumpgeschwindigkeiten, Ausgleichsgewichtspositionen und Motoreinstellungen durchgeführt und die Ergebnisse untereinander verglichen. Für eine Ölsonde, mit einer durchschnittlichen Pumpgeschwindigkeit von 5 Hüben pro Minute, kann die Spitzenlast an der Polierstange um 2 % und der Energieverbrauch um bis zu 37 % verringert werden. Dies führt zu einer Anhebung des Systemwirkungsgrad von 24 % auf 38 %. Darüber hinaus kann die Belastung von Motor und Getriebe um bis zu 23 % reduziert werden. Abschließend werden in dieser Arbeit die derzeitigen Anfahrvorgänge von Gestängetiefpumpen untersucht, die bei der Erstinbetriebnahme und nach Sondenbehandlungen verwendet werden. Basierend auf Förder- und Flüssigkeitsdaten wird ein optimiertes Verfahren entwickelt, das mit Hilfe eines Frequenzumrichters die Pumpgeschwindigkeit in Form einer linearen Rampe erhöht und somit die Wahrscheinlichkeit von Sandförderung und sofortigem Gerätebruch verringert.

Abstract

The large amount of energy losses along the system of a sucker rod pump is one of the key disadvantages of this artificial lift method, which dictates the energy consumption and drives up operational expenditures for oil producing companies. Therefore, this thesis will give a thorough investigation on the operation and performance of a sucker rod pump. Based on the distribution of polished rod loads and energy consumption, an optimized process is developed that alters the drive speed within each stroke to increase the energy efficiency of the system. The velocity profile is designed with harmonic functions and its implementation requires the installation of a VSD controller. This thesis shows that this method is technically feasible for low to intermediate pumping speeds and leads to several improvements of the sucker rod pumping system. Conventional and optimized operations are simulated and compared with one another in regards to different pumping speeds, counterweight settings and motor setups. Considering a sample well with an average pumping speed of 5 spm, the peak polished rod loads can be reduced by 2 % and the energy consumption by up to 37 %. This raises the overall efficiency of the system from 24 % to 38 %. Moreover, the loading of the gear reducer and electric prime mover is decreased by up to 23 %. In addition, this thesis will analyse current start-up procedures of sucker rod pumps that are carried out at the beginning of operations or after a well intervention. In virtue of operational and fluid data, an enhanced method is provided, implying a VSD controlled start-up ramp of the pumping speed, to reduce the risks of sand production and immediate equipment failure further.

List of Tables

List of Figures

Abbreviations

2Q	Two-Quadrant
4Q	Four-Quadrant
AC	Alternating Current
ALS	Artificial Lift System
API	American Petroleum Institute
CFD	Computational Fluid Dynamics
DC	Direct Current
DIN	Deutsches Institut für Normung
ESP	Electrical Submersible Pump
FS	Full Size
GB	Gearbox
GL	Gas Lift
GRG	Generalized Reduced Gradient
HP	Horsepower
IGBT	Insulated Gate Bipolar Transistors
KOP	Kickoff Point
LRP	Linear Rod Pump
Max	Maximum
Min	Minimum
NEMA	National Electrical Manufacturers Association
p./pp.	page/pages
PCP	Progressive Cavity Pumps
PRHP	Polished Rod Horsepower
PRL	Polished Rod Load
PWM	Pulsed-width Modulation
SB	Saddle Bearing
SH	Slim Hole
Spec.	Specification
SRP	Sucker Rod Pump
STD	Standard
TP	Turning Point
TVD	True Vertical Depth
TWC	Thick Wall Cylinder
UCS	Unconfined Compressive Strength
VSD	Variable Speed Drive

Table of Content

Page

1 Introduction

1.1 General Introduction

In the petroleum industry, artificial lift systems (ALS) are applied to provide additional energy to the wellbore when the reservoir loses its ability to let liquids flow naturally to the surface or a higher production rate is desired. In general, a naturally flowing wellbore means that the bottomhole pressure is high enough to overcome the pressure losses along the wellbore to ensure free flow from the reservoir to the surface. Over the lifecycle of a production well this pressure will constantly decrease, mainly due to reservoir depletion, until one point in time the production will stop and the well stops free flowing. These circumstances require the usage of an ALS that adds energy, in the form of pressure, to the well either by mechanical means or by injecting compressed gas. Frequently installed methods include Electrical Submersible pumps (ESP), Hydraulic pumps, Progressive Cavity pumps (PCP), Sucker Rod pumps (SRP) and Gas Lift (GL). The selection process depends on several factors such as production rate, fluid properties, wellbore trajectory, required pressure, infrastructure of the field as well as costs, which need to be checked for each well individually. An overview of each method's share in the world's total oil production is shown in Figure 1. [1] [2, p. 1]

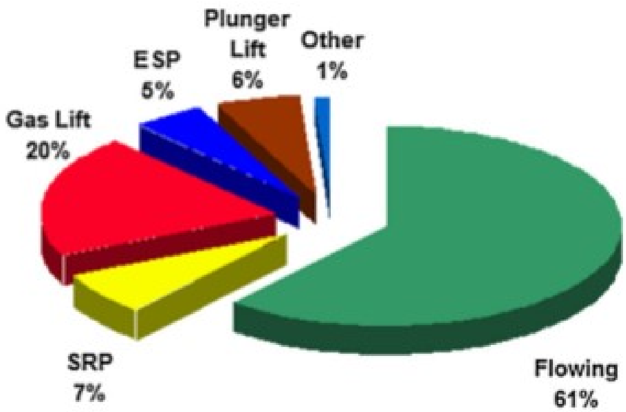

Figure 1: Share in the World's Total Oil Production of Different ALSs [3, p. 4]

The main emphasis of this thesis will be on SRPs, known as the oldest and most widely used artificial lift method. The origins of this method go back many centuries when the Chinese used a similar approach to pump drinking water to the surface, however the first dated usage as a lifting technique for the oil production lies a bit more than a century back in the past and occurred shortly after the birth of the petroleum industry. Over all these years the basic principle of sucker rod pumping remained the same and it is still the most applied ALS, with a rising tendency. Nowadays, it is assumed that three out of four production wells are driven by

SRPs, with a total number of more than 600,000 installations worldwide. Compared to other techniques, its popularity comes mainly from the simple system design and the low operating and capital investment costs. [3, p. 7] [4]

1.2 Problem Definition

Despite their high popularity and small operational expenditures, SRPs have some major shortcomings that leave space for improvement and challenge the petroleum industry to put continually efforts into analysing the existing system and researching for enhancements. One of the biggest problems of a sucker rod pumping system is the moderately efficient energy usage which is reflected by the large difference in electrical power, fed into the system, and hydraulic power, actually needed for lifting wellbore fluids to the surface. This is caused by energy losses developing along the whole system, starting at the power supply and ending at the subsurface pump. These inefficiencies arise in both downhole and surface equipment and consist of electrical, mechanical, hydraulic and friction losses, as illustrated in Figure 2. Any attempt to increase the overall energy efficiency, requires therefore a perfect understanding of all SRP components, such as the prime mover, the pumping unit, the rod string and the subsurface pump, as well as the nature and magnitude of their energy losses. With an economic situation of constantly increasing electricity costs and oil prices at a low level, an industry-wide trend can be observed, calling for cutting down operational expenditures by reducing energy losses and increasing the efficiency of SRP systems. As a comparison, the system efficiencies of different ALSs is illustrated in Figure 3 [3, pp. 359-365]

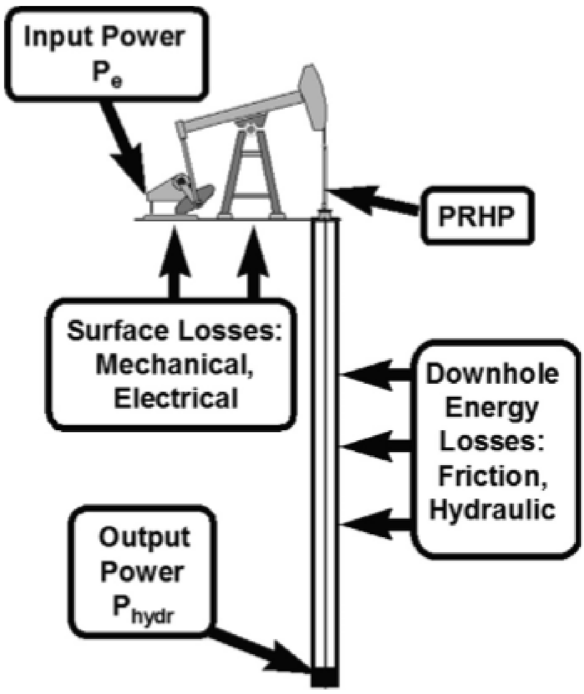

Figure 2: Energy Losses occurring in a Sucker Rod Pumping System [3, p. 360]

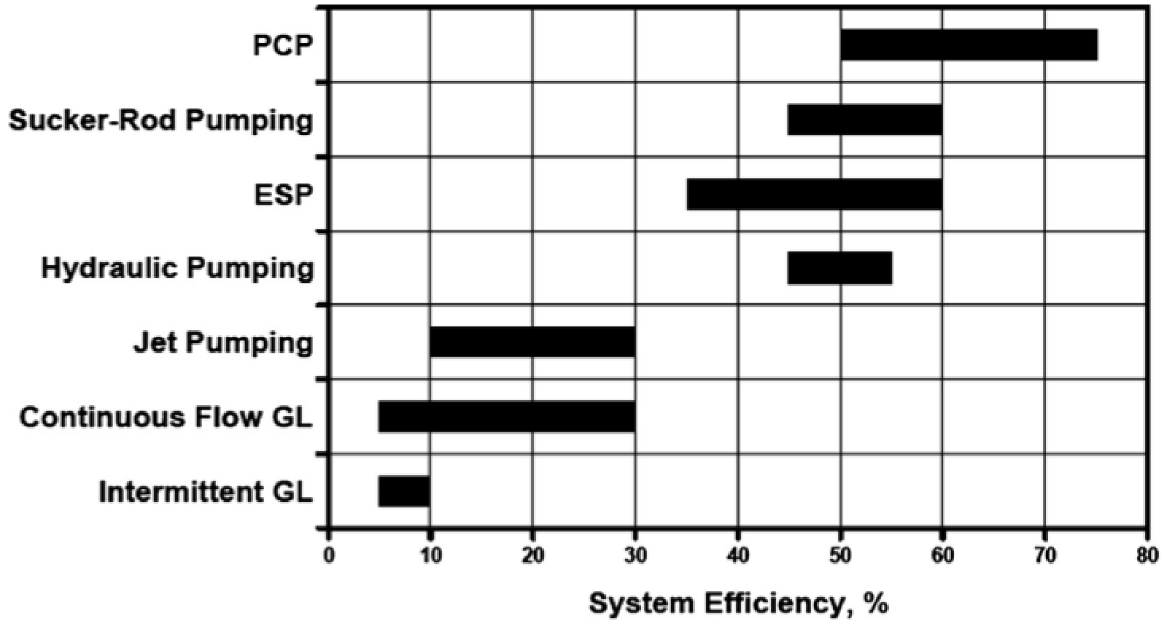

Figure 3: System Efficiencies of Different ALSs [3, p. 6]

1.3 Objective of this Master Thesis

The main ambition of this work is to provide an answer to the stated problem and improve the energy efficiency of a SRP. This is achieved by equipping the system with a variable speed drive and operating the electric motor frequency-elastic, meaning that the drive speed of the SRP is altered within each stroke. To optimize the course of the instantaneous pumping speed and point out the potential for improvement, it is necessary to set up an integrated model describing the whole sequence of the pumping operation, from the subsurface pump to the electric prime mover, and predict the energy consumption of the system. The major elements of this approach are the kinematic analysis of the pumping unit by Svinos, the description of the dynamic behaviour of the rod string, with a one-dimensional damped wave equation by Gibbs as well as the calculation of gearbox torques considering counterbalance and inertial effects by Takacs. This model is applied on a sample well provided by OMV Austria GmbH and based on the development of polished rod loads and energy consumption during one stroke, a drive speed function is designed, in consideration of each component's technical limitation, to reduce these two parameters. Several scenarios are then performed, including different pumping speeds, counterweight settings and motor setups, to demonstrate the increase in energy efficiency and evaluate the profitability, compared to conventional pumping operations. In addition, the model is updated by using the sucker rod string simulation software of Langbauer, to achieve a more exact prediction of the polished rod loads. Finally, this thesis will also provide a solution approach to eliminate the high risks of initiating sand production during the start-up of a sucker rod pumped well, by installing a VSD controller and continuously increasing the pumping speed in small steps.

2 Fundamentals

2.1 Sucker Rod Pumping

A sucker rod pumping system can be divided into two different groups of equipment. On the one hand, the surface equipment includes the prime mover, the gear reducer, the pumping unit, the polished rod and the wellhead. On the other hand, the downhole equipment includes the rod string and the downhole pump.

2.1.1 Surface Equipment

An overview of the most important components related to the surface equipment of a sucker rod pumping system is shown in Figure 4.

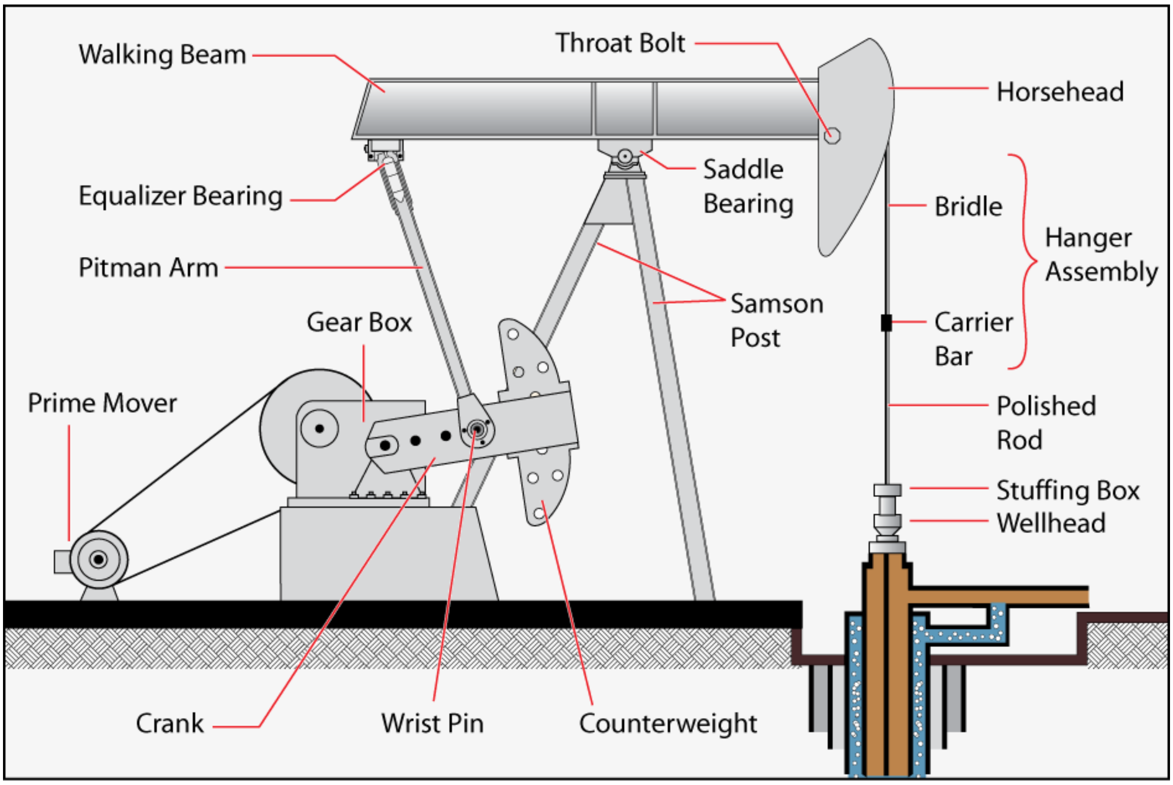

Figure 4: Surface Equipment of a Sucker Rod Pumping System [5, p. 4]

2.1.1.1 Prime Mover

The first component is the prime mover that generates the required mechanical power in the system. In general, two different prime movers are used for sucker rod pumping, electric motors or gas engines. The main selection criteria are the availability of gas or electricity at the well site, operational and investment costs as well as maintenance. The purchase costs of electric motors are lower than the ones for a gas engine, but a shorter operating life needs to be expected. Gas engines are of particular interest, when the gas comes directly from the wellbore. This can save an enormous amount of money, together with the constant increase of electricity costs in recent days. This thesis concentrates on sucker rod pumps driven by electric motors that are explained in detail in chapter 2.2. [6]

2.1.1.2 Gear Reducer and V-Belt Drive

The main function of a gear reducer is to convert the high rotational speed of the prime mover to the required pumping speed and deliver the torque demands of the pumping system. The gearbox and the prime mover are connected to each other by a V-belt assembly, consisting of two sheaves of different sizes and a belt drive. The large difference in size between the sheave mounted on the prime mover and the one on the gearbox leads to a further reduction in speed. A typical gearbox itself consists of three different shafts, the high speed shaft, the intermediate shaft as well as the slow speed shaft, and two gears of different size. The arrangement of the gearbox, seen in Figure 5, reduces the input speed from the V-belt in two steps to the desired output speed of the crank arms and converts it to torque.

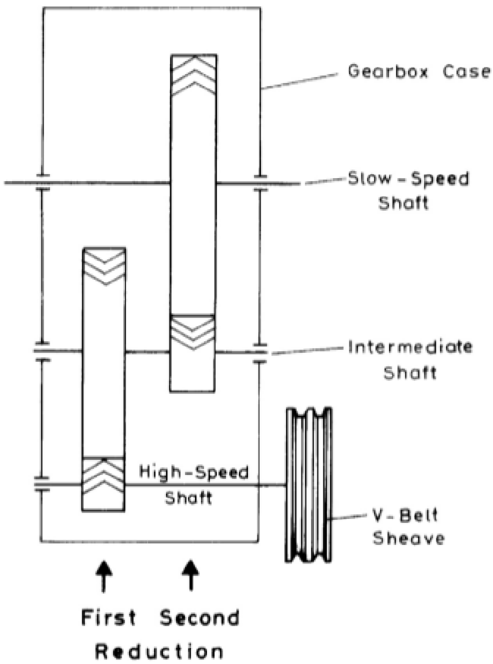

Figure 5: Sketch of a Double-reduction Gearbox [3, p. 227]

The speed reduction ratio depends on the size of the gears and ranges between 28 and 35 to 1. Since the gear reducer contributes more than half of the costs of the surface equipment, a proper operation and maintenance is essential. An important aspect is the lubrication of all moving parts. Therefore the gears are dipped into an oil bath at the bottom of the gearbox and distribute it while turning. At pumping speeds below 5 spm, the gears might rotate too slowly to ensure sufficient lubrication, which requires the installation of specially designed wipers. For even lower pumping speeds, below 2 spm to 3 spm, a lubrication pump has to be installed. [3, pp. 226-228] [7, pp. 45-48]

2.1.1.3 Pumping Unit

The objective of the pumping unit itself is to convert the rotary motion of the gearbox into the oscillating movement needed at the polished rod. Basically a distinction is made between four different types of pump jacks based on their geometrical arrangement: Conventional, Air balanced, Mark II and Reverse Mark units. However, since conventional pumping units are by far the most common and cheapest ones, this work will only concentrate on them. The basic concept of a conventional pumping unit can be compared to a four-bar linkage problem with the walking beam acting as a double-arm lever. The two rotating crank arms are fixed on both sides of the gearbox and are driven by the slow speed shaft. The pitmans are connected at the bottom end to the crank arms via wrist pins and at the upper end to the walking beam via the equalizer bearing. The walking beam is placed on the saddle bearing of the Samson Post with the equalizer bearing at one end and the horsehead at the other end and moves up and down like a seesaw. The special form of the horsehead ensures that the motion of the polished rod, which is connected by the wireline hanger and the carrier bar, is strictly vertical. Most pumping units are additionally equipped with adjustable counterweights mounted on the crank arms. Their purpose is to counteract the torque required to lift the rod string and therefore reduce the energy consumption and the loading of the gearbox. [8, pp. 488-489]

The exact geometry and dimensions of a pumping unit are standardized and depend on five different parameters: The type of the pumping unit, the maximum allowable torque at the gear reducer, the type of the gear reducer, the maximum polished rod load and the maximum polished rod stroke. These factors can be summarized to the unit's designation code as seen in Figure 6.

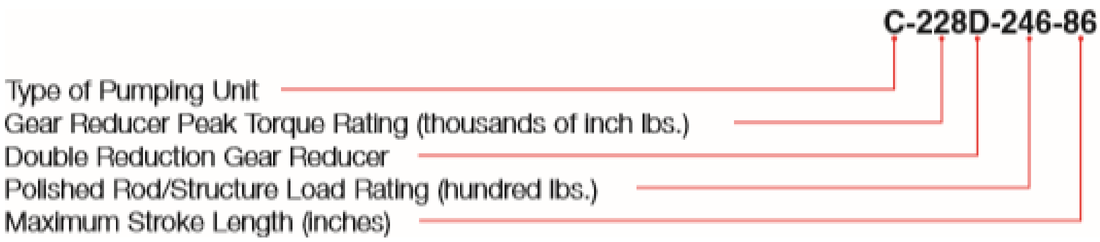

Figure 6: Example of a Pumping Unit's Designation Code [7, p. 69]

2.1.1.4 Polished Rod and Stuffing Box

The polished rod is the linkage between the surface and downhole equipment. It is located at the top of the rod string and transmits the vertical movement from the walking beam to the rod string and the loads from the pumping operation to the pumping unit. At the top of the polished rod, a rod clamp is fixed allowing the pump jack to lift the whole rod string via the wireline hanger and the carrier bar. In general, the polished rod is designed with a quarter inch larger diameter than the rod string beneath due to the fact that the loads acting at the polished rod are the highest. In addition, the surface of the polished rod is very smooth with a sprayed-metal coating to provide sufficient sealing to the wellhead. The counterpart of the polished rod, in terms of sealing, is the stuffing box. It is located at the top of the wellhead, where the polished rod enters the wellbore and is designed to prevent any fluids leaking to the atmosphere. The sealing is achieved by the usage of specially designed packing rings made out of rubber that fit perfectly to the polished rod. Since the sealing is one of the weakest links of the system, the packing rings require a special lubrication and need to be adjusted or replaced on a regular basis. [3, pp. 185-187, 197-198]

2.1.2 Downhole Equipment

The major parts of a sucker rod pumping system, in terms of downhole equipment, are the rod string, auxiliary equipment attached to the string and a positive displacement pump of the cylinder and piston type.

2.1.2.1 Rod String

The rod string serves as the mechanical linkage between the surface unit and the downhole pump and consists of several individual sucker rods. The length of one sucker rod ranges between 25 and 30 ft and the required amount depends on the setting depth of the downhole pump. Most commonly used at OMV Austria, are Grade D steel rods with diameters from ¾” FS (Full Size) to 1” SH (Slim Hole) that are threaded at both ends and put together with spray metal couplings. The two ends of a sucker rod are shown in Figure 7, with one end already connected to the coupling. The wrench square is specially designed to allow the usage of power tongs.

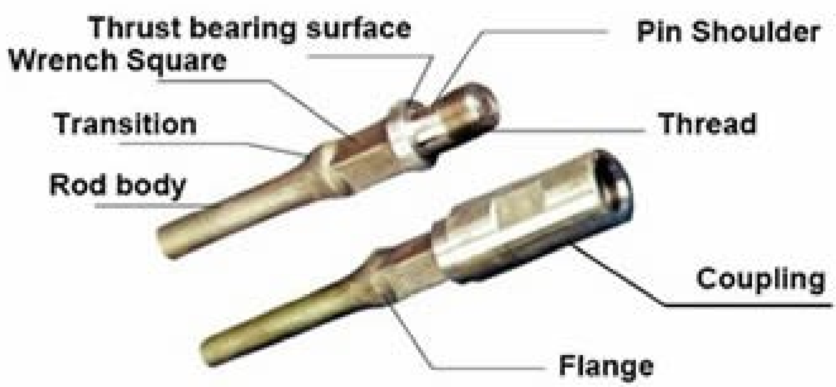

Figure 7: Construction Details of the Sucker Rod End [9]

The material of the sucker rods depend on the required tensile strength as well as the properties of the produced fluids. Steel sucker rods contain iron and a couple of different alloying elements such as carbon, manganese or sulphur. The exact composition and the resulting tensile strength and corrosion resistance are standardized by API Spec. 11B [10]. Grade D rod steels for example consist of chrome molybdenum alloy with a tensile strength of 115,000 psi (793 N/mm²) and a moderate corrosion resistance. The most important design criterion is to ensure safe operations without the failure of the rod string. In general two forms of failure can be observed, tensile and fatigue failures. Tensile failures are abrupt breaks of the rod string when the dynamic loads exceed the tensile strength of the rod material. However, fatigue failures are more difficult to predict since they develop over a longer period of time and occur at dynamic loads below the tensile strength. They may be caused by the cycling loading of the rod string, wear, corrosion, buckling or a combination of those. A proper way to define the fatigue endurance limits is to use the modified Goodman diagram, where the allowable stress is indicated as a function of the tensile strength of the rod material and the minimum rod stress, as shown in **eq.1** [3, p. 155].

$$S_a = SF\ \left(\frac{T_a}{4} + 0.5625\ S_{min}\right) \qquad (1)$$

Additionally the formula includes a safety factor SF that accounts for the corrosiveness of the environment. As an example, Figure 8 shows the modified Goodman diagram for various steel sucker rod grades and a non-corrosive environment, with the stresses being stated in kilo pounds per square inch (ksi). [8, pp. 473-476]

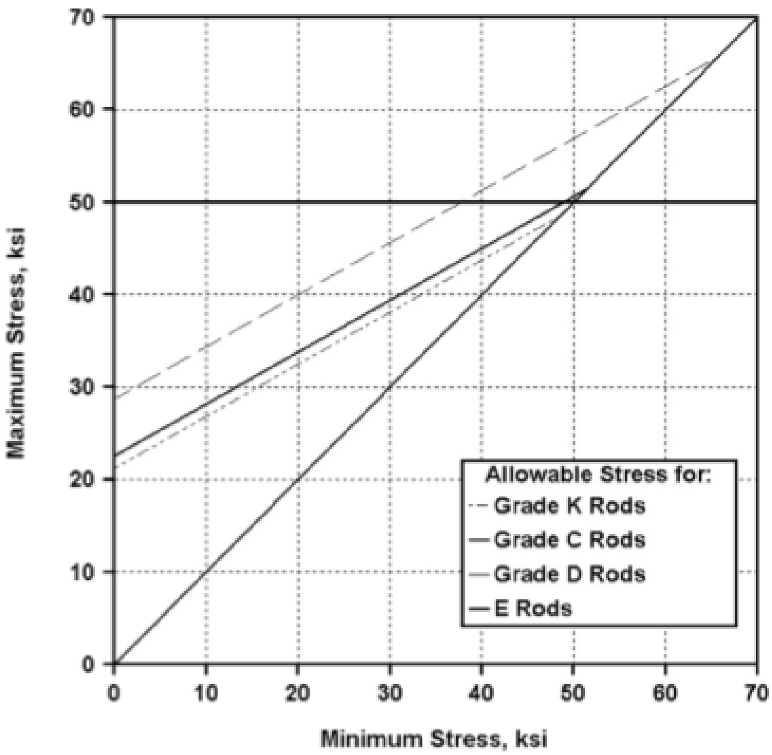

Figure 8: Modified Goodman Diagram for Various Rod Grades [3, p. 157]

2.1.2.2 Auxiliary Equipment

Auxiliary equipment can be installed together with the rod string to enhance the pumping operation and reduce the potential of immediate and fatigue failures. Rod guides are placed in suitable intervals on the rod string, mostly two to four per sucker rod, and minimize the effects of mechanical rod-tubing friction. This can be achieved by keeping the rod string in a centralized position, which is of major importance especially in deviated wells, and using a low friction material such as polyamide. Rod guides not only reduce the effects of wear but also the risks caused by paraffin deposition, based on the special form of the guide that acts as a scraper. Sinker bars are heavy weight sucker rods, achieved by the selection of a different material or a larger diameter, and are placed at the bottom of the rod string above the downhole pump. OMV Austria for instance uses 1 ¾” or 2” sinker bars that are 6 m long and made out of C65 low carbonate steel. Their major purpose is to keep the whole rod string in tension and prevent the effects of buckling, a sinusoidal deformation of the lower part of the rod string when the loading changes from tension to compression. These effects occur mainly during the downstroke and might lead to immediate breaks or a decreased fatigue endurance. [8, pp. 484-486]

2.1.2.3 Downhole Pump

The subsurface pump consists of four major elements. The stationary part of the pump is the cylinder and is attached to the lower end of the tubing string. The moving part of the pump is the piston or also called pump plunger and is connected directly to the rod string.

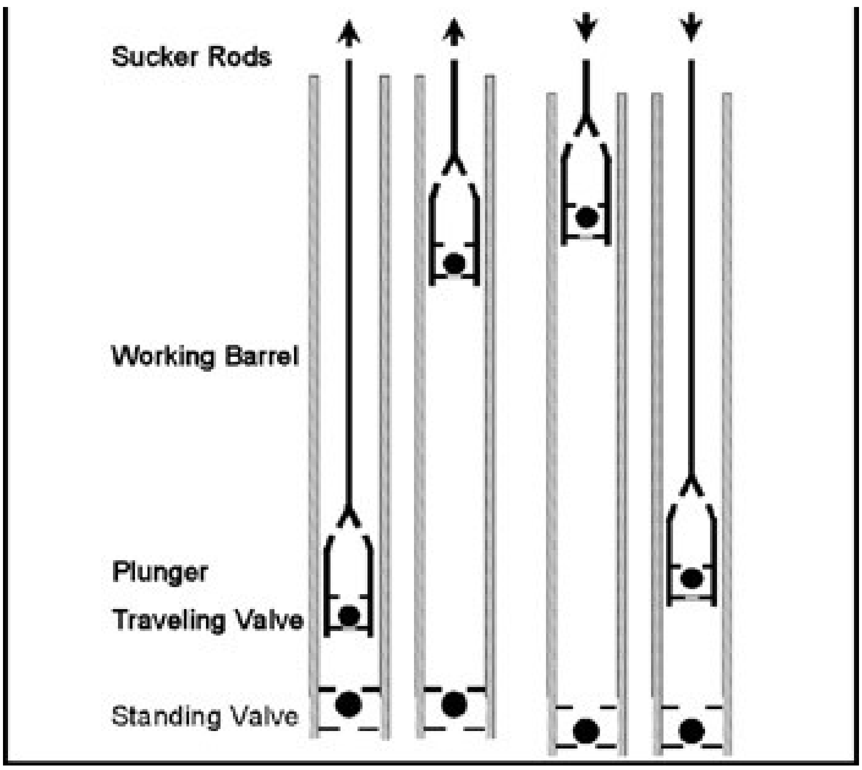

Figure 9: Stages of the Pumping Cycle [11, p. 1]

Additionally, these two components contain two ball valves that are restricted in their movement by cages. The first one is the standing valve that is fixed to the barrel and acts as a suction valve during the upstroke by allowing fluids to enter the pump. The second one is the travelling valve that is fixed to the plunger and is responsible for lifting the fluid column above the pump. A schematic of the different stages of the pumping process is shown in Figure 9.

The pumping cycle starts with the upwards movement of the pump plunger. The travelling valve gets closed by the weight of the fluids above the plunger and starts lifting the liquid column. At the same time, the standing valve opens, caused by the underpressure between the valves, and allows new formation fluids to enter the downhole pump. After the top of the stroke is reached, the pump plunger starts moving downwards again and the traveling valve opens. Consequently, the standing valve gets now closed by the weight of the liquid column and the trapped fluids are pushed through the travelling valve above the pump plunger. [12]

Basically, there are two different types of subsurface pumps, tubing pumps, where the stationary pump barrel is integrated to the tubing string, and insert pumps, where the whole pump is run on the rod string and placed on a seating nipple in the tubing string. The major differences are the larger volumes that can be pumped with a tubing pump and the less extensive pulling out of an insert pump. The classification of subsurface pumps is standardized according to API Spec 11AX [13], with the following designation serving as an example:

$$25 - 175\ \mathrm{RHAC} - 21 - 4$$

The first two numbers are codes describing the nominal tubing size and the pump bore size. The four letters indicate the basic type of the pump, the type of the barrel as well as the position and type of the seating assembly. Finally, the last two numbers give the length of the barrel and the plunger. So in this case the nominal tubing size is 2 7/8 in and the inside diameter of the barrel is 1 ¾ in. The subsurface pump is an insert pump with a heavy-wall barrel and a cup-type seating assembly at the top. The length of the barrel and the plunger is 21 ft and 4 ft, respectively. [8, pp. 465-467]

2.2 Electric Prime Mover

The most common type of electric prime movers used in the petroleum industry for driving a SRP is a three-phase squirrel cage induction motor with six poles. The power supply at OMV Austria comes from a 50 Hz AC line with a voltage of 400 V. The popularity of these prime movers is mainly caused by their relatively low purchase costs and their high efficiency and reliability. [14]

2.2.1 Functionality of the Induction Motor

Basically the induction motor consists of a stationary stator fed with the AC current from the power line and a turnable rotor that transmits the rotary movement to the motor shaft, both wrapped with windings. The AC power supplied to the stator generates a magnetic field that rotates in time with the oscillations of the current. This magnetic flux induces an opposing AC current in the squirrel cage rotor, which in turn creates a magnetic field in the rotor acting against the stator field. The poles of the two magnetic fields are attracted and repelled by each other, forcing the rotor to turn and transmit continuous rotation to the motor shaft. The rotational speed of the magnetic field depends on the number of pole-pairs in the stator and frequency of the AC power and is called the synchronous speed of the motor, given in **eq.2** [15] in revolutions per minute.

$$\mathrm{N_{syn}} = \mathrm{f}\left(\frac{2}{\mathrm{p}}\right) 60 \qquad (2)$$

Since rotation of the rotor at the synchronous speed would result in no electromagnetic induction, the rotational speed that can be transmitted to the motor shaft is always slower. The difference between the synchronous speed and the actual speed of the motor is called slip and is always stated as the ratio between the speed difference and the synchronous speed, as seen in **eq.3** [15].

$$\mathrm{s} = \frac{\mathrm{N_{syn}} - \mathrm{N_{mot}}}{\mathrm{N_{syn}}} \qquad (3)$$

The performance of a motor depends on the selected motor type and is mainly characterized by the relationship between the motor speed and the produced torque. In general there are three different types of motors, NEMA B, C and D, with NEMA D motors being the most common used for sucker rod pumping. This is based on the fact that the breakaway torque that is needed for starting the pumping operation equals the peak output torque and reaches the highest value with 275 % of the rated motor torque. In addition, the high slip factors of NEMA D motors increase the motor speed variation and consequently the inertial effects of the rotating components of the pump jack, which has a favourable impact on the gearbox torques and motor currents. An overview of the main features of the three different motor types is given in Table 1 and the produced motor torque as a function of motor speed can be seen in Figure 10.

Table 1: Comparison of NEMA B, C and D Motors

Motor Type	**Slip Factor**	**Breakaway Torque**	**Maximum Torque**	**Full Load Efficiency**
NEMA B	below 3%	100-175 %	175-300 %	above 92%
NEMA C	5%	200-250 %	190-225 %	above 90%
NEMA D	5-8%	275 %	275%	above 88%

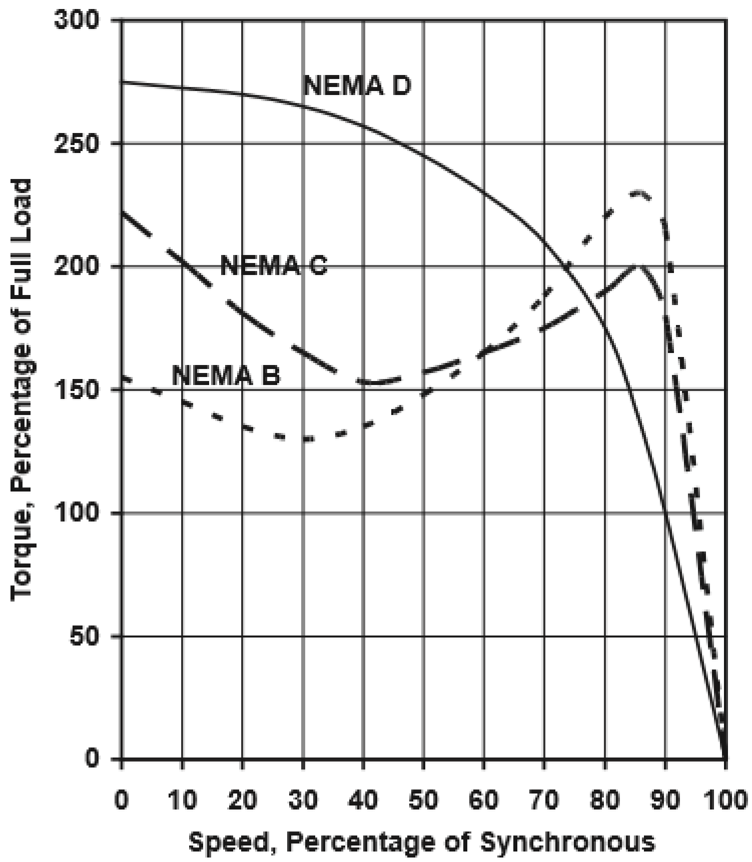

Figure 10: Motor Torque as a Function of Motor Speed [3, p. 238]

The most frequently installed electric prime movers at OMV Austria are NEMA D motors with a rated power output between 9 and 65 kW and therefore the main focus of this thesis. An illustration of the quality performance curves of this motor type is given in Figure 11 by showing the motor torque, motor current and motor efficiency as a function of the motor speed.

The torque output of a NEMA D motor is constantly decreasing from the breakaway torque at standstill conditions to zero torque at the synchronous speed. At the rated speed, which is indicated by the synchronous speed minus the slip, the produced torque equals the rated torque of the motor. As the motor torque, the motor current decreases with increasing motor speed, while the efficiency of the motor increases from zero to maximum efficiency reached at the rated speed and then drops abruptly to zero at the synchronous speed. In case the motor gets driven by the well load and switches to generator mode, the motor turns faster than the synchronous speed and generates negative torques. This indeed generates electric power that can be fed back into the supply system or the process is prevented with regenerative braking by clamping ratchets on the motor. A motor with regenerative braking is called two-quadrant (2Q) drive and a motor with energy recovery four-quadrant (4Q) drive. [3, pp. 235-240] [15] [16]

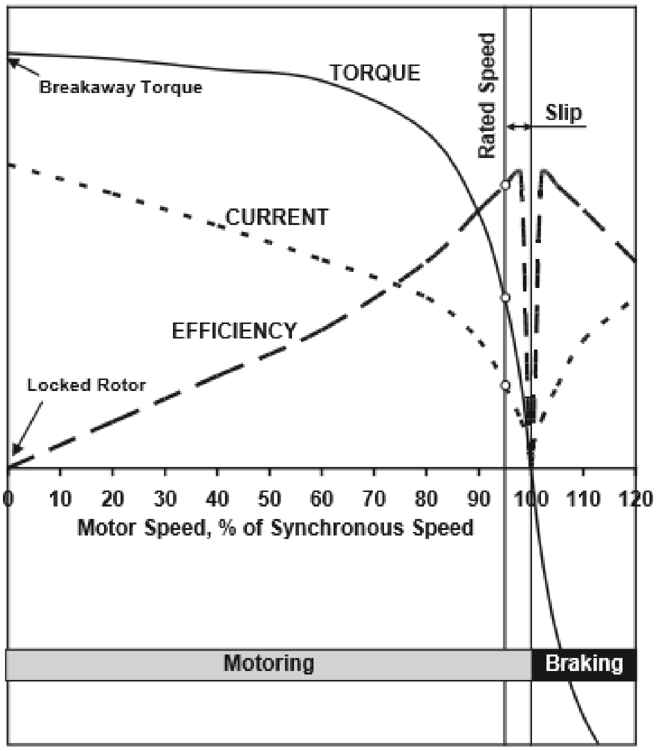

Figure 11: Performance Curves of NEMA D Motors [3, p. 239]

2.2.2 Selection of the Motor Size

To choose the appropriate motor size for a pumping operation, it is necessary to account for the strong fluctuations of the loads acting at the polished rod. As an example, during the upstroke the required amount of power is enormous, when the pump unit has to lift the whole rod string and fluid column, however during the downstroke no power is needed or even generated when the rod string gets lowered by its own weight. And although the counterbalance effect of the pumping jack and additional weights try to equalize these loads, there is still a certain amount of load fluctuations. In general, the motor size is chosen based on the average power requirements at the motor shaft, but since these fluctuations induce higher torques and as a consequence higher currents during some parts of the stroke cycle, a larger motor size must be chosen. The reason for this is that higher currents lead to a temperature rise above the allowable limit and as a result the motor will overheat or get damaged. The effect of torque fluctuations is described with the cyclic load factor CLF, a ratio between the root mean square and the average values of the motor current. Based on the linearity of the electric current versus torque characteristics **eq.4** [3, p. 350] can be used to predict the cyclic load factor.

$$\mathrm{CLF} = \frac{\sqrt{\frac{\int_0^T T_{net}^2 dt}{T}}}{\frac{\int_0^T T_{net}\, dt}{T}} \tag{4}$$

The minimum required motor size can be then determined by multiplying the average mechanical power required at the motor times the cyclic load factor, as seen in **eq.5**. [8, p. 497]

$$P_{req} = CLF * P_{mot} \quad (5)$$

Another rule of thumb to determine the required motor size is by simply doubling the average power acting at the motor shaft. In general, NEMA D motors are oversized by a larger margin, to ensure sufficient torque output at motor speeds close to the rated speed. [8, pp. 496-497]

2.3 Variable Speed Drive

A variable speed drive (VSD) is an electrical device that provides a continuous range speed control of the pumping process. It is placed between the power supply and the prime mover and controls the AC motor speed and torque by varying the input frequency and voltage.

2.3.1 Functionality of the VSD

Basically, the operation of a VSD controller can be subdivided into three steps, as shown in Figure 12: A converter section that converts AC voltage into DC voltage, a DC link section that provides a smooth waveform of the DC signal and an inverter section that creates AC voltage at a variable frequency. In addition the system is equipped with a regulator unit that provides information about the desired frequency and voltage output.

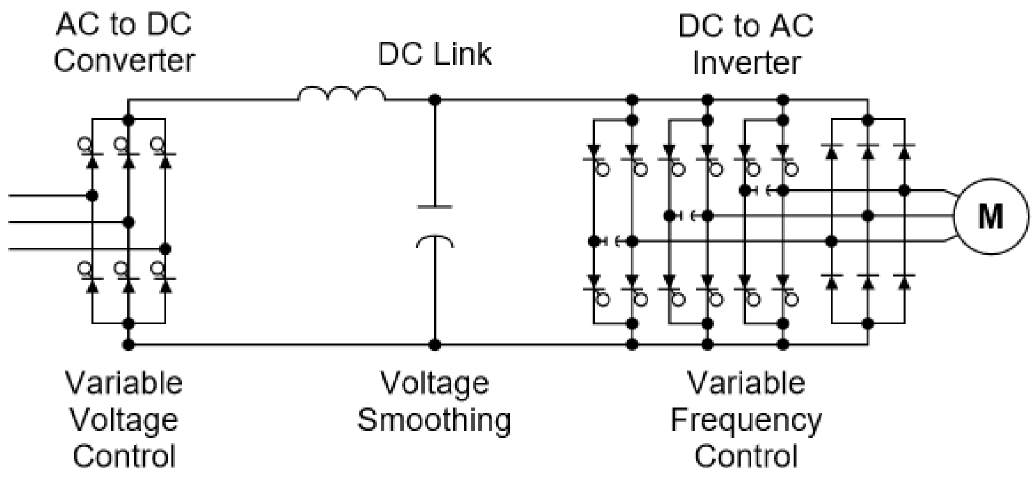

Figure 12: Major Components of a VSD Controller [17, p. 21]

The three phase input power from the AC line has a fixed frequency of 50 Hz and enters the converter section of the VSD controller. This section consists of a diode bridge rectifier and converts the AC input voltage into DC voltage. It is common that the suppression of the alternating waveform is incomplete resulting in unwanted residual periodic variation. These so-called ripples can be smoothened out in the DC link section by the usage of a capacitor. The core element of the VSD controller is the inverter section that generates the AC motor input by adjusting the voltage and frequency of the DC power. Most inverters operate according to the principle of pulsed-width modulation (PWM), where the AC waveform is produced by semiconductor switches like insulated gate bipolar transistors (IGBT). The major advantage of these inverters compared to previous ones is the close fit of the output current to a sinusoidal form that is required by induction motors. The inverter receives the filtered DC input from the DC link and generates a series of voltage pulses by switching on and of the transistors, where each signal has the same magnitude but a different width. The width of the pulses is regulated and controlled based on the desired output voltage and the number of pulses during one interval based on the desired frequency output. The amplitude of the voltage pulses is constant and equals the input voltage of the DC link. Higher frequencies and higher voltage are reached by producing fewer pulses during one cycle with a broader width. On the contrary, lower frequencies and lower voltage are reached by producing more pulses with a narrower width. Furthermore the alternating form of the output current can be achieved by reversing the polarity of the voltage pulses. Figure 13 gives an example of the output waveforms of a PWM inverter. [17, pp. 11-22] [18, pp. 1-5]

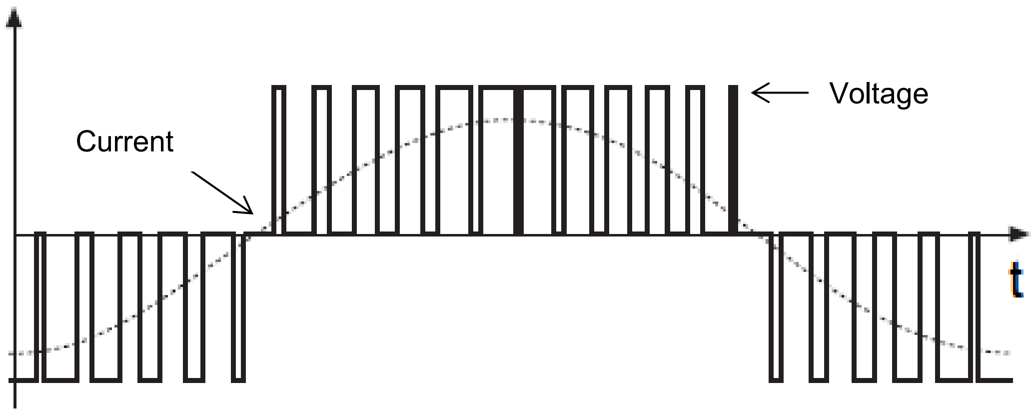

Figure 13: Waveforms of a Pulsed-Width Modulated Inverter [19]

It is of major importance that the VSD not only alters the frequency transmitted to the prime mover but also the input voltage. An increase in frequency without the increase in voltage will result in a higher motor speed but at the same time in a decreasing magnetic flux density in the motor’s air gap. This in turn leads to a decrease in motor torque since it is directly proportional to the magnetic flux density. Therefore, the ratio between volts and frequency must be kept constant allowing the electric motor to produce its output torque continuously at the rated value. The VSDs used at OMV Austria are provided by Schneider Electric with their key features listed in Table 2. [20] [21]

Table 2: VSDs used at OMV Austria

Designation	MX eco and MX pro
Power rating	55 kW, 90 kW
Rectifier	6-pulse diode rectifier
Inverter	6-pulse IGBT inverter
Line Voltage	3-phase 400 V, 50 Hz
Operating Temperature	-10…+50 °C

2.3.2 Usage in the Oil and Gas Industry

VSDs are already used for a wide range of applications in the oil and gas industry. Their growing popularity comes mainly from the high reliability of the system, the huge amount of energy savings and the reduction in maintenance. In addition VSDs allow for soft starts of motors and can reduce the air and noise pollution compared to other systems.

2.3.2.1 Transportation and Refining

The implementation of these speed controllers can be mainly seen in the transportation and refining processes, where large compressors and pumps are used to pump oil and gas through pipelines, refineries as well as petrochemical and gas treatment plants. For these applications it is often customary to use electric motors in conjunction with VSDs to allow a smooth start of the large motors and continuously adjust the speed to control the flow. On the one hand, an enormous amount of energy costs can be saved by eliminating the wasted energy in throttling valves to control the flow, as well as the resulting maintenance expenses of these valves. On the other hand, the motor can be protected against starting inrush currents. Compared to compressors driven by gas turbines, electric motor and VSD assemblies show much higher reliabilities and reduce the problems of air and noise pollution to almost zero. [22, pp. 1-2]

2.3.2.2 Oil and Gas Production

It gets also more and more common to use VSDs for the lifting of oil and gas, in order to assure economic feasibility of wellbores with complex formation or variable inflow conditions. Especially ESPs are often driven with VSDs to optimize the production rate and increase the operating life of the pump. This can be done by adjusting the frequency input to the pump to keep the dynamic fluid level in the wellbore constant at an optimum height. The fluid level should be as low as possible to reduce the hydrostatic pressure in the wellbore and allow more inflow from the reservoir, but high enough to avoid running dry conditions and gas liberation from the formation fluids, since ESPs are very sensitive to them. In this case the information for the VSD may come from a continuously monitoring fluid level measurement. The biggest advantage of a VSD-driven ESP is the possibility of ensuring a soft start of the pump, which is of major importance when producing heavy oils from a great depth. Even if it is intended to operate the ESP on a fixed supply frequency, it is common practice to start up the pump with a reduced frequency based on the great resistance forces of the viscous crude and the resulting rise in motor current. Without the usage of a VSD, this current may be up to 450% of the nameplate current, which leads to a drastic increase in motor temperature and consequently to motor damage or complete failure of the system. In general, the start frequency is about 1/5 of the operating frequency and is automatically increased with the aid of the VSD, by monitoring the motor current, until the well is cleaned up and the pre-set operating conditions have established. [23, pp. 2-3] [24, pp. 2-3]

For SRPs a similar approach can be chosen, where VSDs are used together with pump-off controllers to maximize the production rate while complying with mechanical and economic limitations. The pump-off controller (POC) is continuously fed from measurement sensors with operational data such as surface load, polished rod position and motor speed and signals the VSD to adjust the pumping speed. The basic adjustment principle is that the POC looks at the fillage of the downhole pump, seen on the dynamometer card, and signals the VSD to change the pumping speed when the pump fillage leaves the predetermined fillage range. Figure 14 illustrates the dynamometer card of a hypothetical well and shows the adjustment principle of the POC.

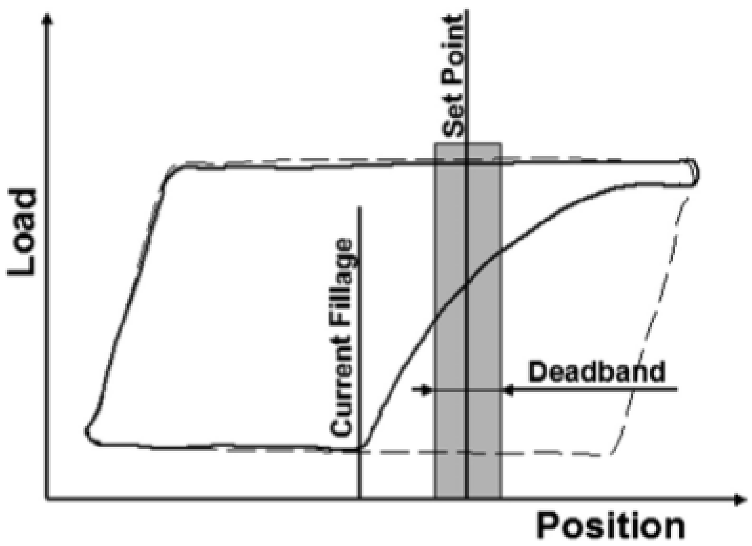

Figure 14: Adjustment Principle of the Pump-Off Controller [3, p. 417]

If the production rate exceeds the inflow performance of the reservoir and the fillage of the pump falls below the set range, the VSD reduces the input frequency and as a consequence the pumping speed. As a result the production rate decreases and the downhole pump fills again to a higher degree. On the contrary, if the pump fillage surpasses the predetermined limits, the VSD increases the input frequency to achieve higher pumping speeds and maximize the production. [3, pp. 415-418] [25, pp. 155-156]

A recent technology of a VSD application is the usage together with linear rod pumps (LRP) that is illustrated in Figure 15. The principle of a LRP is similar to a sucker rod pump, but instead of the surface pumping jack the system is driven with a rack-and-pinion unit and a reversible motor. A vertical tube is attached directly to the wellhead and houses a rack gear, connected to the polished rod and moved up and down by the pinion. The pinion is driven by the gearbox that is placed on the outside of the tube, next to the motor. Based on the simple design of the surface unit and the low resulting inertia, VSDs can be used to optimize the kinematic behavior of the polished rod by varying the motor speed. It is possible to install different velocities for both up- and downstroke to reduce the dynamic forces at the surface and as a consequence the energy consumption. The great advantage of LRPs compared to SRPs, in terms of speed variation during one stroke, is that the high inertial effects of the pumping jack can be neglected. This allows the selection of up- and downstroke velocities that are constant but different from each other, as well as abrupt velocity changes between the intervals. [26, pp. 1-3]

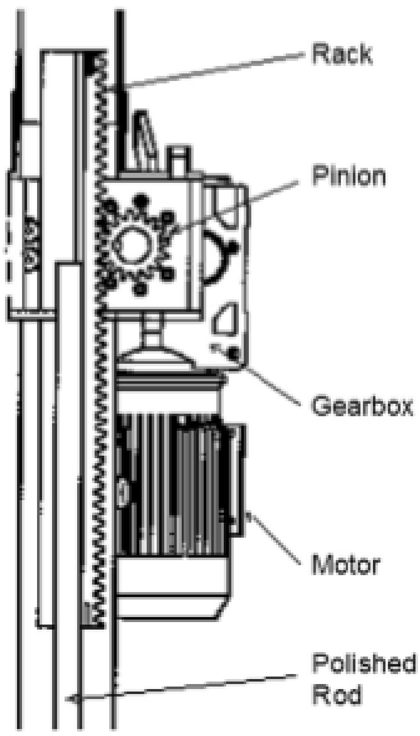

Figure 15: Schematic of a Linear Rod Pump [3, p. 225]

3 Latest Development: Frequency-Elastic Operations

3.1 Recent Technology Overview

There are only few operators or service companies found in the literature that have already tried to increase the energy efficiency or performance of a sucker rod pump, by using VSD controllers to alter the crankshaft velocity within one stroke. Two operators are found that came up with an optimization principle that is already in use and field-tested on a large scale, as well as one service company that offers a specially designed VSD controller for the same purpose.

3.2 Field Studies

The first field study was carried out by PDVSA, the national oil and gas company of Venezuela, that developed an improved sucker rod pump control by using VSD together with rod pump controllers. The project started in January 2004 and was performed on approximately 100 wells at the San Tome Orinoco Belt in Venezuela. The used VSD controller is equipped with an optimization algorithm that automatically changes the pumping speed over a couple of testing days in a predetermined velocity range and records the resulting production as well as pump fillage data. The recordings are then checked by the responsible engineers to define the optimum pump fillage, in terms of maximum production without exceeding the inflow performance of the reservoir or overstressing the pump plunger and the rod string. The VSD controller is then instructed to change the pumping speed in order to keep the desired pump fillage by analysing real-time dynamometer data. Furthermore the VSD is equipped with an exact model of the rod string and the downhole pump, which allows the controller to calculate the real-time plunger velocity by continuously recording the pumping speed within each stroke. Based on this data the surface speed is adjusted within the stroke to optimize the downhole behaviour of the pump. The VSD controller reacts to several downhole conditions: If the real-time dynamometer detects incomplete pump fillage, the plunger velocity and acceleration are reduced prior to fluid impact to guarantee better pump filling. As a consequence, the plunger speed is increased during other parts of the stroke, where it is low anyway, to remain or even increase the average pumping speed. The peak upstroke velocity is also decreased to ensure a lower pressure drop at the pump entrance, which reduces the problems of gas breakout in the downhole pump and allows the production at lower fluid levels. Moreover, the controller adjusts the pumping speed to balance the damping caused oscillations of the rod load, in order to minimize the risks of equipment failure. All of the tested wells have reacted differently and resulted in a unique surface velocity profile. The oil production of each well has increased in a range of 10 % to 160 %, based on the reduction in fluid level and increase in average pumping speed. The down-time of the wells has also decreased due to a better equipment protection. An example of this improved sucker rod pump control is shown in Figure 16 to Figure 19 , by comparing dynamometer cards as well as rod, plunger and crank velocity from a conventional operation to an optimized one. [27, pp. 1-3]

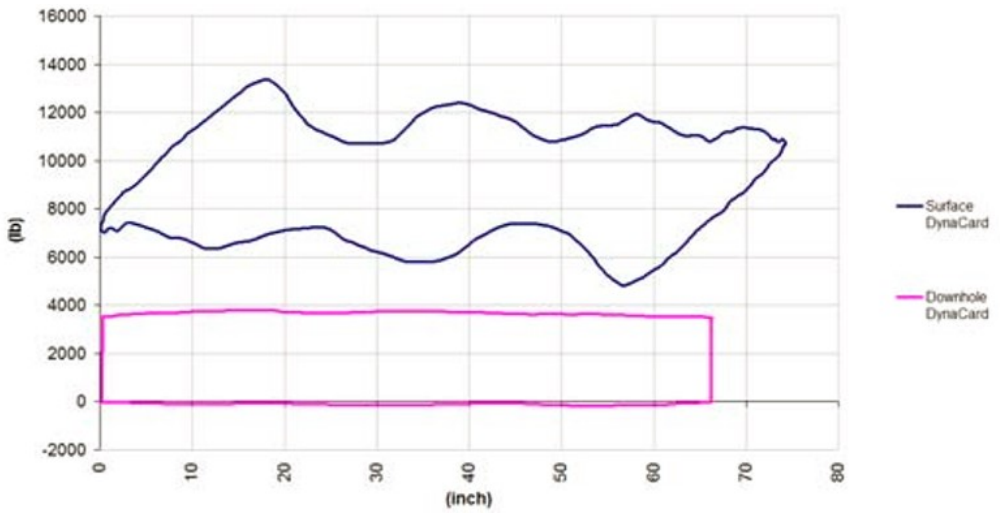

Figure 16: Dynamometer of the Conventional Operation [27, p. 6]

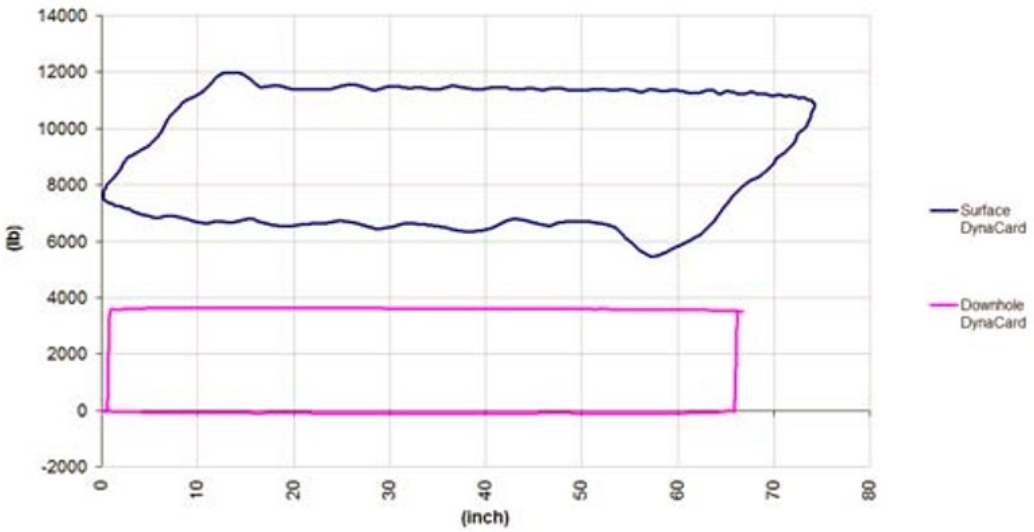

Figure 17: Dynamometer of the Optimized Operation [27, p. 6]

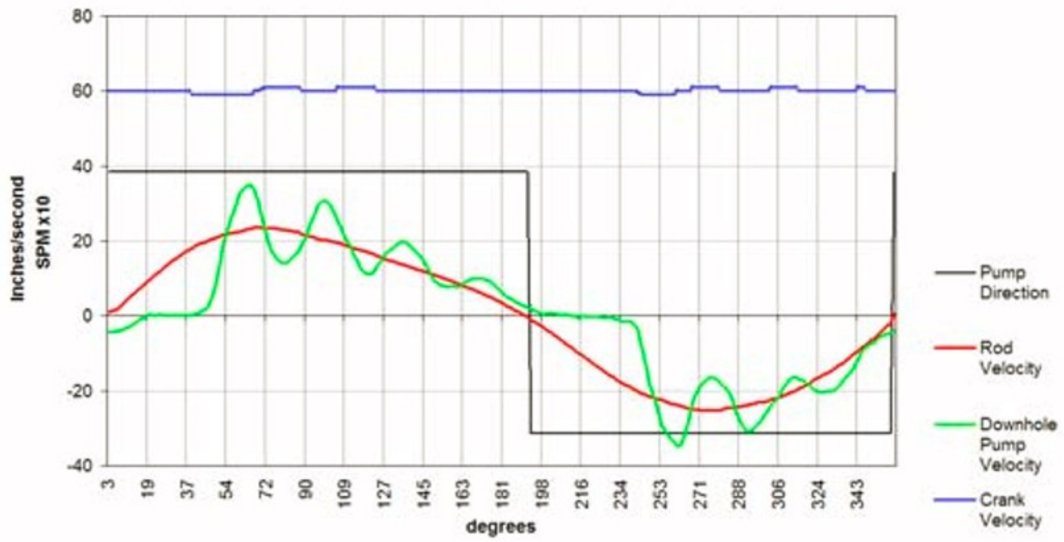

Figure 18: Rod, Plunger and Crank Velocity of the Conventional Operation [27, p. 6]

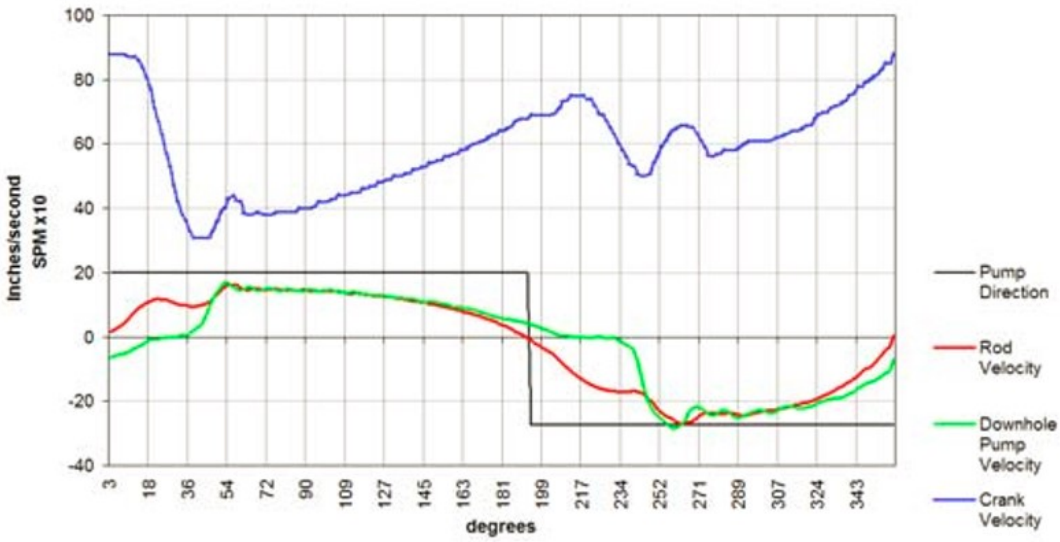

Figure 19: Rod, Plunger and Crank Velocity of the Optimized Operation [27, p. 6]

Another invention to optimize the performance of a sucker rod pump by changing the motor speed within one stroke was developed by the two Canadians Palka and Czyz in 2005. They came up with a specialized software that calculates the optimum motor speed variation in terms of maximizing production rate without increasing the energy consumption or stresses acting on the downhole equipment. The motor speed profile is described with Fourier series and the software calculates the appropriate coefficients for each well based on a kinematic model of the pump jack, a predictive analysis of the forces acting along the rod string and a dynamic model of the surface equipment. Their optimization algorithm was tested on 20 SRP wells in Alberta, Canada over a minimum period of six months. The wells are equipped with VSDs and a local control unit that collects data from the pump performance, such as polished rod load and position, motor torque and speed, as well as casing and tubing pressure. This information is then sent to a remote computer centre, where the software can simulate the optimum motor speed profile for each well. This data is sent back again to the local control unit that signals the VSD to adjust the motor input frequency to fulfil the provided motor speed profile. To illustrate the potential of this optimization principle, the operator provided the data of one of the tested wells. A 1940 m deep well with a 2 inch diameter pump is operated by a conventional pumping unit with a 3.05 m stroke and a 30 kW electric motor. Half of the rod string is made out of fibreglass, and the other half out of steel. The original pump performance is tested over a 24 hour period to obtain the required information, as mentioned above, that is fed into the optimization software. The optimal motor speed profile is now determined to maximize the production rate without increasing the Goodman factor and the energy consumption, and can be seen in Figure 20.

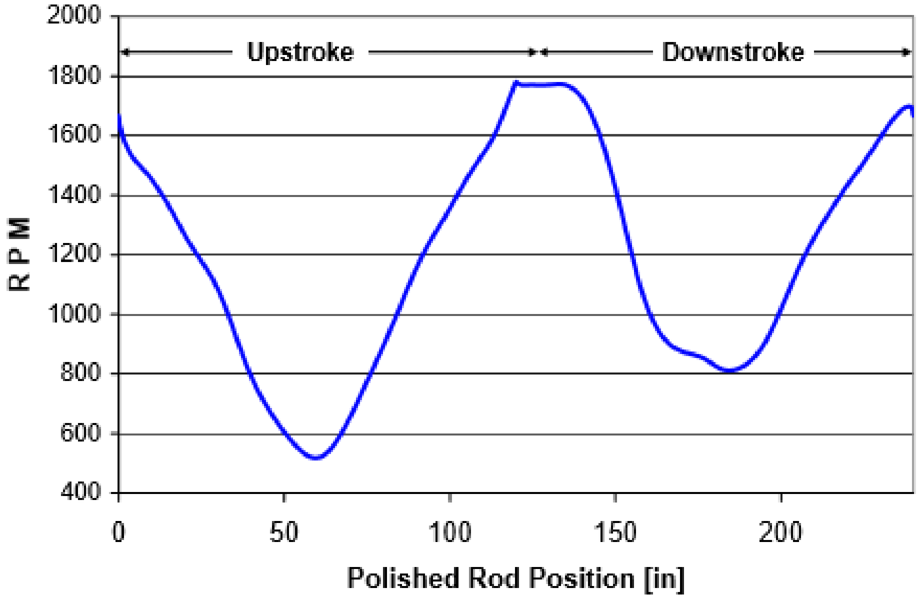

Figure 20: Optimized Motor Speed as a Function of Polished Rod Position [28, p. 7]

The resulting motor speed varies in a large range, especially during the upstroke, between 500 rpm and 1770 rpm. The average pumping speed is increased from 3.9 spm to 6.9 spm which leads to a production increase of 133 %, from 17.01 m³/day to 39.59 m³/day. In addition the Goodman factor remained the same, while the energy consumption decreased a little bit. An overview of the resulting parameters can be seen in Table 3. [28, pp. 1-10]

Table 3: Comparison of Constant and Optimal Motor Speed [28, p. 7]

Pumping Parameters	**Speed Profile**		**Change [%]**
	Constant	*Optimal*	
SPM	3.9	6.9	77
Plunger Stroke Length [m]	1.88	2.18	16
Pump Leakage [m³/day]	4.36	4.31	0
Pumped Volume [m³/day]	17.01	39.59	133
Max. Goodman Factor [%]	92	92	0
Energy Consumption [kWh/m³]	10.13	9.81	-4

3.3 Integrated VSD Controller

The service company Schlumberger has developed an integrated VSD controller, called UniStar, that adjusts automatically the pumping speed of a SRP in order to maximize oil production and enhance equipment protection, based on all available parameters. The controller operates sensor-free and contains real-time monitoring equipment that uses mathematical models to simulate the behaviour of the motor, the pumping unit, the rod string, the pump, the tubing, the casing, the fluid as well as the reservoir. In general the controller is ordered to maximize the pumping speed until certain limits are reached during parts of the stroke, where the velocity has to be reduced to ensure equipment protection. The rod loads are simulated based on the rod string data, fluid properties and eventually the computed rod friction factor for deviated wells. A range of maximum and minimum rod loads is predetermined to reduce the stresses in the rods, and if the rod loads exceed this range during the upstroke or drop below during the downstroke, the controller automatically reduces the speed. Furthermore, the unit simulates the crank position and the torque acting at the gearbox and adjusts the pumping speed in case of overloading and a possible damage to the gearbox. The possible belt slip that might occur during variable motor speed scenarios is considered as well and kept as small as possible to prevent excessive slippage or breakage. As far as the energy consumption is concerned, the controller monitors motor input power, motor output power as well as the power required at the polished rod and controls the speed to maximize production and efficiency of the system, without surpassing the thermal capacities of the motor and speed drive. Finally the controller is able to simulate the fillage of the downhole pump and adjusts the speed to prevent pump-off conditions and eliminate fluid pound. In addition, the speed is automatically reduced prior to fluid impact to protect the reservoir and prevent sanding. The accuracies of the simulated parameters are very high and therefore the parameters can be visualized for the operator to inspect the wells without the installation of sensors, such as load cells, position sensors or echometers. The most interesting real-time information for the operator is the production rate, the fluid level as well as surface and downhole dynamometer cards. The monitoring and controlling of the VSD unit can be done remotely, with an optional software installed on personal computers, tablets or mobile phones. The major features and benefits of the UniStar controller are summarized in the following list: [29, pp. 1-2]

- Optimized production under changing conditions
- Protects gearbox and downhole equipment
- Improves energy management and reduces the number of sensors
- System modelling and simulation
- Surface and pump dynacard generator
- Pump fill optimization
- Pump speed, rod load and gearbox control
- Motor current, torque and thermal control
- Power monitoring and control
- Data capture and communication

4 Methodology: Frequency-Elastic Operations

4.1 Description and Sample Well

In this chapter a model is set up, describing in detail all the necessary calculations that are used to determine the polished rod loads as well as the energy consumption during one complete stroke cycle of a SRP. The basic input parameters for this model are the pump jack geometry, the well completion and the pumping speed. Additionally, it is possible to insert a varying drive speed during one cycle or to adjust it automatically to minimize loads as well as energy demand. The four major parts of this model are: The kinematic analysis of the pumping unit, to describe the relation between crank rotation and polished rod movement, the one dimensional damped wave equation, to simulate the rod loads from the downhole pump up to the surface, the calculation of the gearbox net torque and surface efficiencies, to predict the energy consumption, and harmonic cosine functions, to describe the angular crank velocity during variable speed scenarios.

The data for the following calculations are taken from a sample well, called Well 1, which is located near Gaenserndorf and operated by OMV Austria GmbH. The total depth of the slightly inclined well is 1000 m with a KOP of 460 m and a total horizontal deviation of 197 m. The well is equipped with a C-320D-256-144 Lufkin pumping unit, a 7/8 in rod string and a 25-175 RHAC-21-4 insert pump, set in a 2 7/8 in tubing at a depth of 900 m. The pumping system is driven with a 40 HP (30 kW) NEMA D electric motor and under current production conditions (May, 2016), with a pumping speed of 4.19 spm and a pump efficiency of 65.77 %, the well produces 21.95 m³/day. An overview of the necessary input data can be seen in Table 4 and a drawing of the well schematic in Appendix A. [30]

Table 4: Input Data of Well 1 [30]

Well Name	Well 1
Pump Jack	C-320D-256-144
Peak Torque Rating	36,155 N m
PRL Rating	114 kN
Stroke Length	3.66 m
Pump Type	25-175 RHAC-21-4
Pump Depth	900 m
Pump Efficiency	65.77 %
Tubing Pressure	400 kPa
Casing Pressure	490 kPa
Water Cut	85.55 %
Oil Density	920 kg/m³
Fluid Level	827 m
Rod Diameter	7/8 in
Tubing Size	2 7/8 in

4.2 Kinematic Analysis of the Pumping Unit

As a first step it is necessary to have a closer look at the kinematic characteristics of the pumping unit, in order to predict the exact motion of the rod string and especially the polished rod. Therefore a mathematical method developed by Svinos, is applied to obtain displacement, velocity and acceleration of the polished rod as a function of crank angle or time. These parameters can be determined by solving a four-bar mechanical linkage problem that describes the conversion from rotary to oscillatory motion. Compared to previous work that was done by Gray, this model has two major advantages. The first one is that higher accuracies are achieved, since velocities and accelerations are calculated directly at each link of the system instead of numerical differentiation of the relation between rod position and crank angle. The other one is the fact that the kinematic analysis of Svinos also considers the effects of a variable crankshaft speed, which is a necessity for this study. The calculation is described in detail in the following chapters and performed in a Microsoft Excel sheet. [31]

4.2.1 Four-Bar Linkage Problem

In order to set up the four-bar linkage problem and represent it with a vector system, the exact geometry of the pump jack is needed. Figure 21 shows a simplification of the pumping unit to its essential geometric dimensions according to the API STD 11E [32] that have to be provided by the manufacturer. [31, pp. 1-2]

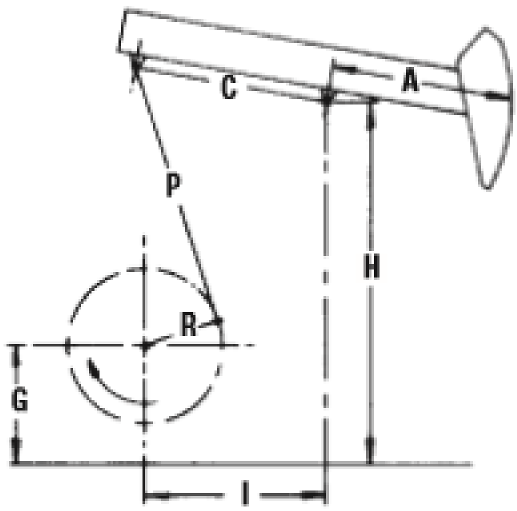

Figure 21: Geometry of the Pumping Unit [7, p. 6]

The dimensions for the C-320-256-144 pump jack of the sample well can be obtained from a Lufkin product catalogue and are summarized in Table 5. [7, p. 6] The dimension provided by Lufkin are given in inch and therefore converted to meters.

Table 5: Dimensions of a C-320-256-144 Pump Jack [7, p. 6]

A	180 in	4.57 m
C	120.08 in	3.05 m
I	120 in	3.05 m
P	144.5 in	3.67 m
H	260 in	6.60 m
G	111 in	2.82 m
R	47 in	1.19 m

In general crank arms have three or four wrist pin bearings, so the variable R can be adjusted by connecting the pitman to different bearings, depending on the desired polished rod stroke length.

The four-bar linkage problem consists of the vectors K, R, P and C, with K extending from the crankshaft to the saddle bearing. Additionally, an auxiliary vector L is needed between the wrist pin bearing and the saddle bearing as well as the angles of the crank, pitman and walking beam, θ_2, θ_3 and θ_4 measured from the reference line through vector K. A sketch of the stated four-bar linkage problem can be seen in Figure 22. [31, p. 2]

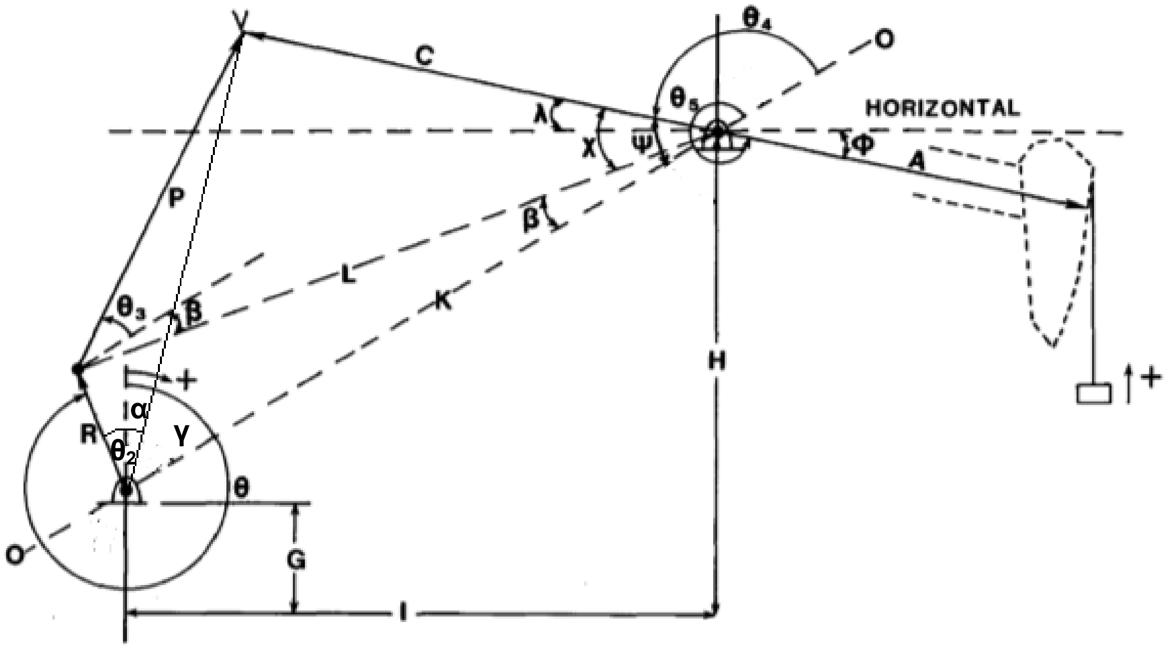

Figure 22: Sketch of the Four-bar Linkage Problem [31, p. 7]

The calculation of the missing dimensions and angles are shown in **eq.6** to **eq.16** [31, p. 2]. SI-units are used with the lengths given in meters and the angles in radian.

As a first step the length of vector K is described using the Pythagorean theorem.

$$K = \sqrt{(H - G)^2 + I^2} = 4.86\ \mathrm{m} \tag{6}$$

The angle of the crank arm measured from the position at the bottom of the stroke in counterclockwise direction is defined as

$$\theta_2 = 2\,\pi - \theta + \alpha \tag{7}$$

with α being the angle between the 12 o'clock and the bottom of the stroke position

$$\alpha = \sin^{-1}\left(\frac{I}{K}\right) - \gamma \tag{8}$$

and θ being the angle of the crank arm measured from the 12 o'clock position in direction of the crank movement. Moreover, the angle shift between the reference line and the position at the bottom of the stroke is given with

$$\gamma = \cos^{-1}\left(\frac{(R+P)^2+K^2-C^2}{2\,(R+P)\,K}\right) \tag{9}$$

The length of the auxiliary vector L is variable and depends on the position of the crank arm. As far as the calculation is concerned, the law of cosines needs to be applied.

$$L = \sqrt{K^2 + R^2 - 2\,K\,R\,\cos\theta_2} \tag{10}$$

The same law can be used to determine the angle between vector L and K as well as the angles of vector P and C, both measured from the reference line.

$$\beta = \cos^{-1}\left(\frac{L^2+K^2-R^2}{2\,K\,L}\right) * (j) \tag{11}$$

where

$$j = \begin{cases} 1 & \text{for } 0 < \theta_2 < \pi \\ -1 & \text{for } \pi < \theta_2 < 2\,\pi \end{cases}$$

$$\theta_3 = \cos^{-1}\left(\frac{P^2+L^2-C^2}{2\,P\,L}\right) - \beta \tag{12}$$

$$\theta_4 = \cos^{-1}\left(\frac{P^2-C^2-L^2}{2\,C\,L}\right) - \beta \tag{13}$$

Apart from θ_4, the position of the walking beam can also be described with

$$\psi = \cos^{-1}\left(\frac{C^2+L^2-P^2}{2\,C\,L}\right) + \beta \tag{14}$$

varying between the value at the bottom of the stroke

$$\psi_B = \cos^{-1}\left(\frac{C^2+K^2-(P+R)^2}{2\,C\,K}\right) \tag{15}$$

and the value at the top of the stroke

$$\psi_T = \cos^{-1}\left(\frac{C^2+K^2-(P-R)^2}{2\,C\,K}\right) \tag{16}$$

4.2.2 Angular Velocity and Acceleration

The next step of Svinos' kinematic analysis is the calculation of the angular velocities and accelerations at each link of the system. Regarding the crank arm, the angular velocity and acceleration can be calculated directly from the crank angle by taking the first or second derivative with respect to time. For the special case of a constant pumping speed, in this scenario 4.19 spm, **eq.17** and **eq.18** [3, p. 218] can be applied.

$$\dot{\theta}_2 = \frac{N\,\pi}{30} = 0.439\ \mathrm{rad/s} \tag{17}$$

$$\ddot{\theta}_2 = 0\ \mathrm{rad/s^2} \tag{18}$$

As far as pitman and walking beam are concerned, it is necessary to relate their angles θ_3 and θ_4 to the crank angle θ_2 first. This can be done by describing the motion of point V, the equalizer bearing, with vector addition from both sides. **Eq.19** [31, p. 2] shows the position in complex vector form.

$$\underline{P}_V = R\,e^{i\,\theta_2} + P\,e^{i\,\theta_3} = K + C\,e^{i\,\theta_4} \tag{19}$$

This expression can be differentiated with respect to time, to determine the velocity of point V. This can be seen in **eq.20** [31, p. 3] or by splitting this term in a real and an imaginary part in **eq.21** and **eq.22** [31, p. 3].

$$\dot{\underline{P}}_V = R\,\dot{\theta}_2 i\,e^{i\,\theta_2} + P\,\dot{\theta}_3 i\,e^{i\,\theta_3} = C\,\dot{\theta}_4 i\,e^{i\,\theta_4} \tag{20}$$

$$R\,\dot{\theta}_2 \sin\theta_2 + P\,\dot{\theta}_3 \sin\theta_3 = C\,\dot{\theta}_4 \sin\theta_4 \tag{21}$$

$$R\,\dot{\theta}_2 \cos\theta_2 + P\,\dot{\theta}_3 \cos\theta_3 = C\,\dot{\theta}_4 \cos\theta_4 \tag{22}$$

So with two equations and two unknowns, it is possible to solve for the angular velocity of the pitman and the walking beam, shown with **eq.23** and **eq.24** [31, p. 3].

$$\dot{\theta}_3 = \frac{R\,\dot{\theta}_2}{P}\,\frac{\sin(\theta_4-\theta_2)}{\sin(\theta_3-\theta_4)} \tag{23}$$

$$\dot{\theta}_4 = \frac{R\,\dot{\theta}_2}{C}\,\frac{\sin(\theta_3-\theta_2)}{\sin(\theta_3-\theta_4)} \tag{24}$$

Finally, **eq.25** and **eq.26** [31, p. 3] express the corresponding angular accelerations after a second differentiation with respect to time.

$$\ddot{\theta}_3 = \dot{\theta}_3\left[\frac{\ddot{\theta}_2}{\dot{\theta}_2} - \left(\dot{\theta}_3 - \dot{\theta}_4\right)\,\cot(\theta_3-\theta_4) + \left(\dot{\theta}_4 - \dot{\theta}_2\right)\,\cot(\theta_4-\theta_2)\right] \tag{25}$$

$$\ddot{\theta}_4 = \dot{\theta}_4 \left[\frac{\ddot{\theta}_2}{\dot{\theta}_2} - \left(\dot{\theta}_3 - \dot{\theta}_4\right) \cot(\theta_3 - \theta_4) + \left(\dot{\theta}_2 - \dot{\theta}_3\right) \cot(\theta_2 - \theta_3)\right] \quad (26)$$

4.2.3 Polished Rod Position

One of the most important results of the kinematic analysis is the position of the polished rod as a function of time, which is later on necessary to predict the motion of the entire rod string. The formula for this relation can be seen in **eq.27** [31, p. 3]

$$\mathrm{PR} = \mathrm{A}\,(\theta_4 - \frac{\pi}{2} - \alpha) \quad (27)$$

However in virtue of illustration purposes a dimensionless expression is more common. **Eq.28** [31, p. 3] shows the polished rod position in dimensionless form based on the beam angle ψ.

$$\mathrm{PR} = \frac{\psi_B - \psi}{\psi_B - \psi_T} \quad (28)$$

with:

PR	Polished rod position [-]
ψ_B | ψ_T	Angle of the walking beam at the bottom | top of the stroke [rad]
ψ	Angle of the walking beam [rad]

Figure 23 illustrates now the motion of the polished rod of the base scenario, with a constant pumping speed of 4.19 spm. Displayed is the movement of one stroke cycle, a time span of 14.32 s, with a position value of 0 representing the bottom of the stroke and a position value of 1 representing the top of the stroke.

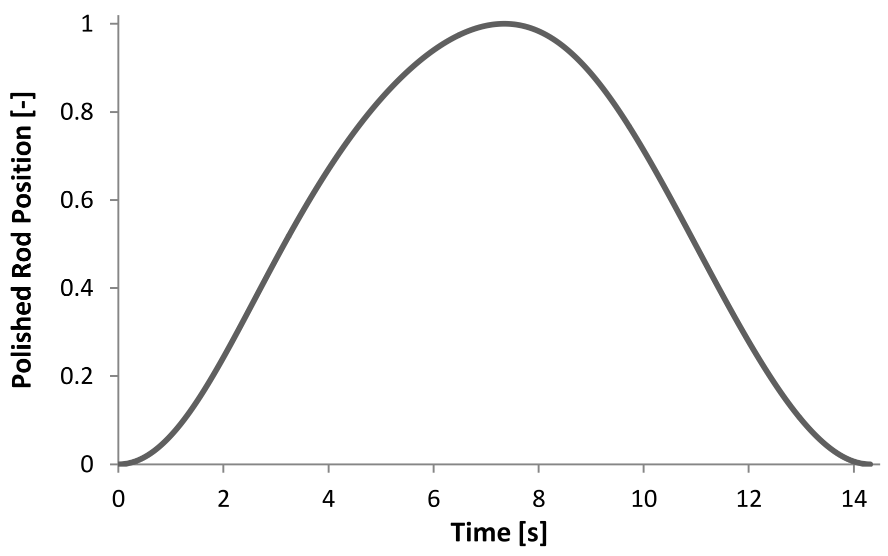

Figure 23: Polished Rod Motion of the Base Scenario as a Function of Time

4.2.4 Polished Rod Velocity and Acceleration

The next parameters that need to be calculated are the polished rod velocity and acceleration. This can be done, once again, by differentiation with respect to time. For the velocity a first order derivate of the polished rod position is taken, as seen in **eq.29** [31, p. 3] and in an analogous manner a derivative of second order is taken for the acceleration shown in **eq.30** [31, p. 3].

$$\mathrm{VR} = \mathrm{A}\ \dot{\theta}_4 \tag{29}$$

$$\mathrm{AR} = \mathrm{A}\ \ddot{\theta}_4 \tag{30}$$

with:

VR | AR	Polished rod velocity | acceleration [m/s | m/s²]
A	Distance between the horsehead and the walking beam [m]
$\dot{\theta}_4$| $\ddot{\theta}_4$	Angular velocity | acceleration of the walking beam [rad/s | rad/s²]

The time history of these two parameters as well as the dimensionless polished rod position over the cycle of one stroke of the base scenario is illustrated in Figure 24.

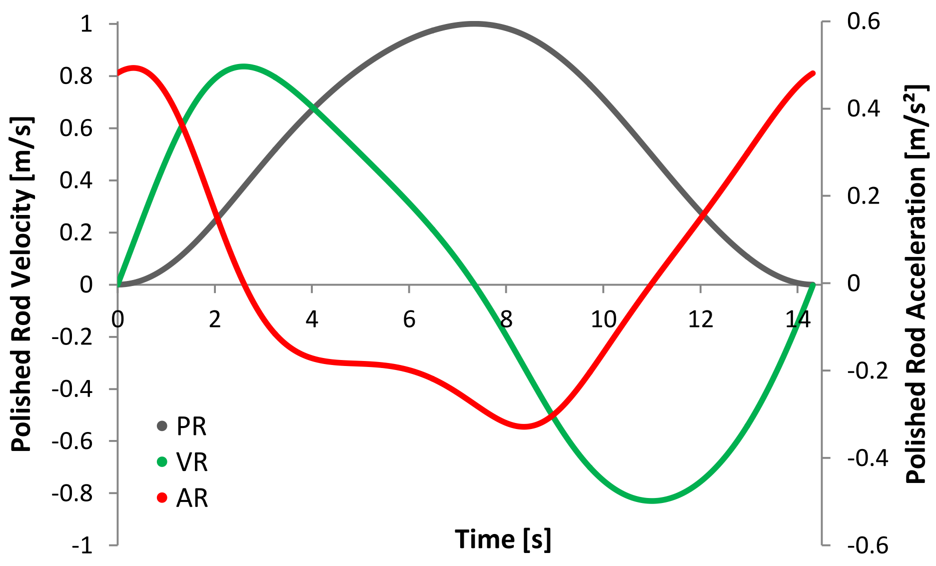

Figure 24: Polished Rod Velocity and Acceleration as a Function of Time

As far as the velocity is concerned, the peak of the upstroke is reached after 2.61 s with a value of 0.836 m/s and the peak of the downstroke after 11 s with a value of -0.830 m/s. The corresponding average velocities are 0.504 m/s and -0.532 m/s, resulting in an overall average velocity of 0.518 m/s. Considering the acceleration, the maximum is of special interest, which is reached early at the beginning of the upstroke after 0.33 s, with a value of 0.493 m/s².

4.3 Calculation of the Polished Rod Loads

The next step of the model is to predict the forces that are acting along the rod string, especially at the polished rod, during a complete pumping cycle. In general, a distinction is made between five different types of rod loads: [3, pp. 143-144]

- The **weight of the rod string**, a static force that is constant throughout a stroke cycle and positive in downward direction.
- The **buoyancy force**, describing the lifting effect of the rod string by the surrounding fluid. It depends on the density difference between rod material and produced liquid and acts in opposite direction of the rod weight. It is only considered during the downstroke.
- The **fluid load** which equals the hydrostatic net pressure of the produced liquid, put on the pump plunger at the bottom of the string. It is only considered during the upstroke, since the travelling valve of the plunger is open during the rest of the pumping cycle, and points in the same direction as the weight of the rod string.
- The **dynamic load** consisting of inertia effects of the moving string and fluid column, caused by acceleration changes of the rod string, and forces arising from the complex behavior of elastic stress waves travelling through the rod material. Although the amplitude of these forces changes permanently throughout a stroke cycle, dynamic loads are positive during the upstroke and negative during the downstroke.
- **Friction forces** that can be subdivided into fluid friction and mechanical friction. Fluid friction is the result of viscous forces induced by the contact between the rod string and the produced liquid. It is negative during the upstroke since the fluids are moving in the same direction as the rod string and positive during the downstroke because of their opposing movement. Mechanical friction is caused by the contact between rod and tubing string, stuffing box and polished rod as well as plunger and barrel of the downhole pump. It opposes the rod movement and is therefore positive during the upstroke and negative during the downstroke.

The whole calculation sequence is described in the following chapters and computed by using Mathworks MATLAB, with the time history of the polished rod position being imported from chapter 4.2. The used code can be seen in Appendix B.

4.3.1 One Dimensional Damped Wave Equation

In order to calculate or predict the loads occurring at the polished rod as accurately as possible, an exact simulation of the rod string behavior is necessary. Especially the elasticity of the rod material makes this a difficult task. On the one hand, all the forces and loads exerted at the downhole pump travel as stress waves throughout the string to the surface and on the other hand impulses produced by the pumping unit, such as the polished rod motion, are sent in the opposite direction. These elastic waves propagate at the speed of sound through the rod material and may interfere with each other or get reflected along the way, which makes the prediction of the polished rod loads such a complex undertaking. Gibbs was one of the first to set up a predictive method that includes the elastic characteristics of the rod string by describing the propagation of stress waves with a one dimensional damped wave equation. [33, p. 769]

The first step of Gibbs Model is to reduce the rod string to a representative element with a length of Δx and set up a force balance for this section. As seen in Figure 25, there are four forces acting on each rod section: Two tension forces, one from above $F_{x,}$ and one from below $F_{x+\Delta x}$, the weight of the rod element W, and a damping force F_d. [34, pp. 34-35]

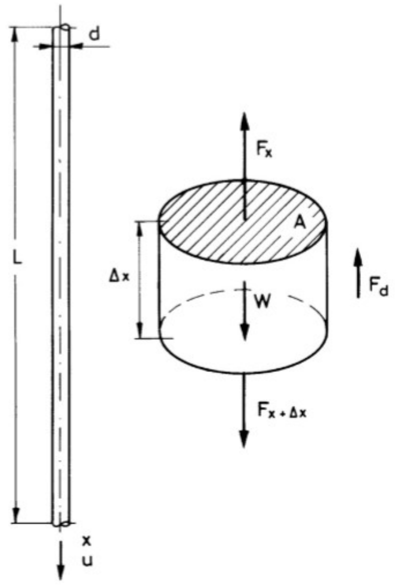

Figure 25: Forces acting on one Rod Element of the String [3, p. 275]

According to Newton's second law the sum of the forces on an object is equal to the mass of that object multiplied by the acceleration, given as the second derivative with respect to time of the displacement u. The force balance for this problem is stated in **eq.31** [3, p. 274].

$$F_{x+\Delta x} - F_x + W - F_d = m\frac{\partial^2 u}{\partial t^2} \tag{31}$$

This formula can be further adapted as seen in **eq.32** [3, p. 275] by removing the rod weight for now, as it is a constant force, and by expressing the pulling forces, as mechanical stresses on the cross-section area of the rod.

$$(S_{x+\Delta x} - S_x)A_{rod} - F_d = m\frac{\partial^2 u}{\partial t^2} \tag{32}$$

Furthermore, based on the elastic properties of the rod material, Hooke's law can be applied to express the mechanical stresses as a product of the Young's modulus E, a material specific parameter, and the rod strain, in this case the change of rod displacement over rod length. Consequently, the difference between the rod strains over the segment is given by the second derivative of displacement with respect to distance. In addition, the mass of the rod element can be expressed in a more general way, as the product of density and volume. The resulting form of the force balance is shown in **eq.33** [3, p. 276].

$$EA_{rod}\,\Delta x\,\frac{\partial^2 u}{\partial x^2} - F_d = A_{rod}\,\rho_{st}\,\Delta x\,\frac{\partial^2 u}{\partial t^2} \qquad (33)$$

The final thing that needs to be determined is the damping force. In general, this force equals the sum of fluid and mechanical friction and describes the energy that is lost from the polished rod to the downhole pump. Since the source and dependency of the two friction forces is very different and would result in a complex expression, the mechanical friction is neglected. This can be done because the sample well is assumed to be perfectly vertical and therefore rod and tubing string do not contact each other at any point of the system. Apart from that, the mechanical friction generated at the stuffing box or the downhole pump is comparatively small. As already mentioned, the fluid friction is a viscous force between the rod string and the produced liquid in the tubing, and is proportional to the shear velocity. For the solution of the damping force Gibbs stated the following formula, **eq.34** [3, p. 277].

$$F_d = c\,A_{rod}\,\rho_{st}\,\Delta x\,\frac{\partial u}{\partial t} \qquad (34)$$

with c being the damping coefficient, shown in **eq.35** [34, p. 36]

$$c = \frac{\pi\,v_s\,v}{2\,L_{rod}} \qquad (35)$$

v_s being the speed of sound through the rod material, depending on the Young's modulus and the steel density, as seen in **eq.36** [34, p. 35]

$$v_s = \sqrt{\frac{E}{\rho_{st}}} \qquad (36)$$

and v being the dimensionless damping factor that can be determined with empirical correlations. **Eq.37** [34, p. 41] shows the final form of the one dimensional damped wave equation according to Gibbs, after inserting the damping formula into the force balance and reducing Δx and ρ_{st}.

$$\frac{\partial^2 u}{\partial t^2} = v_s^2\,\frac{\partial^2 u}{\partial x^2} - c\,\frac{\partial u}{\partial t} \qquad (37)$$

The resulting formula is a partial differential equation of second order of the rod displacement as a function of position and time.

4.3.2 Numerical Solution of the Wave Equation

The wave equation can be now solved to determine rod displacement as well as load at each point along the string and at any time during the stroke. Since the final outcome of the analysis should be the polished rod loads throughout a pumping cycle, the solution of the wave equation requires the following boundary conditions. These are the polished rod displacement as a function of time that can be obtained from the exact kinematic analysis of the pumping unit as well as the downhole pump card that is assumed to be ideally shaped. In general, two different methods have established: the analytical solution that approximates the boundary conditions with Fourier functions and the numerical solution that is used in this work and described in detail. [35, pp. 121-122]

The most common numerical solution for partial differential equations is the finite difference method. This works by substituting the derivatives of the wave equation by Taylor series approximations. The three required Taylor expressions can be seen in **eq.38** – **eq.40** [33, p. 771].

$$\frac{\partial u}{\partial t} = \frac{u(x,t+\Delta t)-u(x,t)}{\Delta t} \tag{38}$$

$$\frac{\partial^2 u}{\partial x^2} = \frac{u(x+\Delta x,t)-2\,u(x,t)+u(x-\Delta x,t)}{\Delta x^2} \tag{39}$$

$$\frac{\partial^2 u}{\partial t^2} = \frac{u(x,t+\Delta t)-2\,u(x,t)+u(x,t-\Delta t)}{\Delta t^2} \tag{40}$$

In **eq.41** [33, p. 771] these terms are inserted into the general form of the one dimensional damped wave equation and rearranged to determine the rod displacement at the same axial distance but one time step further.

$$u(x,t+\Delta t) = \frac{c\,\Delta t\;u(x,t)+2\;u(x,t)-u(x,t-\Delta t)+\frac{v_s^2\,\Delta t^2}{\Delta x^2}[u(x+\Delta x,t)-2\;u(x,t)+u(x-\Delta x,t)]}{1+c\,\Delta t} \tag{41}$$

Before this equation can be solved, it is necessary to divide the rod string into m-elements of length Δx and the time span of one stroke into n-elements of length Δt. In order to get a high enough accuracy Δx is chosen to be 50 m. Consequently the 900 m long rod string is split into 18 elements of 50 m length. As far as the time step Δt is concerned, Courant-Friedrichs-Lewy condition needs to be considered. This mathematical condition calculates the maximum allowable time step for solving partial differential equations to still produce correct results. The used formula is a function of the length interval and the wave velocity and can be seen in **eq.42** [35, p. 123].

$$\Delta t \leq \frac{\Delta x}{v_s} \tag{42}$$

For this scenario the maximum allowable time step to produce accurate simulation results is 9.76 ms, but to be on the safe side half of this value is taken, leading to 2934 elements of 4.88 ms to describe one 14.32 s pumping cycle. Furthermore, the initial and the two boundary conditions need to be stated in advance. The rod displacement and velocities are zero at any point along the string, under static conditions at t=0, the displacement at the polished rod is equal to the dimensionless polished rod position times the stroke length S, as seen in **eq.43** [31, p. 3]

$$u(0,t) = PR(t) * S \tag{43}$$

and the displacement of the downhole pump can be related to the plunger load, determined in chapter 4.3.2.2, by using Hooke's law, as seen in **eq.44** [35, p. 122].

$$u(900, t) = u(850, t) - \frac{PL(t)\,\Delta x}{E\,A_{rod}} \quad (44)$$

With these equations it is now possible to solve for the rod displacement at any point in time and space. The corresponding load forces can be determined by applying Hooke's law once again and including the static weight of the rod section that is dropped in the one dimensional wave equation. The rod weight depends on the axial distance, as only the weight of the rod section below the point of interest acts as rod load. The final expression for the load forces is shown in **eq.45** [35, p. 122].

$$F(x, t) = \frac{u(x,t) - u(x+\Delta x,t)}{\Delta x}\; E\,A_{rod} + W(x) \quad (45)$$

with:

F	Rod load as a function of distance and time [N]
u	Rod displacement as a function of distance and time [m]
Δx	Length of a rod section [m]
E	Young's modulus [N/m²]
A_{rod}	Cross section of the rod string [m²]
W	Weight of the rod string as a function of distance [N]

As a next step, in order to obtain the polished rod loads as a function of time, the missing operational parameters such as the rod weight, the plunger load and the damping coefficient, need to be calculated.

4.3.2.1 Rod Weight

The rod weight is a static load, constant throughout a pump cycle, and arises from gravitational forces described by the mass of the rod string section times the gravitational acceleration, as shown in **eq.46** [3, p. 145].

$$W(x) = m^{*}\,(L_{rod} - x)\;g \quad (46)$$

with:

W	Weight of the rod string as a function of distance [N]
m*	Linear mass density of the rod string [kg/m]
L_{rod}	Length of the rod string [m]
x	Axial distance from the surface [m]
g	Gravitational constant 9.81 [m/s²]

The rod type used in this scenario is a Grade D steel rod string with a 7/8 inch diameter [30]. Consequently, the density of the material is 7850 kg/m², the Young's modulus is 2.06E+11 N/m² and the linear mass density of the rod string is 3.56 kg/m. [36, p. 23] The stated expression shows that the magnitude of the rod load depends on the axial distance of the reference point, since only the rod string section below this point exerts gravitational forces and must be taken into consideration. As a result, the rod weight varies between 0 N and 31,431 N, with the first value being reached at the bottom of the rod string, namely the pump plunger, and the second one at the top of the rod string, namely the polished rod.

4.3.2.2 Plunger Load

The forces acting at the pump plunger can be divided in two different terms, once the plunger load during the upstroke and once the plunger load during the downstroke. As far as the upstroke is concerned, the plunger load is equal to the weight of the fluid column in the tubing string and depends on the fluid properties, the wellhead pressure as well as the dynamic fluid level, as seen in **eq.47** [3, p. 147].

$$\mathrm{PL_{US}} = \left(\mathrm{p_{tb}} + \rho_{\mathrm{mix}}\, \mathrm{g}\, \mathrm{L_{dyn}}\right)\left(\mathrm{A_{pl}} - \mathrm{A_{rod}}\right) \tag{47}$$

with:

PL_{US}	Plunger load during the upstroke [N]
p_{tb}	Tubing pressure at the wellhead [Pa]
ρ_{mix}	Density of the fluid mixture [kg/m³]
g	Gravitational constant 9.81 [m/s²]
L_{dyn}	Dynamic fluid level from the surface [m]
A_{pl}	Cross section of the plunger [m²]
A_{rod}	Cross section of the rod string [m²]

As far as the downstroke is concerned, the traveling valve is open and therefore the weight of the fluid column does not act on the pump plunger anymore. The force that is now acting at the lowermost section of the rod string is the buoyancy, a lifting force of the submerged body by the liquids in the tubing annulus and the tubing pressure at the wellhead. Since this force acts in upward direction and opposes the weight of the rodstring, the plunger load reaches now a negative value. The buoyancy depends mainly on the rod string and fluid properties, and can be seen in **eq.48**.

$$\mathrm{PL_{DS}} = -(\mathrm{p_{tb}} + \rho_{\mathrm{mix}}\, \mathrm{g}\, \mathrm{L_{rod}})\mathrm{A_{rod}} \tag{48}$$

with:

PL_{DS}	Plunger load during the downstroke [N]
p_{tb}	Tubing pressure at the wellhead [Pa]
ρ_{mix}	Density of the fluid mixture [kg/m³]
g	Gravitational constant 9.81 [m/s²]
L_{rod}	Length of the rod string [m]
A_{rod}	Cross section of the rod string [m²]

Additionally it is necessary to model the closure and opening of the travelling valve to predict a steady transition from the plunger loads at the beginning and end of the upstroke. For simplicity reasons, a linear increase of the plunger load is assumed and the time for the build-up is chosen to match downhole and surface card as good as possible to the cards predicted by a RODSTAR simulation as seen in Appendix C. This can be done for the same well with different speeds between 2 and 10 spm, the typical operating range for this type of pumping unit, to find a trend for the build-up time as a function of the instantaneous pumping speed in the turning points. This trend is particularly important for frequency-elastic operations, since their cards cannot be predicted with RODSTAR. The transition time from the plunger loads is assumed to be equal for opening and closing of the valve and shown in Table 6 for corresponding sample speeds.

Table 6: Transition Time of the Plunger Load

Pumping Speed	Transition Time
2 spm	0.60 s
3 spm	0.52 s
4.19 spm	0.47 s
5 spm	0.42 s
6 spm	0.40 s
8 spm	0.37 s
10 spm	0.36 s

The function that relates the transition time to the instantaneous velocity in the turning points can be found by using a regression through the data points. In this case the best fit is described with a polynomial regression of third degree, as shown in **eq.49** and Figure 26.

$$t_t(N) = -0.0003521412\ N^3 + 0.0109010954\ N^2 - 0.1165303540\ N + 0.7832492879 \qquad (49)$$

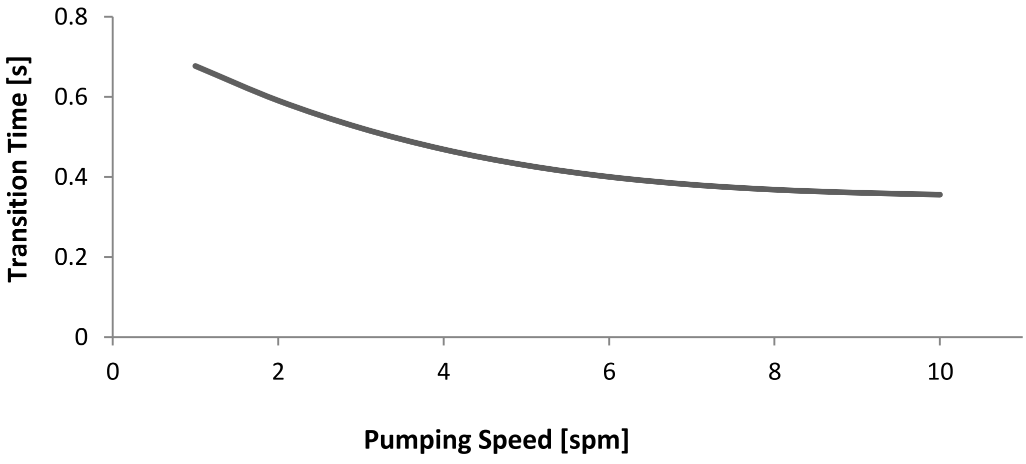

Figure 26: Transition Time as a Function of Pumping Speed

As a result, the time history of the plunger load of one stroke cycle can be determined. Figure 27 shows the plunger load of the base scenario with a pumping speed of 4.19 spm and a corresponding transition time of 0.47 s. The maximum plunger load is reached during the upstroke with a value of 9,798 N and the minimum during the downstroke with a value of -3,541 N.

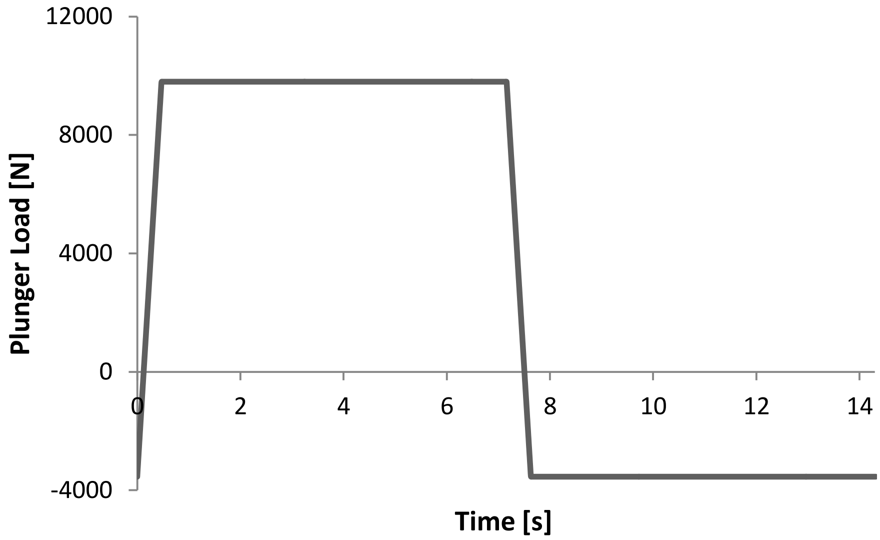

Figure 27: Plunger Load as a Function of Time

4.3.2.3 Damping Coefficient

The final parameter that is necessary to solve the one dimensional damped wave equation is the damping coefficient that describes the complex phenomenon of viscous friction. Since the damping force is equal to the energy that is lost across the rod string, Gibbs came up with a method that determines the damping coefficient with an energy balance for the polished rod and the downhole pump. Consequently, the damping coefficient is proportional to the difference in power transmitted to the polished rod and used at the downhole pump. Given that neither polished rod horsepower nor the surface dynamometer card is known, Gibbs proposes another method with an empirical correlation that gives the dimensionless damping factor as a function of the average polished rod velocity. The correlation is shown in Figure 28 with the polished rod velocity given in ft/s. [37, p. 3]

With an average polished rod velocity of 0.518 m/s or 1.699 ft/s, the base scenario results in a dimensionless damping factor of 0.14 and a damping coefficient of 1.25 1/s, considering a speed of sound through the rod material of 5,123 m/s. The damping coefficient can be double-checked and optionally updated by comparing once again the resulting surface pump card to the one from the RODSTAR simulation in Appendix C.

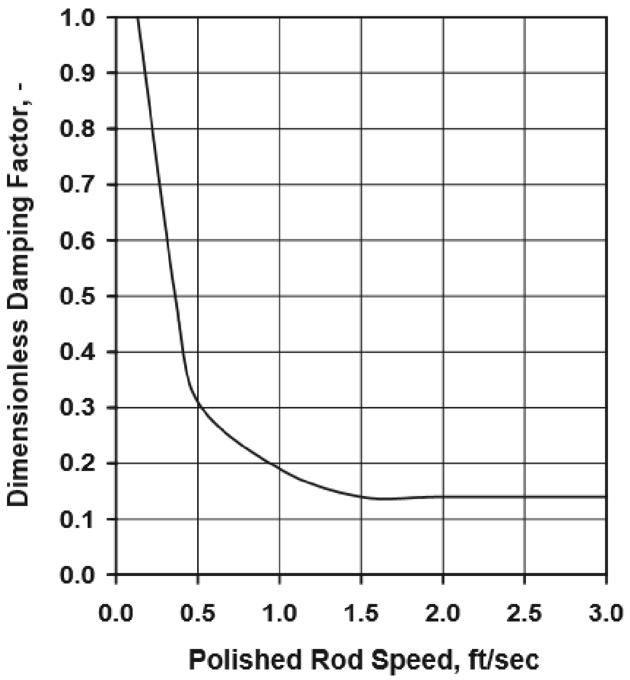

Figure 28: Damping Factor as a Function of Polished Rod Speed [3, p. 289]

4.3.3 Results of the Wave Equation

Finally, with all the necessary parameters determined, the one dimensional damped wave equation can be solved at the top of the rod string to predict the polished rod load for one stroke cycle as a function of time, as seen in Figure 29.

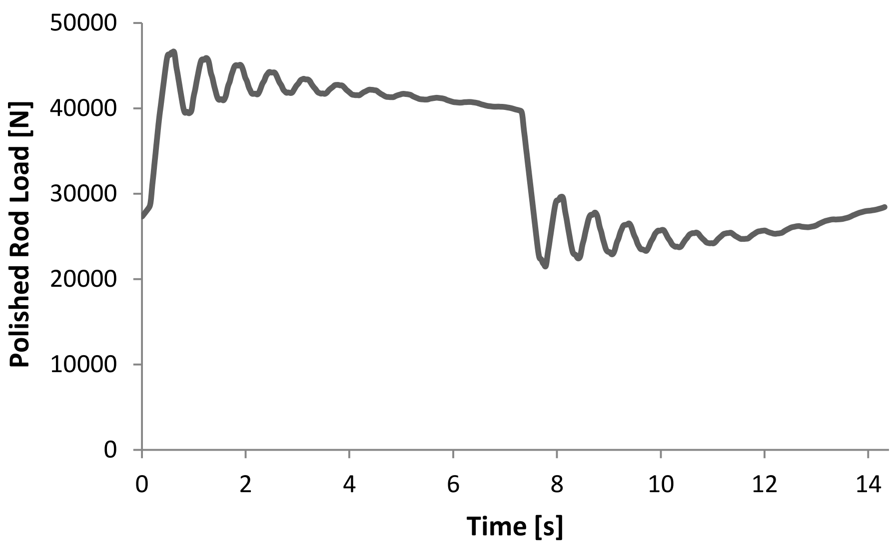

Figure 29: Polished Rod Load as a Function of Time

Furthermore, the loads at the polished rod can be split into the fluid load, rod weight and forces arising from dynamic effects, as shown in Figure 30. Fluid load and rod weight are fixed forces that are independent from the pumping operations. However, the dynamic effects include loads from viscous friction as well as inertia effects and depend on the polished rod movement such as position, velocity and acceleration. In addition, dynamic loads show the theoretical potential of load reduction by optimizing the pumping operation.

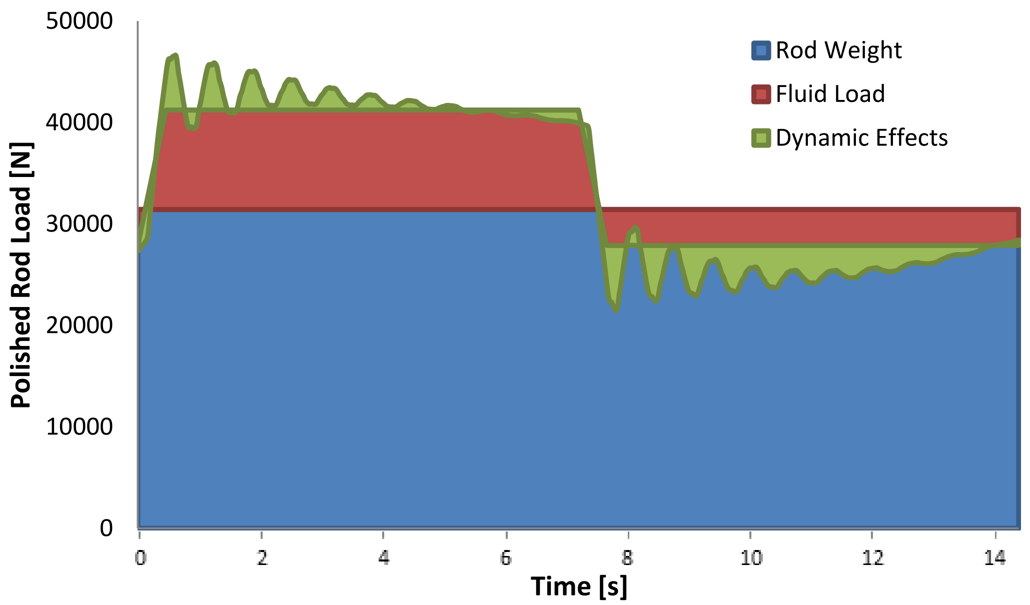

Figure 30: Split Polished Rod Loads

The base scenario shows a peak polished rod load of 46,645 N after 0.61 s. The associated portion of dynamic effects is 5,416 N, resulting in a maximum theoretical load reduction of 11.61 %. Other than the rod weight and the fluid load, the amount of dynamic effects depends on the pumping speed of the operation, with higher velocities resulting in a higher share. Table 7 gives a comparison of the percentage of dynamic effects for various pumping speeds.

Table 7: Percentage of Dynamic Effects for Various Pumping Speeds

Pumping Speed	Dynamic Effects	Dynamic Effects
3 spm	3,520 N	7.87 %
4.19 spm	5,416 N	11.61 %
5 spm	7,246 N	14.95 %
7 spm	11,979 N	22.51 %
10 spm	18,276 N	30.71 %

To conclude this chapter, the assumptions that are made for the calculation of the polished rod loads are summarized in the following list:

- The wellbore and rod string are assumed to be perfectly vertical
- No mechanical friction between rod and tubing string
- No mechanical friction between the polished rod and stuffing box
- No mechanical friction between the pump plunger and barrel
- The existence of rod protectors attached to the string is neglected
- The downhole pump card is assumed to be perfectly shaped
- The pump cards are matched with a RODSTAR simulation of the well
- The fluid friction is estimated with empirical correlations

4.4 Torque and Power Requirements

In order to calculate the required energy that is transmitted from the prime mover to the gearbox and converted into power for lifting rod string and fluids, it is necessary to determine the net torque at the crankshaft as well as the power efficiency of the surface equipment first. In the following chapters, the calculation procedure is explained in detail and the resulting MATLAB code is shown in Appendix D, with the polished rod loads, angular crankshaft and walking beam velocity as well as acceleration being imported from the MATLAB and Excel files from chapter 4.2 and 4.3. [38]

4.4.1 Calculation of Gearbox Torques

In general, there are three different types of torques that act at the gear reducer during the operation cycle of a SRP:

- The **rod torque**, defined as the force acting on a lever arm and indicates therefore the effect of polished rod loads at the gearbox.
- The **counterbalance torque**, resulting from the counterweights that are installed at the crank arms to balance the large difference in power requirements between the up- and downstroke, to improve efficiency and reduce motor and gearbox size.
- **Inertial torques**, describing the effects of energy storage and release in those parts of the pumping unit that turn at varying speeds. This includes articulating torque, arising from oscillating components such as the walking beam, horsehead, equalizer or pitman and rotary torque arising from the cranks and counterweights but only in the case of a variable crankshaft velocity.

As a result, the sum of these terms is the net torque acting on the gearbox, as described in **eq.50** [39, p. 104].

$$\mathrm{T_{net}} = \mathrm{T_{rod}} + \mathrm{T_{CB}} + \mathrm{T_{ia}} + \mathrm{T_{ir}} \tag{50}$$

4.4.1.1 Rod Torque

The rod torque is the product of the polished rod load and the torque factor which describes an imaginary lever arm. In addition, the rod force needs to be reduced by the structural unbalance, a specific pumping unit parameter provided by the manufacturer that indicates the required force to keep the walking beam in a horizontal position. For a C-320-256-144 pump jack this balance force is -1,780 N and points therefore in upward direction. The resulting formula for the rod torque can be seen in **eq.51** [40, p. 284].

$$\mathrm{T_{rod}} = \mathrm{TF\ (PRL - SU)} \tag{51}$$

with:

T_{rod}	Rod torque [N m]
TF	Torque factor [m]
PRL	Polished rod load [N]
SU	Structural unbalance [N]

According to Svinos, the torque factor can be calculated by setting up an energy balance from the crankshaft to the polished rod, as seen in **eq.52** [31, p. 4].

$$\mathrm{T_{rod}}\ \dot{\theta}_2 = \mathrm{PRL} * \mathrm{VR} \tag{52}$$

Assuming negligible inertia and friction effects, the energy at the gearbox, a product of rod torque and angular crank speed, is equal to the energy at the polished rod, a product of polished rod load and velocity. As a consequence the torque factor can be expressed with the relation in **eq.53** [31, p. 4].

$$\mathrm{TF} = \frac{\mathrm{VR}}{\dot{\theta}_2} \tag{53}$$

with:

TF	Torque factor [m]
VR	Polished rod velocity [m/s]
$\dot{\theta}_2$	Angular velocity of the crankshaft [rad/s]

Figure 31 shows the time history of the torque factor for one complete stroke cycle of the base scenario and Figure 32 the resulting rod torque as a function of time. The maximum torque is reached after 2.55 s with a value of 87,614 N m and the minimum torque after 10.69 s with a value of -50,995 N m.

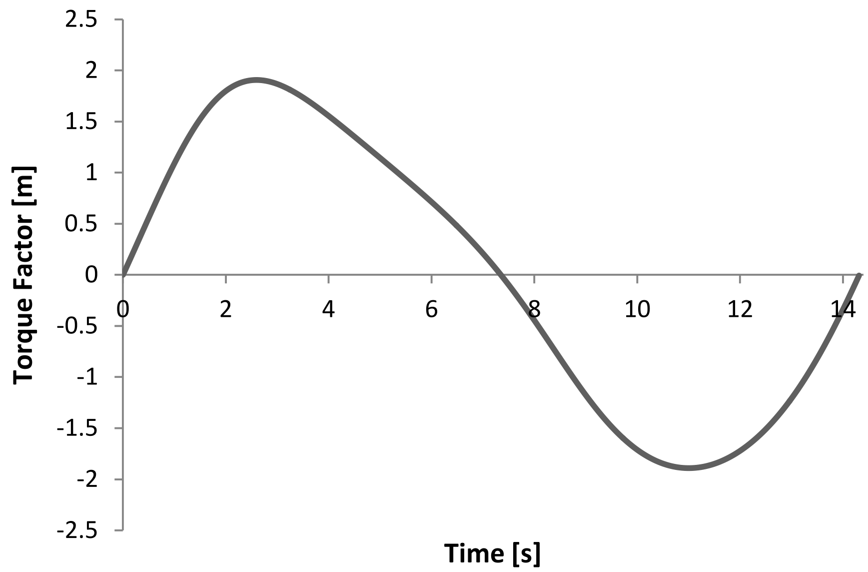

Figure 31: Torque Factor as a Function of Time

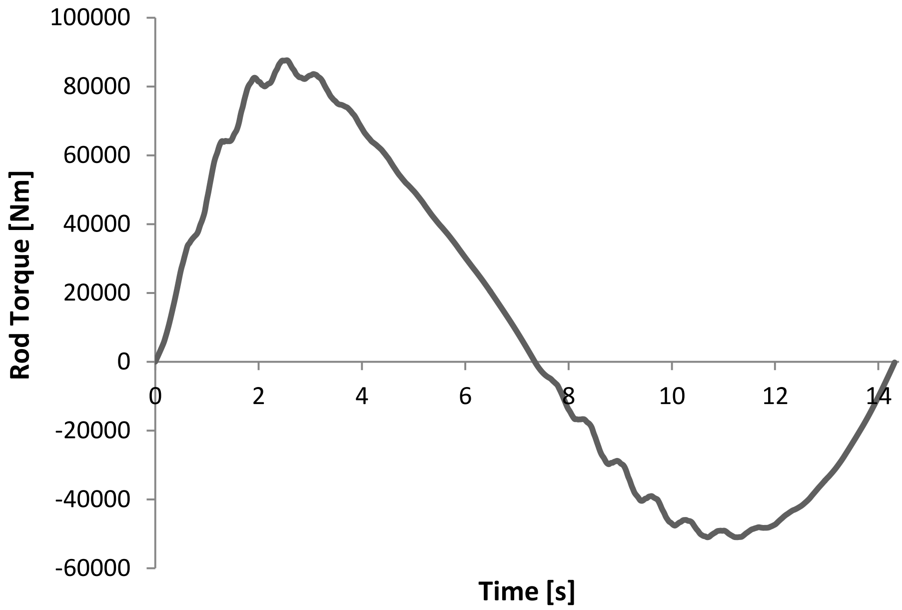

Figure 32: Rod Torque as a Function of Time

4.4.1.2 Counterbalance Torque

The counterbalance torque is the mechanical torque acting on the gearbox, produced by the crank arms, the attached counterweights and parts of the pitmans and is meant to oppose the rod torque. The torque can be calculated by taking the product of the weight and the distance between the center of gravity and the crankshaft. Since the distance changes constantly throughout a crank arm rotation, with a value of zero at the vertical positions and a maximum value at the horizontal positions, the counterbalance torque can be described with a sine function of the crank angle, as seen in **eq.54** [40, p. 285].

$$T_{CB} = -T_{CBmax} \sin\theta \tag{54}$$

with:

T_{CB} Counterbalance torque [N m]

T_{CBmax} Maximum counterbalance torque [N m]

θ Crank angle from the 12 o'clock position [rad]

The maximum torque is determined when the cranks are in horizontal position and is equal to the sum of the crank arm, counterweight and pitmans torque. For this sample well, the mechanical torque produced by the crank arms and pitmans is estimated to be 45,000 N m and 643 N m, respectively. However the one imposed by the counterweights is kept variable, to figure out the optimal counterbalance scenarios. The counterweights are positioned at a fixed distance of 3 m from the crankshaft and vary between 0 and 4000 kg. Consequently, the maximum counterbalance torque lies between 45,643 N m and 163,363 N m. Figure 33 shows the time history of the counterbalance torque over the course of one stroke cycle of the base scenario with the attached counterweights positioned at the minimum torque (MinTorque) setting. This means that the resulting peak net torque reaches the smallest possible value and requires therefore a maximum counterbalance torque of 71,541 N m.

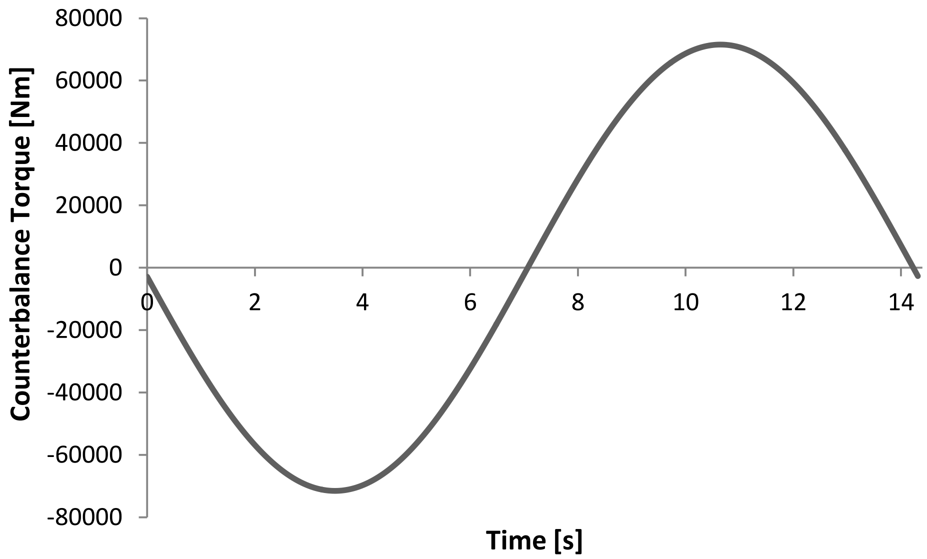

Figure 33: Counterbalance Torque as a Function of Time

A possible configuration for the required counterbalance effect is determined by using XBAL, as seen in Figure 34, with four 1225 kg heavy OARO counterweights positioned at 99.52 cm from the end of an 8495CA crank arm.

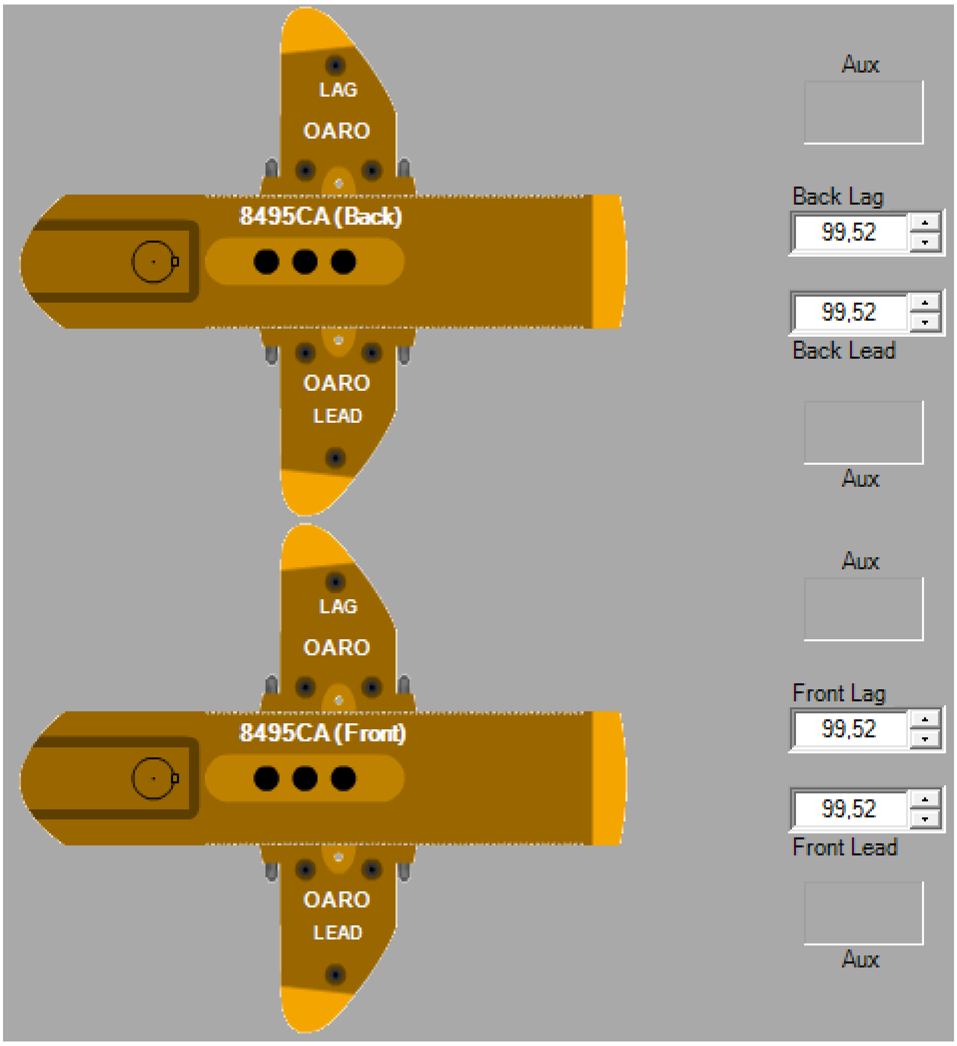

Figure 34: Possible MinTorque Counterweight Setting

4.4.1.3 Inertial Torques

Inertial torques represent the effects of acceleration and deceleration of pumping unit components on the gearbox torque and can be subdivided into two different categories. The first one is the articulating torque that needs to be considered for all pumping scenarios, even if the pump is driven with constant prime mover speed and arises from the varying speed of oscillating parts such as the walking beam, the horsehead, the equalizer and the pitmans. The articulating torque at the saddle bearing is defined as the product of the total mass moment of inertia and the acceleration of the walking beam, as seen in **eq.55** [40, p. 288].

$$T'_{ia} = I_{SB}\,\ddot{\theta}_4 \quad (55)$$

The mass moment of inertia is an extensive property and equals therefore the sum of the moments of the individual components. They can be calculated by taking the mass times the square of perpendicular distance to the rotation axis, and using data provided by the manufacturer as well as geometry estimations. [7, p. 6] [41] An overview of the articulating parts and their moments of inertia around the saddle bearing are listed in Table 8.

Table 8: List of Mass Moments of Inertia of the Oscillating Components

Component	Designation	Mass	Distance to SB	Moment of Inertia
Walking beam	W30x173	1981.2 kg	0.76 m	10730.7 kg m²
Equalizer	W24x55	82.0 kg	3.05 m	762.8 kg m²
Pitmans	W8x10	110.1 kg	3.05 m	512.1 kg m²
Horsehead	-	349.8 kg	5.00 m	8745.0 kg m²

As far as the sample well is concerned, the total mass moment of inertia of the oscillating components results in a value of 20,751 kg m².

In order to obtain now the articulating torque at the gearbox, the one calculated at the saddle bearing can be transformed into an equivalent polished rod force by dividing with the distance A and then multiplied with the torque factor, similar to the rod torque calculation. The final expression of the articulating torque acting on the gearbox can be seen in **eq.56** [40, p. 288].

$$T_{ia} = TF\,\frac{I_{SB}}{A}\,\ddot{\theta}_4 \quad (56)$$

with:

T_{ia} Articulating inertial torque [N m]

TF Torque factor [m]

I_{SB} Mass moment of inertia of the oscillating components [kg m²]

$\ddot{\theta}_4$ Angular acceleration of the walking beam [rad/s²]

A Distance between horsehead and the saddle bearing [m]

As a rule of thumb, the articulating torque is positive during the first half of the upstroke since the moving parts get accelerated, with the torque factor being positive at the same time. The result is a storage of kinetic energy and an increase in net torque at the gearbox. However, the second part of the upstroke shows a deceleration of the articulating components, with the torque factor still being positive, leading to a release in kinetic energy and a decrease in net torque. As far as the downstroke is concerned, a contrary behavior can be observed. Although, the effects of acceleration and deceleration are similar to the ones from the upstroke, the resulting articulating torque has reversed signs, based on the shift from a positive to a negative torque factor. [40, pp. 287-288]

The second category is the rotary inertial torque that is only produced in pumping operations with variable crankshaft velocity and is therefore neglected in most calculation procedures. However, for this work it is important to build a model that takes these effects into account since scenarios with both constant and varying crankshaft velocities are simulated and compared. The pumping unit components considered for the calculation are the counterweights, the crank arms as well as parts of the pitmans, with their mass moments of inertia listed in Table 9.

Table 9: List of Mass Moments of Inertia of the Rotary Components

Component	Mass	Distance to GB	Moment of Inertia
Crank arms	3988.8 kg	2.30 m	7033.6 kg m²
Counterweights	880.0 kg	3.00 m	7920.0 kg m²
Pitmans	110.1 kg	1.19 m	78.0 kg m²

The torque can be determined in a similar manner as the articulating torque with the total mass moment of inertia of the rotating parts times the acceleration of the crank arm, as seen in **eq.57** [40, p. 289].

$$T_{ir} = I_{rot}\,\ddot{\theta}_2 \tag{57}$$

with:

T_{ir} Rotary inertial torque [N m]

I_{rot} Mass moment of inertia of the rotating components [kg m²]

$\ddot{\theta}_2$ Angular acceleration of the crankshaft [rad/s²]

Concerning the base scenario, the effect of rotary inertia is zero because of a constant pumping speed and consequently a constant crank arm velocity. Generally speaking, acceleration of the crank arms leads to an increase in net torque and deceleration of the crank arms to a decrease in net torque. The cause lies again in the storage and release of kinetic energy. [40, pp. 288-289]

4.4.1.4 Net Torque

The sum of all individual torque components is the resulting net torque acting on the gearbox that needs to be overcome to drive the pumping unit. The time history of the net torque for the base scenario with the counterweights being positioned at the MinTorque setting can be seen in Figure 35. The peak net torque for this case is 28,928 N m which equals a capacity utilization of 80 %, compared to the maximum allowable gearbox torque of 36,155 N m indicated in red.

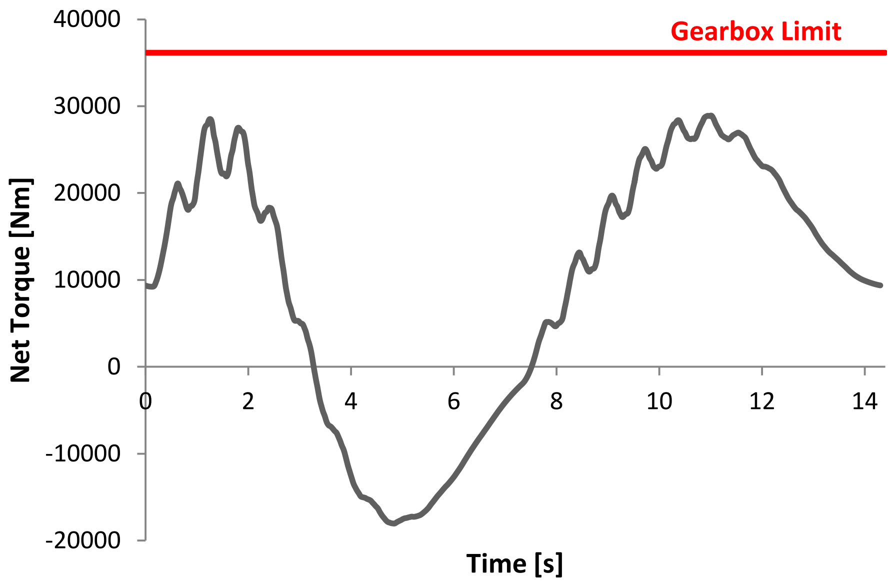

Figure 35: Net Torque as a Function of Time

4.4.2 Efficiency of the Surface Equipment

Power losses arise in several elements of a sucker rod pumping system. Most of these inefficiencies are mechanical, hydraulic and damping losses and occur downhole, in the subsurface pump, the rod string or the liquid column. Since these losses are already considered in the net torque by the dynamic analysis of the rod string, it is only necessary to additionally account for power losses in the surface equipment. In general there are two types of surface losses: mechanical losses in the drive train and losses in the prime mover. Losses in the drive train are caused by mechanical friction and occur in:

- The pumping unit's structural bearings
- The gearbox, between well-lubricated gear surfaces
- The V-belt and sheaves

They are summarized and represented by the surface mechanical efficiency η_{mech} that can be determined by using empirical correlations. One of these correlations is given by Gibson and Swaim [42], as seen in Figure 36, where the surface mechanical efficiency can be determined based on the ratio between the average net torque and the torque rating of the gearbox.

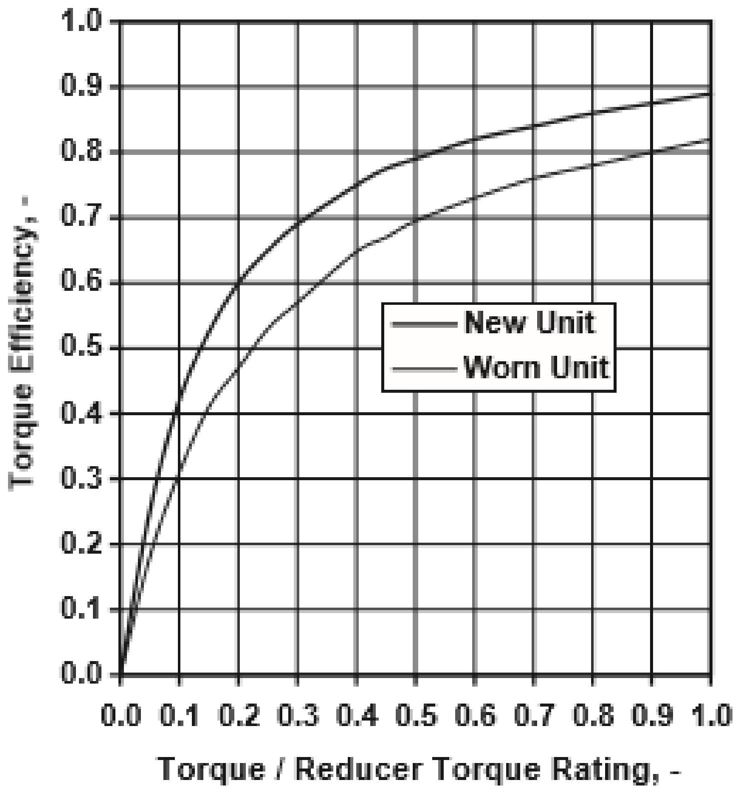

Figure 36: Estimation of the Surface Mechanical Efficiency [3, p. 342]

A differentiation is made between new and worn pumping units, with older ones resulting in a lower efficiency. With an average net torque of 9,218 N m and a gearbox rating of 36,155 N m, the minimum torque scenario shown in chapter 4.4.1.4 would result in a torque ratio of 0.25 and consequently in a surface mechanical efficiency of 0.54 for worn units as well as 0.65 for new units. Since other operators discovered that these correlations drastically underestimate the surface mechanical efficiency and that the mechanical losses are normally lower than 10 %, the efficiencies are raised and set to a fixed value of 0.9 for all scenarios. The second category of surface losses is motor losses and consists of:

- Electrical losses, subdivided in iron and copper losses
- Windage losses, consumed by the cooling air
- Mechanical friction losses in the structural bearings of the motor.

They are summarized by the motor efficiency η_{mot} and range for properly designed NEMA D motors between 78 % and 91 %. The motor efficiency of the scenarios performed in this work is assumed to be constant and set to the average value of the suggested range with 0.85. The total efficiency of the surface equipment η_{surf} equals the product of surface mechanical efficiency and motor efficiency and results in a value of 0.765. [3, pp. 366-367]

4.4.3 Calculation of Power and Energy Requirements

As a next step, power and energy requirements can be calculated that need to be transmitted from the prime mover to the gearbox to overcome the net torque. In rotational mechanics, the power is defined as the product of torque and angular velocity, in this case gearbox torque and angular crank arm velocity, and can be described with **eq.58**. Additionally, the required power is increased by the surface efficiency, to account for the power losses in the surface equipment.

$$P_e = \frac{T_{net}\,\dot{\theta}_2}{\eta_{surf}} \tag{58}$$

with:

P_e	Required electrical power [W]
T_{net}	Net Torque [N m]
$\dot{\theta}_2$	Angular velocity of the crankshaft [rad/s]
η_{surf}	Surface efficiency [-]

The power requirement for the base scenario with the counterweights being positioned at the MinTorque setting is shown in Figure 37 as a function of time, during one stroke cycle. The chosen counterweights do not only lead to the smallest peak net torque but also to the smallest peak power, with a value of 16.59 kW.

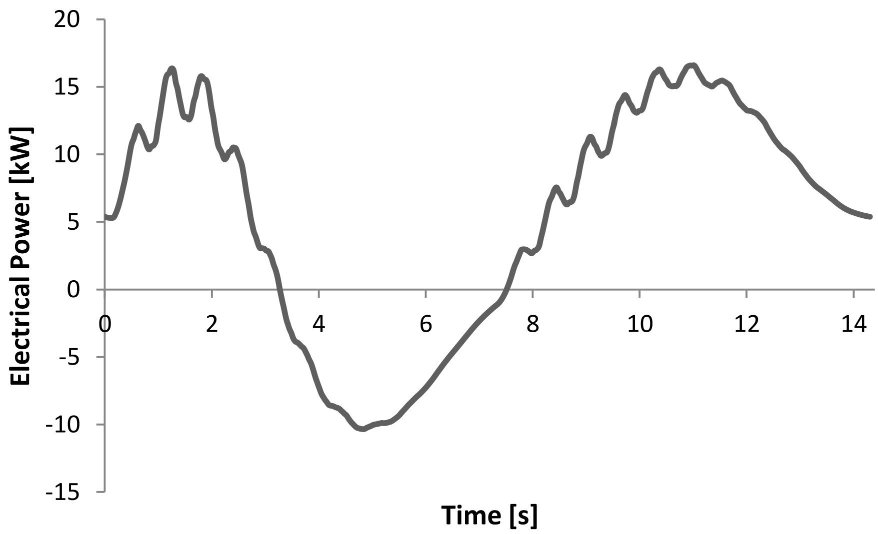

Figure 37: Power Requirement as a Function of Time

The energy consumption of the pumping unit can be determined by taking the integral of the power requirement with respect to the time variable t, expressed with **eq.59**.

$$E_{cons} = \int_0^t P_e \, dt \tag{59}$$

with:

E_{cons}	Energy consumption [J]
P_e	Electrical power input [W]
t	Time [s]

The time history for one stroke cycle is illustrated in Figure 38 for two different operation modes of the electric prime mover. The black line shows a two-quadrant motor with a detent power meter that has ratchets installed and can only rotate in one direction. However, the red line shows a four-quadrant motor with a non-detent power meter that can rotate in both directions and allows therefore the generation of electricity when the prime mover is driven by the pumping unit. Consequently, the four-quadrant motor results in a lower energy consumption. [16] [43, p. 50]

The scenario with the MinTorque counterweight setting of the base case results in an energy consumption of 7.14 kWh per hour with the usage of a two-quadrant motor and 5.28 kWh per hour with the usage of a four-quadrant motor. The daily consumption is 171.36 kWh and 126.72 kWh respectively, which results in electrical costs of 13.71 €/day and 10.14 €/day, taking an averaged electricity price in the European Union for industrial consumers of 0.08 €/kWh [44]. The application of a four-quadrant motor leads to a reduction in electrical expenses of 26 % or 3.57 €/day.

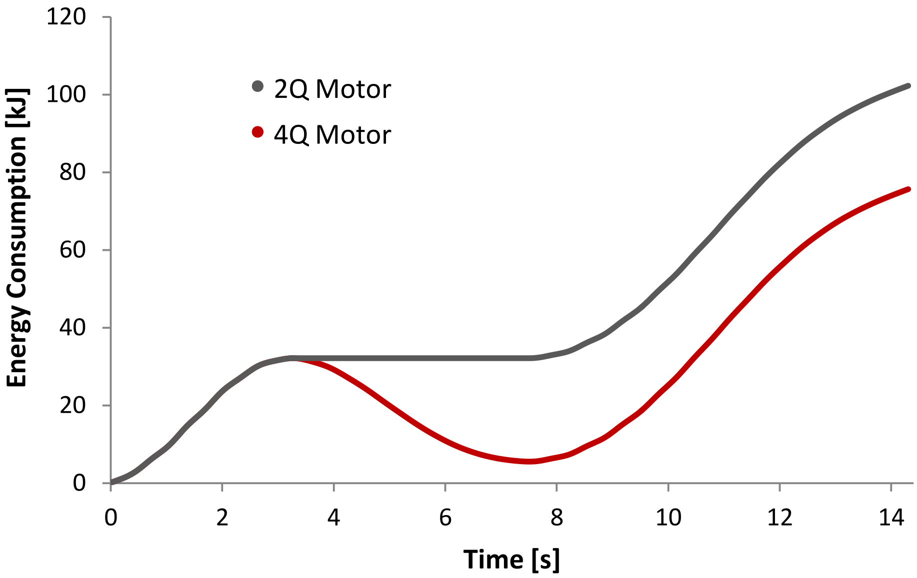

Figure 38: Energy Consumption as a Function of Time

4.5 Variable Crankshaft Velocity

One of the major aims of this work is to expand the typical calculation procedure of a sucker rod pumping system by including the effects of a variable crankshaft velocity. This chapter shows not only an approach to design a possible input function but also a way to optimize it in terms of minimizing polished rod load as well as energy consumption. In addition the influence on the operational parameters are demonstrated and compared with the ones from the constant pumping scenario. As far as the design phase is concerned, it is also necessary to account for the limitations imposed by the pump jack as well as the drive units such as the electric motor and the VSD that is necessary for these scenarios.

4.5.1 Limitations

The limitations consist of the minimum and maximum speed of the pumping unit as well as the allowable frequency range of the drive units and are described in the following chapters.

4.5.1.1 Critical Pumping Speed of the Pumping Unit

As a first step it is necessary to determine the maximum allowable instantaneous crankshaft velocity that should not be exceeded at any point of the stroke cycle. This can be done by applying the definition of the critical pumping speed. According to Byrd, this speed is reached when the carrier bar that is fixed to the horsehead by the wireline hanger, starts moving faster on the downstroke than the free fall velocity of the polished rod. In this case, a smooth transition between up- and downstroke cannot be guaranteed since the carrier bar might slam the polished rod clamp caused by an opposed movement. The result would be an overload of the pumping unit and gearbox. In general, the critical pumping speed is influenced by two parameters. The first one is the stroke length that indicates the velocity of the free rod fall in air and the second one is an empirical retarding factor that considers both buoyancy and friction forces. For production scenarios with conventional pumping units and ordinary oil characteristics the retarding factor is set to a value of 0.7. This means that friction and buoyancy forces in the wellbore reduce the free rod fall velocity by 30 percent. A commonly applied empirical formula for the critical pumping speed is provided by Lufkin in field units, as seen in **eq.60** [7, p. 70], which is based on the maximum acceleration of the pumping unit, the Mills acceleration factor and the standard acceleration of free fall. [45, pp. 1-2]

$$\mathrm{N_{crit}} = 0.7\sqrt{\frac{2{,}189\,\delta\,\mathrm{g}}{\mathrm{S}}} \tag{60}$$

with:

N_{crit}	Critical pumping speed [spm]
S	Stroke length [in]
δ	Mills acceleration factor 0.85 [-]
g	Gravitational constant 32.17 [ft/s²]

As a consequence, the sample well with a stroke length of 3.66 m is limited to a pumping speed of 14.29 spm or an angular crankshaft velocity of 1.496 rad/s. In addition, the critical pumping speed as a function of stroke length is illustrated in Figure 39.

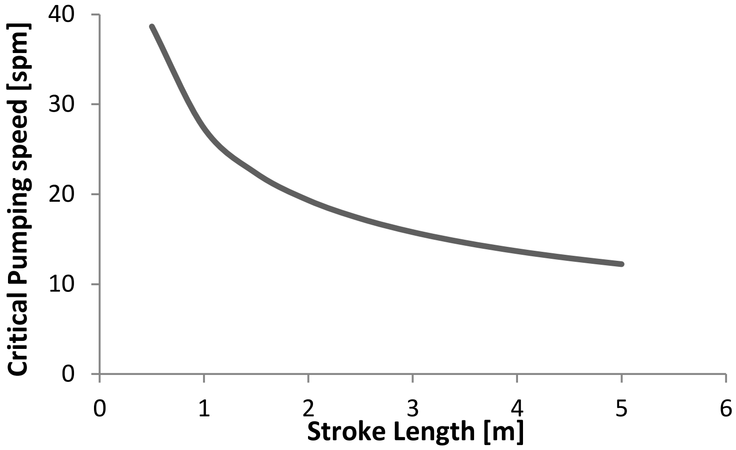

Figure 39: Critical Pumping Speed as a Function of Stroke Length

4.5.1.2 Minimum Pumping Speed of the Pumping Unit

Concerning the minimum pumping speed, the manufacturer recommends a limit of 5 spm for standard operations to ensure sufficient and continuous lubrication of the gear reducer. However, it is possible to run the pumping unit at much lower pumping speeds, till about 2 to 2.5 spm, by the installation of additional high speed gear wipers. This is necessary especially for pumping operations with longer stroke lengths since they often require pumping speeds below the initial limit. Regarding variable speed drive scenarios, the instantaneous crankshaft velocity may even go below 2 spm. The reason is that the lubrication of the gearbox depends on the interval of the stroke and not the instantaneous pumping speed. As a result the only limit of the pumping unit for variable speed drive scenarios is that the average pumping speed of a stroke cycle must be higher than 2 spm or the average crankshaft velocity higher than 0.209 rad/s. [7, p. 47]

4.5.1.3 Allowable Frequency Range of the Drive Units

In general, manufactures of the drive units, especially the electric motors, provide data about the optimum operating range to ensure the output of the full torque requirements. In the case of electric motors designed for a 50 Hz AC power supply, the standard devices used for sucker rod pumping, full torque is provided between 3 and 50 Hz. In addition, it is mandatory to consider excessive heating of the drive units during pumping operation that may result in an enormous efficiency decrease as well as equipment damage or failure. To avoid these problems, standard motors are usually equipped with integral cooling fans that force air into the system to remove the generated heat. However at low speeds, the cooling does not work sufficient enough due to an inadequate air flow and therefore manufactures often suggest a minimum speed of 30 percent of the rated motor speed. Consequently, the allowable frequency for standard 50 Hz electric motors range between 15 and 50 Hz. If it is still necessary to reach lower pumping speeds it is possible to install an external ventilation or to use inverter duty motors that are specially designed for the usage with VSDs and can operate till 20 percent of the rated speed based on a different cooling method and a higher class insulation. As far as the VSD is concerned, there are no further limitations in the allowable frequency range, since it can handle the full frequency spectrum from 0 to 50 Hz. The only requirement for VSDs, in terms of sufficient cooling, is an ambient air temperature below 50 °C. Even the frequency changes (Hz/s) of the resulting speed functions are feasible with conventional VSDs. [46, p. 50]

To determine the corresponding crankshaft velocity range, the instantaneous pumping speed can be calculated with **eq.61** [3, pp. 231, 235, 236].

$$\mathrm{N} = \frac{1}{\mathrm{Z}} \frac{\mathrm{d_{PM}}}{\mathrm{d_{GB}}} \frac{120\,\mathrm{f}}{(1+\mathrm{s})\,\mathrm{p}} \tag{61}$$

- Z is the speed reduction ratio of the gearbox, a fixed value of 30.12 that is provided by the pumping unit manufacturer [7, p. 46]
- d_{PM} is the diameter of the prime mover sheave that has a size of 240 mm under the current operation scenario [30]
- d_{GB} is the diameter of the gearbox sheave that has a size of 1130 mm under the current operation scenario [30]
- s is the slip factor of the motor that is set to 5 %, an averaged value of standard electric motors used for sucker rod pumping [3, p. 238]
- p the number of poles in the stator, a fixed value of 6 for standard electric motors used for sucker rod pumping [3, p. 235]

As a result the allowable range of the instantaneous pumping speed is 2.01 spm to 6.72 spm and the one of the corresponding angular crankshaft velocity is 0.210 rad/s to 0.704 rad/s. This interval can be shifted up- or downwards by adjusting the size of the prime mover and gearbox sheave.

4.5.2 Input Function for Variable Speed Scenarios

In order to optimize the polished rod load or the energy consumption of a SRP by means of variable speed scenarios, it is necessary to design the velocity function of the crankshaft first. The requirements for the input function can be determined by having a close look at the development of the polished rod load and the energy consumption of the base scenario. Since both parameters reach their peak values at the beginning of the upstroke, the crankshaft velocity and acceleration should be there as low as possible. In addition the function should have a smooth path without abrupt velocity changes, to minimize the effects of inertial torque. Therefore, this work uses two harmonic cosine functions, one for the upstroke and one for the downstroke, with the same speeds in the turning points. Apart from the limitations described in the previous chapter, the design requires two additional input parameters, the time ratio of the upstroke to the total stroke as well as one instantaneous velocity along the cycle. Most of the time, the maximum velocity during the downstroke is chosen. Care has to be taken, that the distances travelled during up- and downstroke are identical and equal the adjusted stroke length. Furthermore the average crankshaft velocity over the course of one stroke cycle should stay the same compared to the constant pumping scenario, since the strokes per minute are designed based on the inflow performance of the reservoir. A change of the average pumping speed might either lead to pump off conditions or to a decrease in oil production.

4.5.2.1 Calculation of the Input Function

The general form of the cosine function with respect to time that is valid for both stroke intervals can be seen in **eq.62** [47, p. 662]. The function is given in radians per second.

$$f(t) = a * \cos\left(\frac{2\,\pi}{T}\,(t - t_0)\right) + d \tag{62}$$

- a is the amplitude of the function defined as the difference between the turning point velocity and the average interval velocity [rad/s]
- T is the length of the stroke interval and indicates the period of the cosine function [s]
- t_0 is the starting point of the stroke interval and indicates the phase shift of the cosine function. For the upstroke this value is zero. [s]
- d is the vertical shift of the cosine function and equals the average interval velocity [rad/s]

These four parameters need to be defined for both the upstroke and the downstroke to obtain the input function for the instantaneous crankshaft velocity. The first step of the calculation procedure involves the determination of the two interval lengths based on the upstroke ratio R_{US} and the average pumping speed. The formulas for the upstroke time span T_{US} and the downstroke time span T_{DS} can be seen in **eq.63** and **eq.64**, respectively.

$$T_{US} = R_{US}\,\frac{60}{N_{avg}} \tag{63}$$

$$T_{DS} = (1 - R_{US})\,\frac{60}{N_{avg}} \tag{64}$$

Sequentially, the average pumping speed or more importantly the average angular crankshaft velocity of the two intervals, the up- and downstroke, can be determined with **eq.65**, which equals the vertical shift of the cosine function.

$$d_i = \frac{\frac{60}{2*T_i}\,\pi}{30} \tag{65}$$

Additionally, the time span of the upstroke provides information about the phase shift of the downstroke cosine function. The turning point velocity that is equal for the up- and downstroke can either be an input parameter or calculated based on the chosen maximum as well as average velocity of the same interval. Commonly, this is done for the downstroke since its maximum velocity gets closer to the defined limitations for optimized scenarios. The resulting formula for the turning point velocity can be seen in **eq.66**.

$$\dot{\theta}_{TP} = d_{DS} - (\dot{\theta}_{maxDS} - d_{DS}) \quad (66)$$

Finally, the amplitude of both cosine functions is determined by subtracting the corresponding average interval velocity from the turning point velocity, as seen in **eq.67**.

$$a_i = \dot{\theta}_{TP} - d_i \quad (67)$$

4.5.2.2 Optimization Procedure

The optimization of the polished rod loads and/or the energy consumption is performed by varying the ratio of the upstroke and the maximum downstroke velocity within the scope of the defined limits. This can be done by using trial and error methods as well as solvers working with generalized reduced gradient (GRG) algorithms [48]. In this particular case, a starting value for the maximum downstroke velocity is chosen that lies beneath the critical pumping speed. As a next step the GRG solver is used to find the upstroke ratio that leads to the lowest peak polished rod load or energy consumption. The resulting velocity function is then checked in regards to the limitations, especially the velocity range imposed by the electric motor. The load and energy data are listed and the whole process is repeated by changing the maximum downstroke velocity in steps of +/- 0.001 rad/s. A general rule can be observed: The larger the maximum downstoke velocity, the lower the peak polished rod load and energy consumption, based on the low resulting turning point velocity. In addition, the higher the ratio of the upstroke the lower the peak polished rod load, based on the reduced upstroke velocities:

$$\dot{\theta}_{TP} \downarrow \Longrightarrow \mathrm{PRL} \downarrow$$

$$\dot{\theta}_{TP} \downarrow \Longrightarrow E_{cons} \downarrow$$

$$R_{US} \uparrow \Longrightarrow \mathrm{PRL} \downarrow$$

The optimization procedure is performed together with the polished rod load and energy calculation in an Excel sheet and the resulting time history of the polished rod position, angular velocity and acceleration of the crankshaft and walking beam is imported to the MATLAB files of chapter 4.3 and 4.4.

4.5.2.3 Optimization of the Base Scenario

As an example, the optimized case of the base scenario with a pumping speed of 4.19 spm can be shown, combining both energy and load reduction. The maximum downstroke velocity is set to a value of 0.812 rad/s with an upstroke ratio of 0.585 and a turning point velocity of 0.245 rad/s, respectively. The resulting function of the instantaneous angular crankshaft velocity can be seen in Figure 40 and a comparison of the function to the constant one in Figure 41 on a radial diagram in clockwise direction.

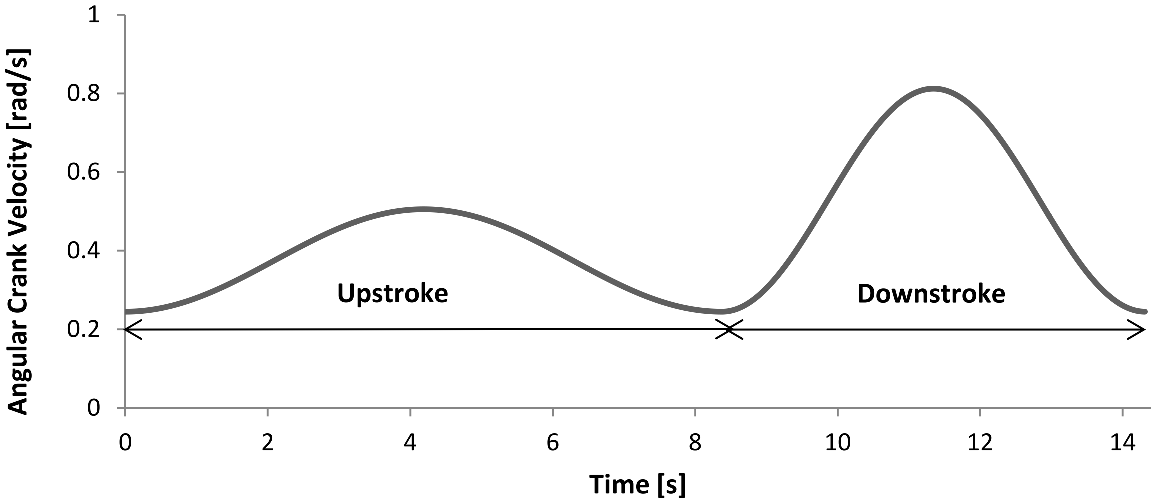

Figure 40: Angular Crankshaft Velocity of the Optimized Case as a Function of Time

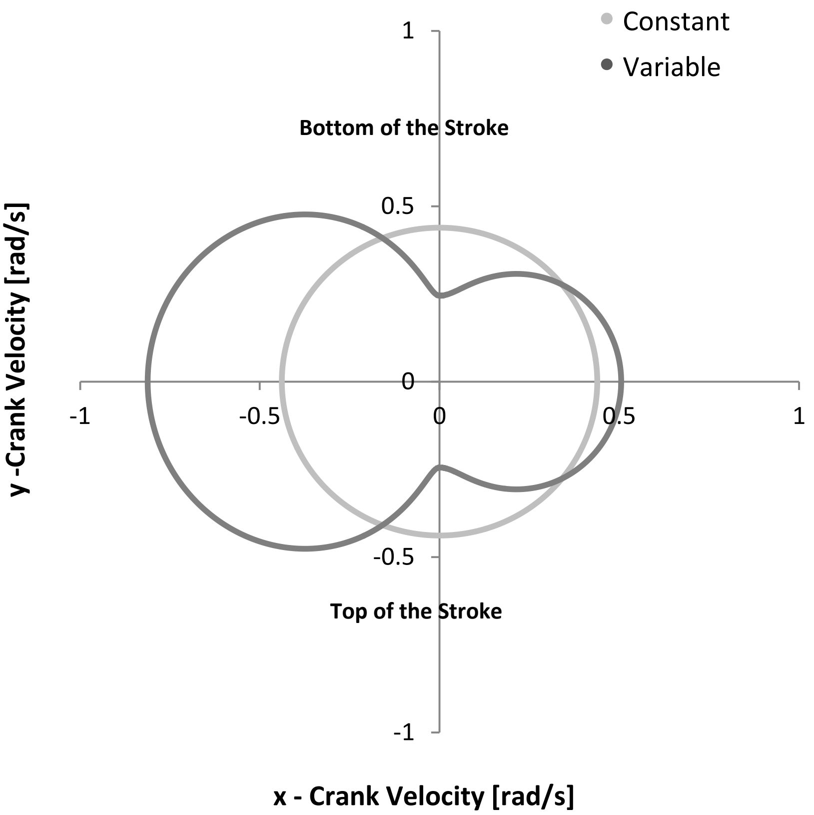

Figure 41: Comparison of the Angular Crankshaft Velocity on a Radial Diagram

In addition, a comparison of the polished rod motion between the constant and optimized case is given in Figure 42.

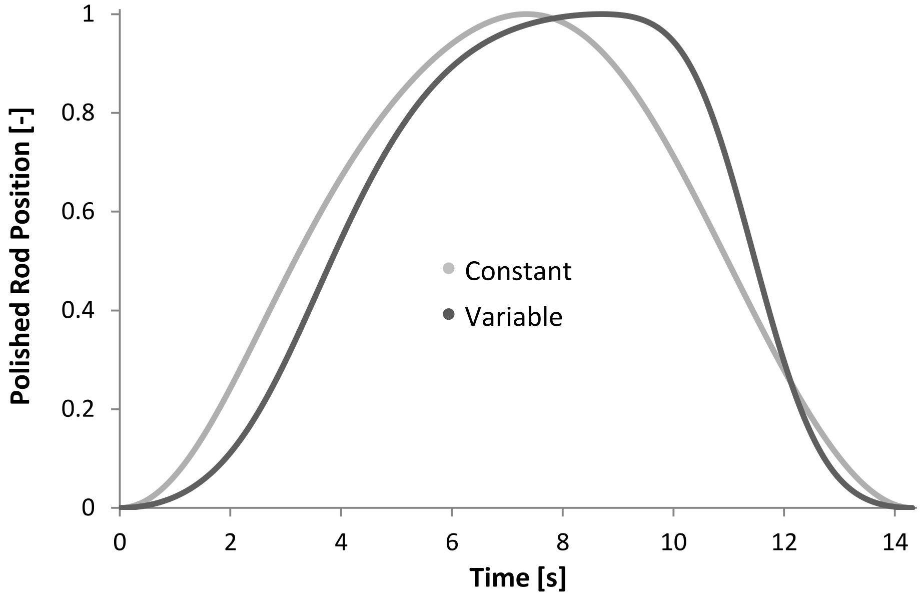

Figure 42: Comparison of the Polished Rod Motion as a Function of Time

The impact on the polished rod load can be seen in Figure 43. The peak polished rod load is shifted from 46,645 N to 44,902 N, which equals a reduction of the total loads of 4 % and a reduction of the dynamic effects of 32 %.

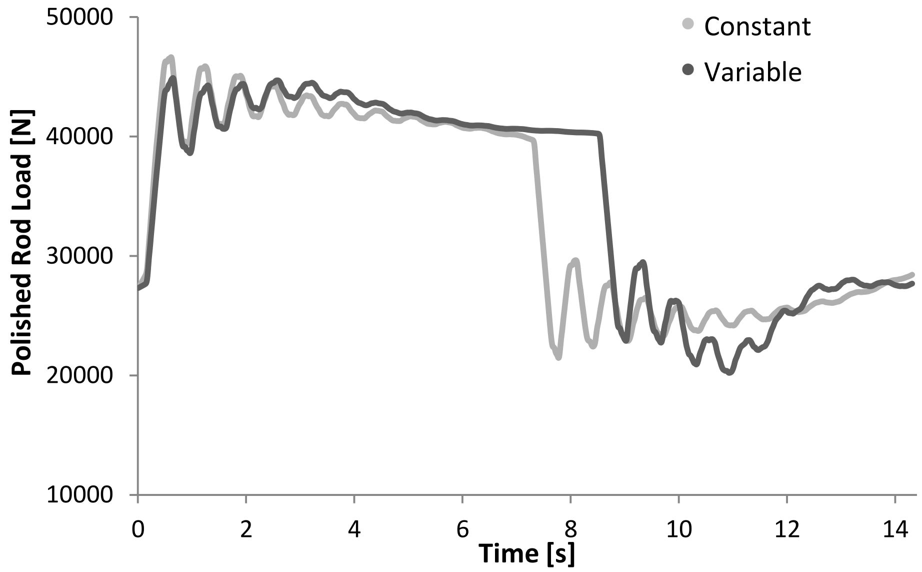

Figure 43: Comparison of the Polished Rod Load as a Function of Time

As far as the MinTorque counterweight setting is concerned, the required maximum counterbalance torque shifts from 71,541 N m (4x OARO at 99.52 cm) to 53,883 N m (4x

OARO at 136.27 cm). Although the peak power rises from 16.59 kW to 19.41 kW, the energy consumption is reduced by 27 %, from 7.14 kWh to 5.24 kWh per hour. Consequently, the daily energy consumption decreases from 171.36 kWh to 125.76 kWh and the daily energy costs from 13.71 € to 10.06 €. Figure 44 compares the energy consumption of one stroke cycle for the MinTorque scenario with a two-quadrant motor (The turning points between up- and downstroke are labelled with TP). In addition, a comparison of the resulting gearbox net torques between the constant and optimized case with the MinTorque counterweight setting is given in Figure 45.

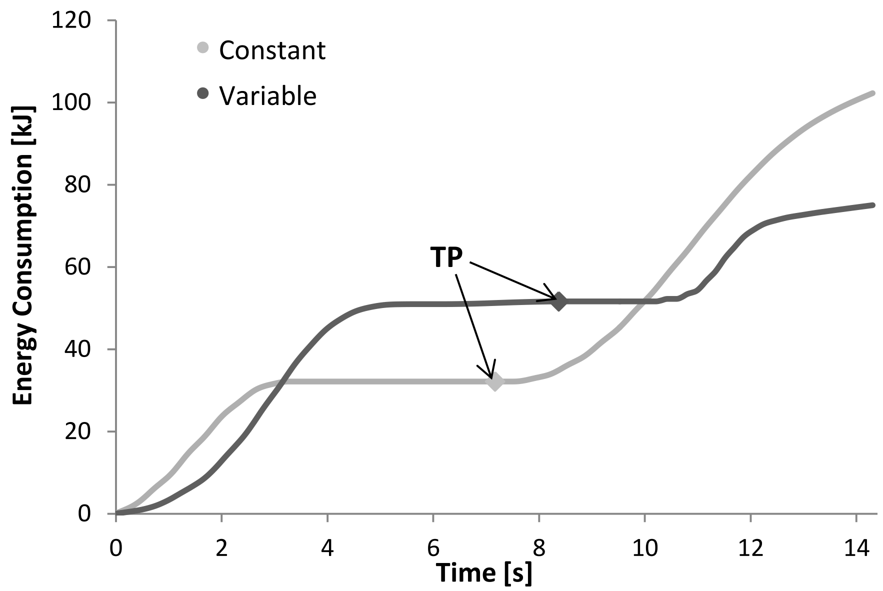

Figure 44: Comparison of the Energy Consumption (MinTorque) with a 2Q Motor

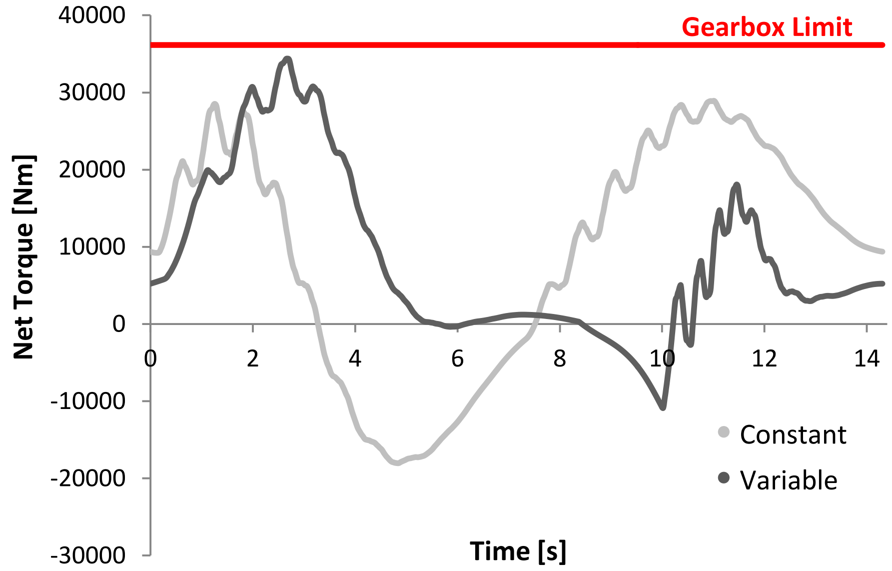

Figure 45: Comparison of the Gearbox Net Torques with the MinTorque Setting

For the minimum energy (MinEnergy) counterweight setting, which is identical to the MinTorque setting for the optimized case, the required maximum counterbalance torque shifts from 47,997 N m (4x OARO at 148.53 cm) to 53,883 N m (4x OARO at 136.27 cm). The peak power and energy consumption decrease from 25.48 kW to 19.41 kW and from 5.57 kWh to 5.24 kWh per hour, respectively. This equals a reduction in energy consumption of 6 %. Consequently, the daily energy consumption decreases from 133.68 kWh to 125.76 kWh and the daily energy costs from 10.69 € to 10.06 €. Figure 46 compares the energy consumption of one stroke cycle for the MinEnergy scenario with a two-quadrant motor. In addition, a comparison of the resulting gearbox net torques between the constant and optimized case with the MinEnergy counterweight setting is given in Figure 47.

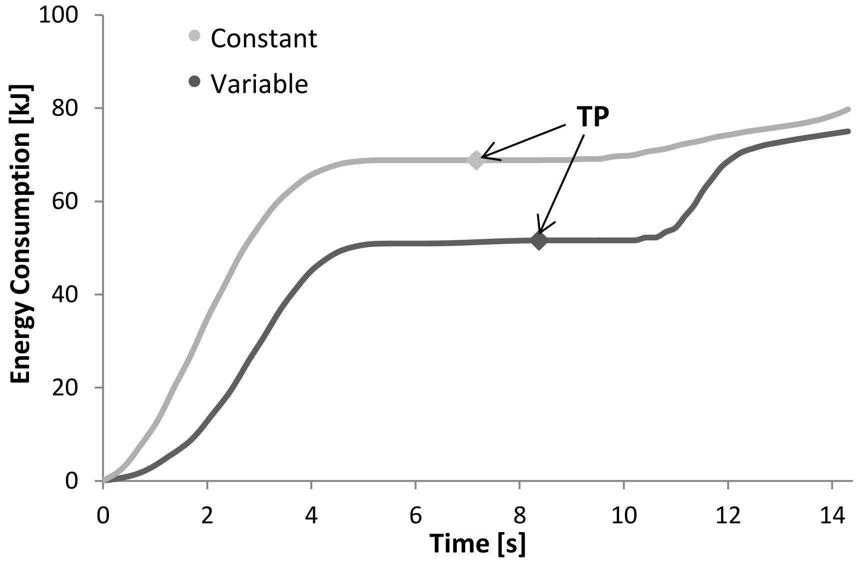

Figure 46: Comparison of the Energy Consumption (MinEnergy) with a 2Q Motor

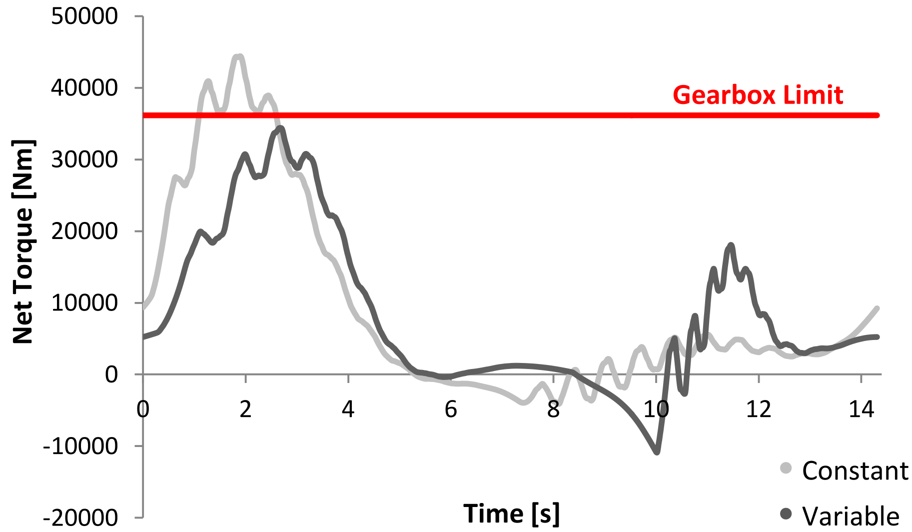

Figure 47: Comparison of the Gearbox Net Torques with the MinEnergy Setting

Considering a four-quadrant motor, the energy consumption reduces by 8 % from 5.28 kWh to 4.88 kWh per hour. Consequently, the daily energy consumption decreases from 126.72 kWh to 117.12 kWh and the daily energy costs from 10.14 € to 9.34 €. These results are equal for both the MinTorque and the MinEnergy counterweight setting, based on the regeneration of energy. Figure 48 compares the energy consumption of one stroke cycle for the MinTorque scenario with a four-quadrant motor.

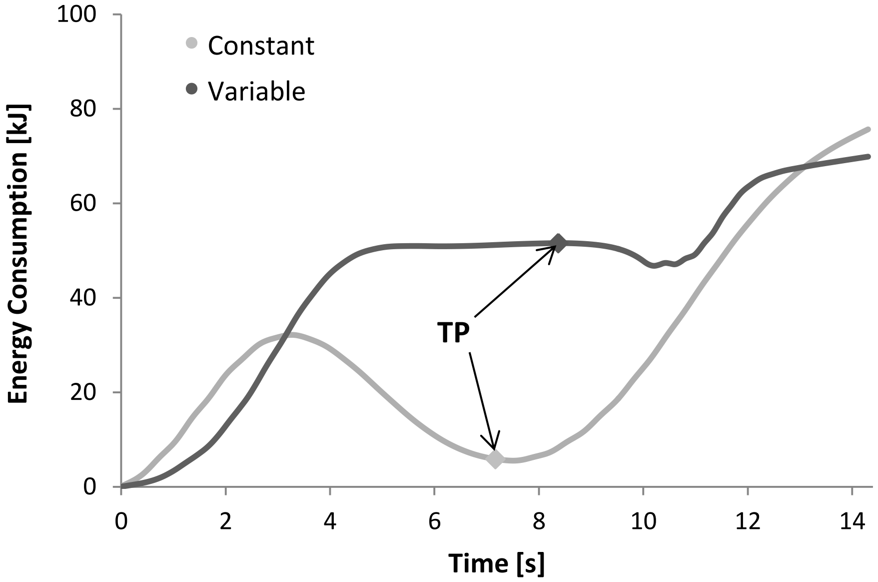

Figure 48: Comparison of the Energy Consumption (MinTorque) with a 4Q Motor

Nevertheless, this work will mainly focus on the scenarios with a two-quadrant motor and will only show the cases with a four-quadrant motor and the resulting regeneration of energy for comparison purposes. The reason for this is that conventional VSD controllers are not able to recover energy since the diode rectifier and DC link capacitor of the system block any current flow that comes from the motor. In addition, this would exceed the voltage rating of these devices and might lead to equipment failure. Therefore it is necessary to use detent prime movers or equip the VSD controller with dynamic braking resistors that dissipate regenerative power as heat. An alternative is given with the specialized REGEN controller that allows for feeding power back into the grid by using line regenerative controls. [3, p. 416] [49] [50]

The main outcomes of the constant and optimized case are summarized in Table 10, for both counterweight settings and the usage of a four-quadrant motor with energy regeneration.

Table 10: Overview of the Results of the Constant and Optimized Case

		MinTorque			MinEnergy			Energy Recovery
Case	PRL [N]	P_{max} [kW]	E_{cons} [kWh/h]	CB_{max} [Nm]	P_{max} [kW]	E_{cons} [kWh/h]	CB_{max} [Nm]	E_{cons} [kWh/h]
Constant	46,645	16.59	7.14	71,541	25.48	5.57	47,997	5.28
Variable	44,902	19.41	5.24	53,883	19.41	5.24	53,883	4.88

4.6 Abaqus Rodstring Simulation

The numerical model used for calculating the forces acting along the rod string in chapter 4.3 has several shortcomings that lead to a not entirely exact prediction of the polished rod loads. Basically the model neglects the effects of mechanical friction: On the one hand, friction forces between the polished rod and the stuffing box as well as the ones in the downhole pump between the pump plunger and the barrel; on the other hand friction forces generated by the contact between tubing and rod string or tubing and rod protectors, since the wellbore is assumed to be perfectly vertical and the existence of protectors is disregarded. Therefore an additional, more exact prediction is obtained by using the sucker rod simulation software developed by Langbauer in 2015 at the Chair of Petroleum and Geothermal Energy Recovery at the Montanuniversitaet Leoben. [38]

The software uses a couple of different MATLAB and Python codes to model the rod string in an Abaqus interface. Similar to the model proposed in this work, the software uses a finite element method to explain the dynamic behaviour of the rod string with the difference that it includes the exact configuration of the wellbore and the rod string as well as a precise simulation of the mechanical friction forces. One of the major benefits of this simulation software is the analysis of the contact forces between the tubing and the rod string that gives a better understanding of mechanical friction and compression forces along the rod string. The program can be used for determining not only the reaction forces at the polished rod, but also the effective stroke length, by analysing the rod displacement at the subsurface pump, or the occurrence of buckling, by looking at the contact forces between the tubing and rod sections without protectors.

The major differences between the Abaqus rodstring simulation software and the original calculation of the polished rod loads are summarized in the following list:

- Input of the exact geometry of the wellbore
- Considering rod protectors attached to the string
- Calculation of friction forces between rod and tubing string
- Calculation of friction forces between rod protectors and tubing string
- Calculation of friction forces between the polished rod and stuffing box
- Calculation of friction forces between pump plunger and barrel
- Determination of the fluid friction with CFD simulations

4.6.1 Software Description

As a first step the sucker rod string needs to be defined by using a numerical mesh, an arrangement of elements and nodes. Nodes are placed on each rod protector as well as on the rod string, exactly between two protectors, which leads to alternating nodes positioned on and off the rod guides. To collect nodes into elements, Abaqus uses a B32 beam element analysis, where each element is composed of three nodes and two integration points at which stresses are observed. These elements and nodes are defined by using a MATLAB file that determines the following parameters and writes them into text files:

- Cartesian coordinates of each node
- Measured depth at each node
- Direction of the tangent at each node
- Nodes and elements within a taper
- Equivalent nodes defined on the tubing string
- Spring elements at each node
- Fluid friction at each node

It is necessary that the nodes are split up in different categories, depending on the rod string taper and the position on or off the protector, and therefore create several text files, in order to accurately predict the occurrence of buckling. In this case, four set of nodes need to be defined: Nodes on the rod string, nodes on the rod protector, nodes on the sinker bars and nodes on the sinker bar protectors. The reason is that for the analysis of buckling only contact forces at nodes on the rod string should be taken into consideration and examined in detail. The spring effect specifies the radial forces on the rod string, generated by the surrounding liquid column. The fluid in the tubing creates not only a buoyancy force that lifts the pump plunger and rod string, but also a radial force that pushes the rod string back to a centralized position when the buoyancy force is large enough to cause buckling. This radial force is considered with a spring action caused by the fluid. Furthermore the fluid friction is calculated based on the liquid characteristics of the produced fluid as well as the rod string properties and is determined by using CFD simulations.

The second step includes the definition of rod loads and movement. The dynamic behaviour of the rod string is described with a partial differential equation that requires two boundary conditions: The time history of the vertical polished rod motion and the immobility of the tubing due to the fact that it is anchored at the bottom. The first condition is determined and placed into text files by using another MATLAB file that calculates load and movement as a function of time at the polished rod based on well specific parameters such a pumping speed, rod diameter, pump size and fluid data. Regarding variable pumping speed scenarios, the MATLAB file needs to be adjusted by importing the time history of the polished rod motion, the angular crankshaft velocity as well as the angular crankshaft acceleration. The second condition is simply reached by editing the code and fixing all nodes on the tubing to their initial position at any time.

As soon as all input text files are generated and the boundary conditions are defined, the main Abaqus code can be started by importing each text file. In the Abaqus code itself, it is necessary to specify the physical properties of the rod material, such as steel density, Poisson's ratio and elastic modulus, to allow the software to accurately model the elastic damping behaviour of the rod string. Also the lengths and diameters of each taper need to be typed in once again, together with information about the clearance and friction factor between each rod string section or rod protector and the tubing. Moreover a 'non-structural mass' is defined, accounting for the weight of auxiliary equipment such as rod guides, and paraffin wax that may be deposited along the rod string. Finally, the pumping speed needs to be entered once again, to determine the time span of one complete stroke interval. The simulation is programmed to monitor three seconds the initial static state to predict the gravity followed by two pump cycles.

When Abaqus has finished the simulation, it is possible to illustrate the time history of several output parameters at each node along the rod string. The most important are the reaction forces, contact forces, stresses as well as movement, or more precisely spatial displacement. In addition, Abaqus generates a number of output files where all these parameters are placed. As a next step, a program written in Python collects the data of these output files and provides an information folder, where the contact force, stress and displacement information of each node is stored for several time points. This data is used by another MATLAB file that generates an information cube based on these three parameters. Besides the mentioned parameters, the Python code creates three extra files describing the time increments, the reaction forces at the polished rod and the vertical displacement at the pump plunger. All information will be processed in a final MATLAB file that can be used for calculating and illustrating the power requirements and energy consumption for one stroke cycle, similar as shown in chapter 4.4, or plotting the dynamometer cards at the polished rod or the downhole pump. [38]

4.6.2 Effective Stroke Length

Apart from the determination of the reaction forces at the polished rod and the detection of buckling by analysing the contact forces at each node, the Abaqus software can be used to identify the effective stroke length of the pump plunger. The downhole stroke length of the plunger may deviate clearly from the surface stroke length that is adjusted and defined at the polished rod. The main reason for this phenomenon is the elastic and dynamic behaviour of the tubing and rod string that get stretched by their own weight and the variable fluid load. Since these elongations affect the plunger stroke, it will differ from the surface stroke and will be shorter by the sum of tubing and rod string stretch. An exact prediction of the effective stroke length can be obtained with the Abaqus software by visualizing the spatial displacement as a function of time at the lowermost node and reading out the travelled distance. This knowledge allows for the calculation of further production related parameters. The volume of liquid passing through the pump during one pumping cycle equals the product of effective stroke length and the cross sectional area of the pump plunger. By additionally considering the average pumping speed and the pump efficiency, the total production rate can be calculated, as seen in **eq.68** [3, p. 425].

$$Q_{tot} = S_{eff} * A_{pl} * N_{avg} * \eta_{Pump} * 60 * 24 \qquad (68)$$

with:

Q_{tot} Total production rate [m³/day]

S_{eff} Effective stroke length [m]

A_{pl} Cross section of the plunger [m²]

N_{avg} Average pumping speed [spm]

η_{Pump} Efficiency of the pump [-]

To determine the amount of oil produced within one day, this value is simply multiplied with one minus the given water cut. Furthermore, the amount of energy needed per gross volume pumped as well as the electricity costs per gross volume pumped can be calculated by dividing the daily energy consumption and electricity costs with the total production rate.

With the knowledge of the volumetric production rate, it is also possible to calculate the hydraulic power needed for lifting the fluids. In general, it is necessary to overcome the hydrostatic pressure to bring wellbore fluids from the downhole pump to the surface and therefore the required energy depends on the mixture density, the dynamic fluid level as well as the production rate. Lea and Minissale came up with the following relation, as seen in **eq.69** [3, p. 361].

$$E_{hydr} = \frac{Q_{tot} * L_{dyn} * \rho_{mix} * g}{24 * 1000 * 3600} \qquad (69)$$

with:

E_{hydr} Hydraulic energy used for lifting [kWh/h]

Q_{tot} Total production rate [m³/day]

L_{dyn} Dynamic fluid level from the surface [m]

ρ_l Density of the fluid mixture [kg/m³]

g Gravitational constant 9.81 [m/s²]

At this point, both the input and output energy of the sucker rod pumping system are identified. The output energy equals the hydraulic energy used for lifting the fluids as explained in this chapter and the input energy equals the electrical energy consumption of the prime mover as demonstrated in chapter 4.4.3. The ratio between these two values is defined as the overall energy efficiency of the pumping system and describes the amount of energy that is lost across the system, from the electric motor to the downhole pump. These losses include electrical losses in the prime mover, mechanical losses in the surface equipment as well as friction and hydraulic losses in the downhole equipment and the wellbore. [3, pp. 361, 364-368, 425-426]

4.7 Impact on the V-Belt Drive

Since the impact of frequency-elastic operations on the V-belt drive is disregarded during the design phase of the optimal velocity function, this chapter will point out the influence and check the differences in terms of technical feasibility. The most important design criterion for the selection of the right V-belt is the maximum stress arising in the drive system and therefore this value is determined for the current installation of the sample well, for both constant and optimized scenario. In general, the biggest loads occur at the contact point of the drive pulley and the tight side of the belt and consist of tension, centrifugal as well as bending forces, as illustrated in Figure 49. In addition to the calculation sequence described in this chapter, an extract of the used Excel sheet can be seen in Appendix E. [51, pp. 603-604]

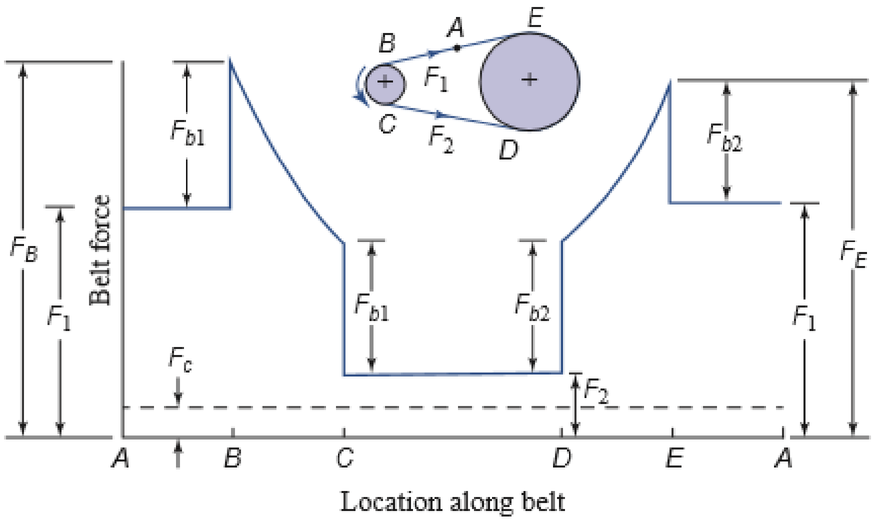

Figure 49: Forces in the V-Belt Drive [52, p. 605]

4.7.1 Tension Force

The tension force in the belt is caused by the torque transmitted from the prime mover to the smaller sheave and due to friction of the rotation of the driver pulley, the tight side tension is always greater than the slack side tension. To determine the tight side tension of the belt, Eytelwein’s formula can be used as seen in **eq.70** [52, p. 606].

$$F_1' = \frac{e^{\mu'\beta_1}}{e^{\mu'\beta_1 - 1}} \frac{2\,T_{mot}}{d_{PM}} \tag{70}$$

where β_1 is the contact angle between the prime mover sheave and the V-belt and can be determined with a simple geometric consideration in function of the sheave sizes and their spacing, shown in **eq.71** [52, pp. 598-599]

$$\beta_1 = \pi - 2\sin^{-1}\left(\frac{d_{GB} - d_{PM}}{e}\right) \tag{71}$$

and μ' is the theoretical friction value, a correction of the actual friction factor by including the groove angle of the sheaves, as seen in **eq.72** [51, p. 600]. This is necessary since the wedging action between the V-belt and the grooves increases the normal force on the belt element.

$$\mu' = \frac{\mu}{\sin(\frac{\varphi}{2})} \tag{72}$$

Furthermore, the motor torque that is transmitted to the smaller sheave equals the net torque required at the gearbox divided by the surface mechanical efficiency that accounts for the mechanical friction losses in the V-belt drive, the gearbox and the pumping unit.

4.7.2 Centrifugal Force

The centrifugal force represents the inertia effect of the V-belt and depends on the cross section of the belt, the density of the material as well as the belt velocity, shown in **eq.73** [51, p. 601]

$$F_c = \rho_B \, A_B \, BV^2 \tag{73}$$

whereby the belt velocity can be calculated from the instantaneous motor speed and the diameter of the prime mover sheave, as seen in **eq.74** [3, p. 232].

$$BV = \frac{N_{mot} \; d_{PM} \, \pi}{60 * 1000} \tag{74}$$

In general this force is comparatively small and therefore neglected in the calculation of the maximum stress. However, for higher and especially non-uniform belt velocities, it is essential to consider the inertia and acceleration effects of the belt as well.

4.7.3 Bending Force

Finally, the bending force needs to be taken into account that is caused by wrapping the belt around the sheaves. The smaller the sheave diameter is, the larger becomes the degree of bending and therefore the bending force reaches its maximum around the drive pulley. An approximation of the force is given in **eq.75** [51, p. 604] that depends on the elastic modulus of the belt material, the cross section of the belt as well as the ratio between effective belt thickness and diameter of the prime mover sheave.

$$F_{b1} \approx E_B \, \frac{t_B}{d_{PM}} \, A_B \tag{75}$$

4.7.4 Maximum Stress

The sum of these forces divided by the cross section of the belt represents the maximum stress that acts on the V-belt and must not exceed the strength of the selected belt. The formula of the maximum stress can be seen in **eq.76** [51, p. 604].

$$\sigma_{max} = \frac{F'_1}{A_B} + \frac{F_c}{A_B} + \frac{F_{b1}}{A_B} \tag{76}$$

with:

σ_{max}	Maximum stress in the V-belt [N/m²]
F'_1	Tight side tension force [N]
F_c	Centrifugal force [N]
F_{b1}	Bending force around the prime mover sheave [N]
A_B	Cross section of the V-belt [m²]

Concerning the sample well, a power band from ConCar is used that consists of four identical V-belts connected by a rubber fabric coat at the top. The properties and dimensions of each V-belt are standardized according to DIN 7753-1 [53, p. 442] with the selected belt having a designation code of SPC 22. The material of the V-belt contains polyester and polyamide cords covered in synthetic fabrics and rubber with an averaged density of 1200 kg/m³ and an elastic modulus of 300 N/mm². Furthermore, the trapezium-shaped V-belt has an effective thickness of 4.8 mm and a cross section of 267.75 mm². With a prime mover sheave diameter of 240 mm, a gearbox sheave diameter of 1130 mm and a spacing between the sheaves of 1.6 m, the length of the V-belt is 5.6 m and the wrap angle around the drive pulley 148° or 2.58 rad. The friction factor between the belt and sheave material is 0.5 and together with a groove angle of 34° or 0.59 rad, the corrected friction factor reaches a value of 1.71. [51, pp. 967, 973-974] [54]

With a constant motor speed of 594 rpm, the constant scenario results in a belt velocity of 7.47 m/s and with a varying motor speed between 332 rpm and 1100 rpm, the belt velocity of the optimized scenario ranges from 4.17 m/s to 13.82 m/s. All the provided information can now be used, together with the time history of the motor torque (counterweights at the MinTorque position), to determine the maximum stress acting on the V-belt. The constant scenario leads to a value of 13.21 N/mm² and the optimized scenario to a value of 14.56 N/mm². This means that the maximum stress at the contact point of the drive pulley and the tight side of the belt is increased by 10.22 % and the safety buffer to the averaged V-belt strength of 20 N/mm² decreased by 19.88 %, when applying frequency-elastic operations instead of conventional ones. In addition, it must be assumed that the varying belt velocity of frequency-elastic operations leads to an increased slip of the V-belt and consequently to a decrease in power transmission from the electric prime mover to the gearbox. As a rule of thumb, a properly designed V-belt drive for conventional pumping operations has slip factor of about 2 %, however the exact values can only be obtained with experimental studies in the field. As far as the model presented in this thesis is concerned, it will be therefore necessary to measure the slip factor of both operation modes, once the conventional one and once the frequency-elastic one, in the field with exactly the same power band and V-belt drive configuration. The percent change can be then used to update the predicted values of the surface mechanical efficiency from chapter 4.4.2, which are so far assumed to be constant, to get a more accurate simulation of the power requirements and the energy consumption. [51, p. 967]

5 Results: Frequency-Elastic Operations

5.1 Simulation Scenarios Overview

Several simulation scenarios are performed for the sample well by using the model described in chapter 4, at different average pumping speeds. The pumping speeds are chosen to represent the theoretical operating range of the pumping unit from low to high pumping speeds:

- Scenario A: Intermediate pumping speed of 5 spm
- Scenario B: Low pumping speed of 3.2 spm
- Scenario C: High pumping speed of 10 spm

For each scenario, three simulations are performed: The first one describes a conventional operation case without the usage of a VSD controller and a constant crankshaft velocity, however the second and the third one describe optimized operation cases with the usage of a VSD unit and consequently a varying crankshaft velocity, to minimize once the loads acting at the polished rod and once the energy consumption. The cases are labelled as follows:

- ‘Constant’ (Grey) – Conventional pumping operation with constant pumping speed
- ‘VarLoad’ (Red) – Optimized operation to minimize the peak polished rod loads
- ‘VarEnergy’ (Blue) – Optimized operation to minimize the energy consumption

The improvements and deteriorations of the optimized cases, in terms of polished rod loads, energy usage as well as energy efficiency of the pumping system, are demonstrated and compared to the constant drive scenario. In addition, the simulations are analysed on technical feasibility for the current well installation by looking at the limitations of the system components and if necessary by suggesting a replacement for individual elements, as well as economic profitability by demonstrating the changes in capital and operational expenditures of the optimized cases compared to the constant one.

All simulations consider two different counterweight settings, the one resulting in the minimum peak torque and the one resulting in the minimum energy consumption, as well as two different prime movers, once a two-quadrant motor with a detent power meter and once a four-quadrant motor with a non-detent power meter allowing the regeneration of electrical energy. The variation in angular crankshaft velocity for the optimized cases is determined based on the polished rod loads calculated with the original simplified method shown in chapter 4.3 and the optimization principle in chapter 4.5, however for the actual results the loads are determined as described in chapter 4.6 by adopting the preceding profiles of the polished rod position as well as angular crankshaft velocity and acceleration.

5.2 Scenario A: Pumping Speed of 5 SPM

The first scenario is performed with an average pumping speed of 5 spm. The Constant case has a fixed angular crankshaft velocity of 0.524 rad/s. The VarLoad case has an upstroke ratio of 0.577 and a varying angular crankshaft speed between 0.286 rad/s at the turning points and 0.620 rad/s at the halfway point of the upstroke or 0.953 rad/s at the halfway point of the downstroke. The VarEnergy case has an upstroke ratio of 0.5 and a varying angular crankshaft speed between 0.242 rad/s at the turning points and 0.805 rad/s at the halfway point of the up- and downstroke. The resulting profile of the polished rod position for the three different cases is illustrated in Figure 50. Further input functions such as the angular velocity and acceleration of the crankshaft and walking beam can be seen in Appendix F.

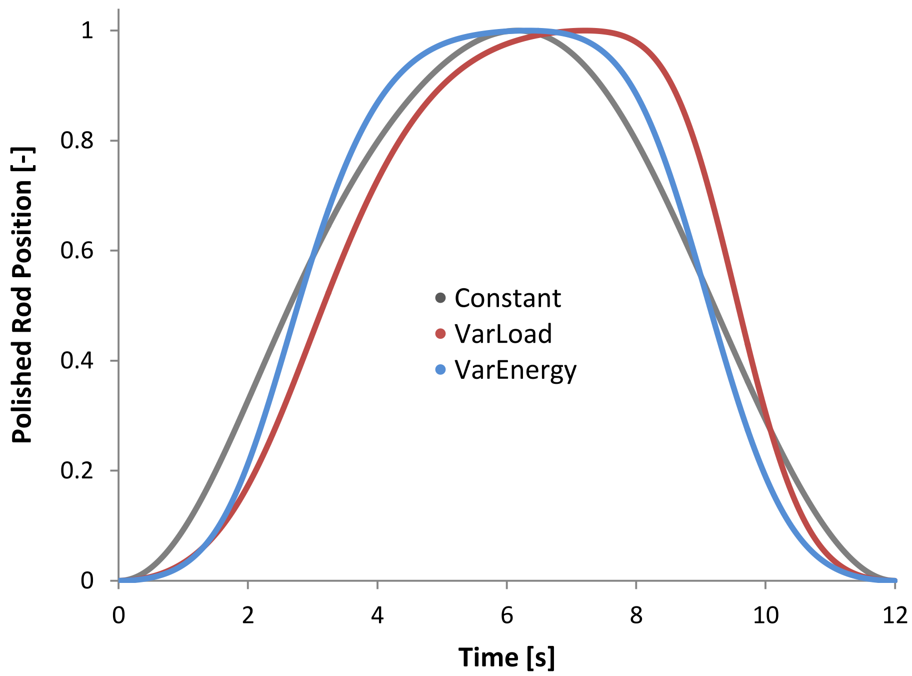

Figure 50: Scenario A: Comparison of the Polished Rod Position

As far as the peak polished rod load is concerned, the Constant case reaches a value of 49,829 N. By applying the VarLoad case, this value can be reduced by 2 % to 48,938 N, however the VarEnergy case leads to a slight increase of 3 % to 51,452 N. A comparison of the time history of the polished rod loads is shown in Figure 51. In addition, a comparison of the dynamometer cards is shown in Figure 52, with the polished rod loads being illustrated as a function of the polished rod displacement.

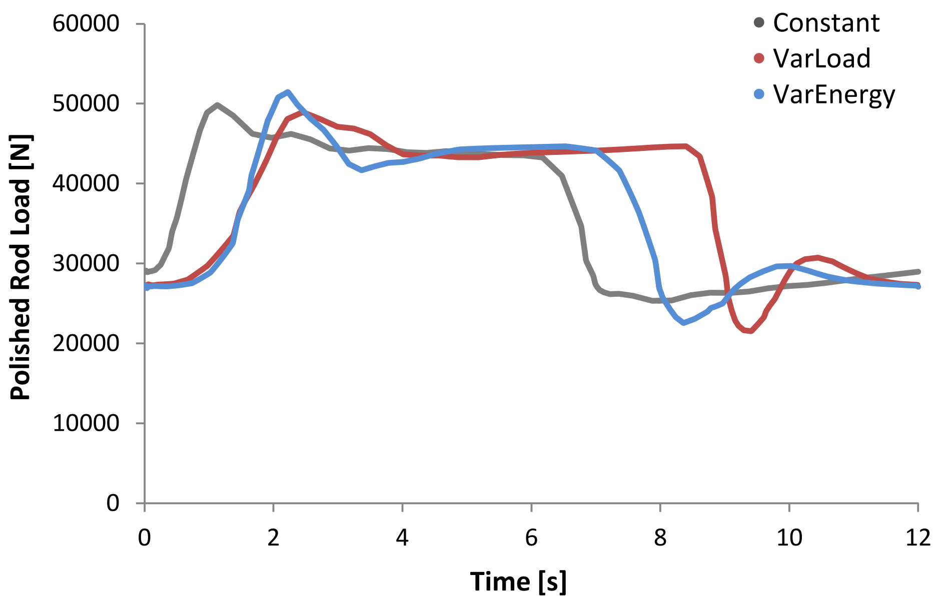

Figure 51: Scenario A: Comparison of the Polished Rod Loads

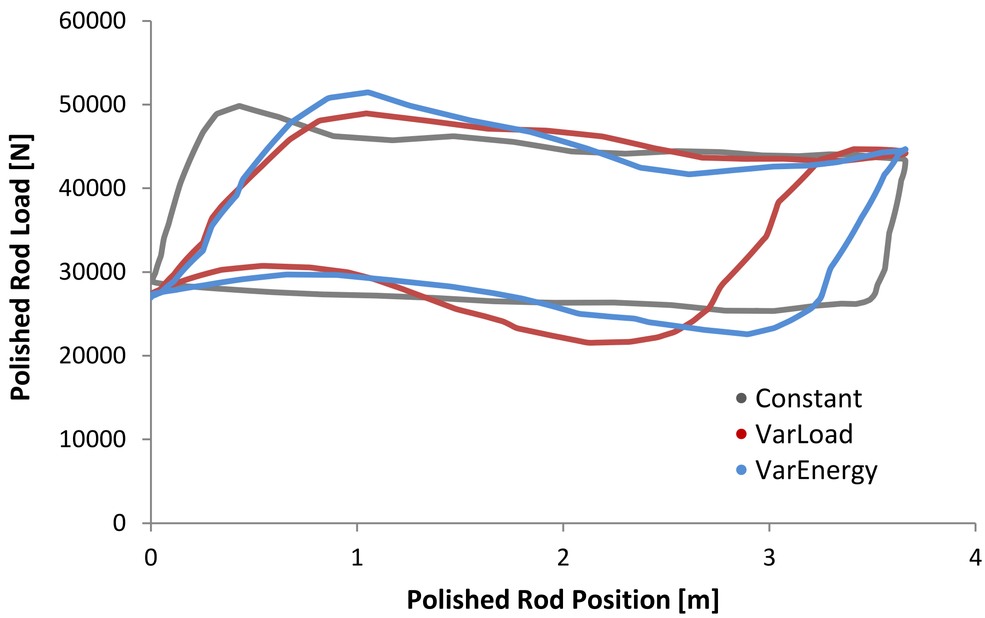

Figure 52: Scenario A: Comparison of the Dynamometer Cards

All three cases are simulated with two different counterweight settings: The MinTorque and the MinEnergy installation. An overview of the mounted counterweights, as well as the resulting maximum counterbalance torque is shown in Table 11.

Table 11: Scenario A: Comparison of the Installed Counterweights

Case	**MinTorque**		**MinEnergy**	
	Counterweights	*Counterbalance*	*Counterweights*	*Counterbalance*
Constant	4x OARO at 84.81 cm	78,605 N m	4x OARO at 141.17 cm	51,529 N m
VarLoad	4x OARO at 124.02 cm	59,769 N m	4x OARO at 126.47 cm	58,592 N m
VarEnergy	4x OARO at 99.52 cm	71,541 N m	4x OARO at 133.82 cm	55,061 N m

5.2.1 MinTorque Counterweight Setting

As far as the MinTorque configuration is concerned, the Constant case leads to a peak power of 21.99 kW. For the VarLoad case, this value is increased by 18 % to 26.02 kW and for the VarEnergy case by 25 % to 27.48 kW.

Considering a **two-quadrant motor** with a detent power meter, the Constant case results in an energy consumption of 9.43 kWh per hour and daily electricity costs of 18.11 €. For the VarLoad case these values can be decreased by 37 % to 5.96 kWh per hour as well as 11.44 € per day and for the VarEnergy case by 30 % to 6.61 kWh per hour as well as 12.69 € per day. A comparison of the energy consumption over the course of one stroke of the three different cases is illustrated in Figure 53.

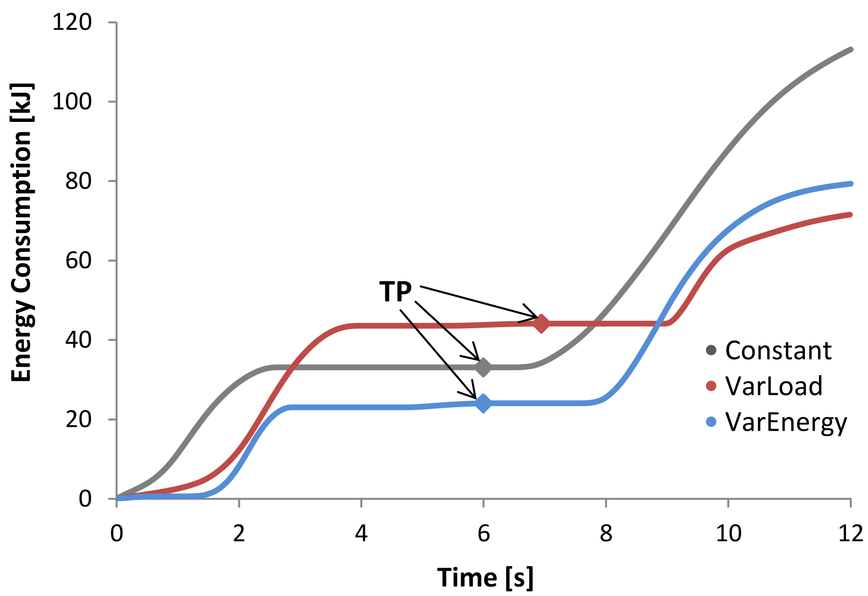

Figure 53: Scenario A: Comparison of the Energy Usage (MinTorque) with a 2Q Motor

With all three cases resulting in an effective stroke length of 3.11 m, the total production rate reaches a value of 22.85 m³/day and the oil production rate a value of 3.30 m³/day. Given that the dynamic fluid level reaches a depth of 827 m, the hydraulic power used for lifting the fluid column is 2.12 kWh per hour, leading to a total system efficiency of 22.50 % for the Constant case, 35.57 % for the VarLoad case and 32.08 % for the VarEnergy case. The electricity costs per gross volume pumped are 0.79 €/m³ for the Constant case, 0.50 €/m³ for the VarLoad case, and 0.56 €/m³ for the VarEnergy case.

Considering a **four-quadrant motor** with a non-detent power meter, the Constant case results in an energy consumption of 6.59 kWh per hour and daily electricity costs of 12.65 €. For the VarLoad case these values can be decreased by 30 % to 4.64 kWh per hour as well as 8.91 € per day and for the VarEnergy case by 20 % to 5.26 kWh per hour as well as 10.10 € per day. The total system efficiency is 32.17 % for the Constant case, 45.67 % for the VarLoad case and 40.29 % for the VarEnergy case. The electricity costs per gross volume pumped are 0.55 €/m³ for the Constant case, 0.39 €/m³ for the VarLoad case, and 0.44 €/m³ for the VarEnergy case. These results are equal for both MinTorque and MinEnergy installations, based on the regeneration of energy. A comparison of the energy consumption over the course one stroke of the three different cases is illustrated in Figure 54.

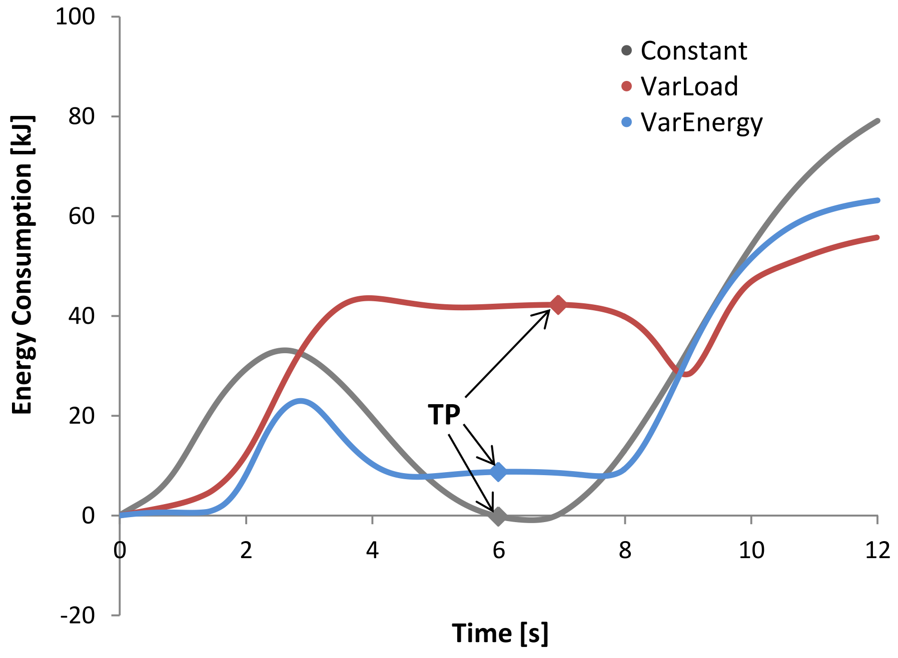

Figure 54: Scenario A: Comparison of the Energy Usage (MinTorque) with a 4Q Motor

5.2.2 MinEnergy Counterweight Setting

As far as the MinEnergy configuration is concerned, the Constant case leads to a peak power of 32.98 kW. For the VarLoad case, this value is decreased by 19 % to 26.76 kW and for the VarEnergy case increased by 22 % to 40.24 kW.

Considering a **two-quadrant motor** with a detent power meter, the Constant case results in an energy consumption of 7.17 kWh per hour and daily electricity costs of 13.77 €. For the VarLoad case these values can be decreased by 17 % to 5.95 kWh per hour as well as 11.42 € per day and for the VarEnergy case by 21 % to 5.68 kWh per hour as well as 10.91 € per day. The total system efficiency is 29.57 % for the Constant case, 35.62 % for the VarLoad case and 37.34 % for the VarEnergy case. The electricity costs per gross volume pumped are 0.60 €/m³ for the Constant case, 0.50 €/m³ for the VarLoad case, and 0.48 €/m³ for the VarEnergy case. A comparison of the energy consumption over the course of one stroke of the three different cases is illustrated in Figure 55.

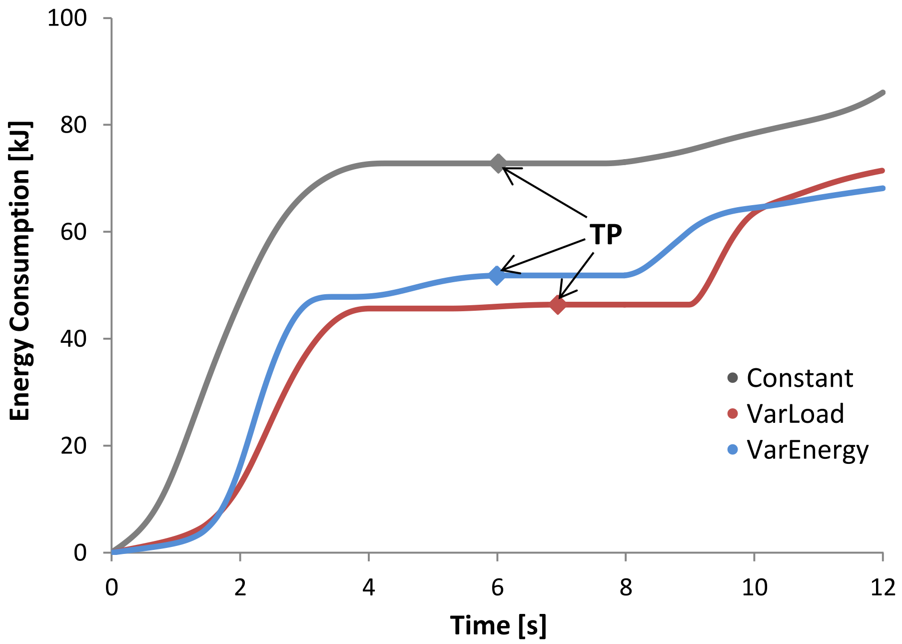

Figure 55: Scenario A: Comparison of the Energy Usage (MinEnergy) with a 2Q Motor

The main outcomes of the three different cases are summarized in Table 12, for both counterweight settings and the usage of a four-quadrant motor. In addition the results are compared to the ones with the simplified prediction of the polished rod loads.

Table 12: Scenario A: Overview and Comparison of the Results

5 SPM		**Abaqus Rodstring Simulation**			**Original Calculation Method**		
		Constant	*VarLoad*	*VarEnergy*	*Constant*	*VarLoad*	*VarEnergy*
	PRL [N]	49,829	48,938	51,452	48,477	46,181	48,463
MinTorque	P_{max} [kW]	21.99	26.02	27.48	22.13	25.88	27.31
	E_{cons} [kWh/h]	9.43	5.96	6.61	9.07	6.52	6.94
	CB_{max} [Nm]	78,605	59,769	71,541	72,719	53,883	64,478
MinEnergy	P_{max} [kW]	32.98	26.76	40.24	32.27	25.88	36.98
	E_{cons} [kWh/h]	7.17	5.95	5.68	7.09	6.52	6.22
	CB_{max} [Nm]	51,529	58,592	55,061	47,997	53,883	52,706
Energy Recovery	P_{max} [kW]	21.99	26.02	27.48	22.13	25.88	27.31
	E_{cons} [kWh/h]	6.59	4.64	5.26	6.51	5.95	6.15
	CB_{max} [Nm]	78,605	59,769	71,541	72,719	53,883	64,478

5.2.3 Technical Feasibility

Since the pumping system is originally designed for constant pumping operations with 4.19 spm, three aspects of the sucker rod pumping system needs to be checked on technical feasibility for each simulation case. These components are the gear reducer, the electric prime mover as well as the sucker rod string.

As far as the gearbox is concerned, the operation is limited to the designed torque rating of the installed gear reducer. In this case, with a 320 D gearbox the maximum allowable peak net torque is fixed at a value of 36,155 N m. Table 13 shows the resulting peak net torques as well as the gearbox loading for all three cases for both counterweight settings. The exceeding loading factors are indicated in red.

Table 13: Scenario A: Comparison of the Peak Gearbox Torques and Loadings

Case	**MinTorque**		**MinEnergy**	
	Peak Torque	*Gearbox Loading*	*Peak Torque*	*Gearbox Loading*
Constant	32,127 N m	88.86 %	48,191 N m	133.29 %
VarLoad	36,076 N m	99.78 %	37,051 N m	102.48 %
VarEnergy	28,978 N m	80.15 %	43,026 N m	119 %

All cases are accomplishable with the gear reducer currently in place, when their counterweights are set to the MinTorque scenario. However for the MinEnergy scenario, all cases require the installation of a gearbox one size larger, 456 D with a torque rating of 51,521 N m or, since unavailable at OMV Austria, 640 D with a torque rating of 72,310 N m.

To determine if the installed 40 HP (30 kW) NEMA D motor is large enough for each simulation case, the minimum required motor size needs to be calculated, which equals the product of the average mechanical motor power and the cyclic load factor. An exact prediction of the cyclic load factor is given with the ratio between the root mean square and the average values of the gearbox net torque, as shown in chapter 2.2.2. An overview of the average mechanical motor power, the cyclic load factors and the required motor sizes is given in Table 14, for all three cases considering both counterweight settings.

Table 14: Scenario A: Comparison of Required Motor Sizes

Case	**MinTorque**			**MinEnergy**		
	P_{Mot}	*CLF*	P_{Req}	P_{Mot}	*CLF*	P_{Req}
Constant	5.60 kW	2.08	11.64 kW	5.6 kW	1.86	10.42 kW
VarLoad	3.95 kW	2.29	9.03 kW	3.95 kW	2.27	9.07 kW
VarEnergy	4.47 kW	2.22	9.93 kW	4.47 kW	2.08	9.30 kW

Since the required motor sizes are clearly below the nameplate power, the installed electric motor can be used for all simulation cases and counterweight settings.

The integrity of the rod string is analysed by checking the tensile strength of the polished rod as well as the occurrence of buckling that might lead to breaks or a decrease in fatigue endurance. The biggest rod loads act at the uppermost rod string section, namely the polished rod. With the peak polished rod loads of 49,829 N, 48,938 N and 51,452 N, all three cases stay clearly below the tensile strength of the polished rod that is specified at 114 kN. Moreover, buckling does not occur for any case, since the contact forces between tubing and rod string are zero at any point in time, along the wellbore. Finally, based on the increased deviation between minimum and maximum loads for the optimized cases, it is necessary to determine the fatigue endurance limits as well. They are calculated at the uppermost rod string section below the polished rod and can be determined with the modified Goodman diagram from chapter 2.1.2.1, under consideration of the rod string properties and the forces acting at polished rod. The cross section of the rod string is 387.95 mm², the tensile strength of the rod material 793 N/mm² and the safety factor is assumed to be 0.9. Table 15 shows the minimum and maximum loads acting at the uppermost rod string section for all three cases as well as their corresponding stresses. In addition, the calculated fatigue endurance limits are presented.

Table 15: Scenario A: Comparison of the Fatigue Endurance Limits

	Constant	**VarLoad**	**VarEnergy**
F_{max}	49,8289 N	48,938 N	51,452 N
S_{max}	128.44 N/mm²	126.15 N/mm²	132.63 N/mm²
F_{min}	25,339 N	21,540 N	22,558 N
S_{min}	65.31 N/mm²	55.52 N/mm²	58.15 N/mm²
S_a	211.49 N/mm²	206.53 N/mm²	207.86 N/mm²
S_{max}/S_a	60.73 %	61.08 %	63.81 %

With the maximum stresses being clearly below the calculated allowable stresses, the fatigue endurance limit is not reached for any case.

5.2.4 Economic Profitability

Apart from the savings in electricity costs, another important indicator for the economic feasibility of frequency-elastic operations is the payout. This period is defined as the time it takes for a project to pay for itself and ends when the savings in operational expenditures equals the additional capital investment costs for the project. In general, the gains and losses in terms of oil production need to be considered as well, but since the production rate does not change for any simulation scenario, these factors can be neglected.

The savings in operational expenditures are determined by taking the reduction of energy consumption times the averaged electricity price of 0.08 €/kWh and the additional investment costs by adding up the expenses of supplementary equipment that is needed for frequency-elastic operations. These costs consist mainly of the purchase price and installation costs of a suitable VSD. The best fitting VSD, available at OMV Austria, has a power rating of 55 kW and is offered by SchneiderElectric for 10,400 € and associated costs for the installation amount to about 10,000 €. In case the well has no EMSR-Installation on site, additional expenses of 20,000 € must be considered for the implementation. [14] Furthermore, the prime mover sheave and the counterweights need to be replaced/adjusted and perfectly fitted for the given conditions, which amounts to 900 € and 970 €, respectively. [54] The increase in capital expenditures adds up to 22,270 €, with available EMSR-Installation, and 42,270 €, without available EMSR-Installation, as summarized in the list below:

Purchase price of the VSD	*10,400 €*
Installation costs of the VSD	*+ 10,000 €*
Replacement of the prime mover sheave	*+ 900 €*
Adjustment of the counterweight position	*+ 970 €*
(EMSR-Installation)	*(+ 20,000 €)*
Total increase in capital expenditures	***= 22,270 €***
	(= 42,270 €)

An overview of the yearly energy savings in euros and the resulting payout time in years is given Table 16 for the frequency-elastic cases, considering the MinTorque setting, the MinEnergy setting as well as the regenerative motor configuration.

Table 16: Scenario A: Comparison of the Energy Savings and Payout Time

Case	MinTorque		MinEnergy		Energy Recovery	
	Savings	*Payout*	*Savings*	*Payout*	*Savings*	*Payout*
VarLoad	2,432 €	9.2 (17.4) y	855 €	26.0 (49.4) y	1,367 €	16.3 (30.9) y
VarEnergy	1,976 €	11.3 (21.4) y	1,044 €	21.3 (40.5) y	932 €	23.9 (45.5) y

5.3 Scenario B: Pumping Speed of 3.2 SPM

The second scenario is performed with an average pumping speed of 3.2 spm. The Constant case has a fixed angular crankshaft velocity of 0.335 rad/s. The VarLoad case, which equals the VarEnergy case, has an upstroke ratio of 0.584 and a varying angular crankshaft speed between 0.186 rad/s at the turning points and 0.388 rad/s at the halfway point of the upstroke or 0.619 rad/s at the halfway point of the downstroke. The resulting profile of the polished rod position for the two different cases is illustrated in Figure 56. Further input functions such as the angular velocity and acceleration of the crankshaft and walking beam can be seen in Appendix G.

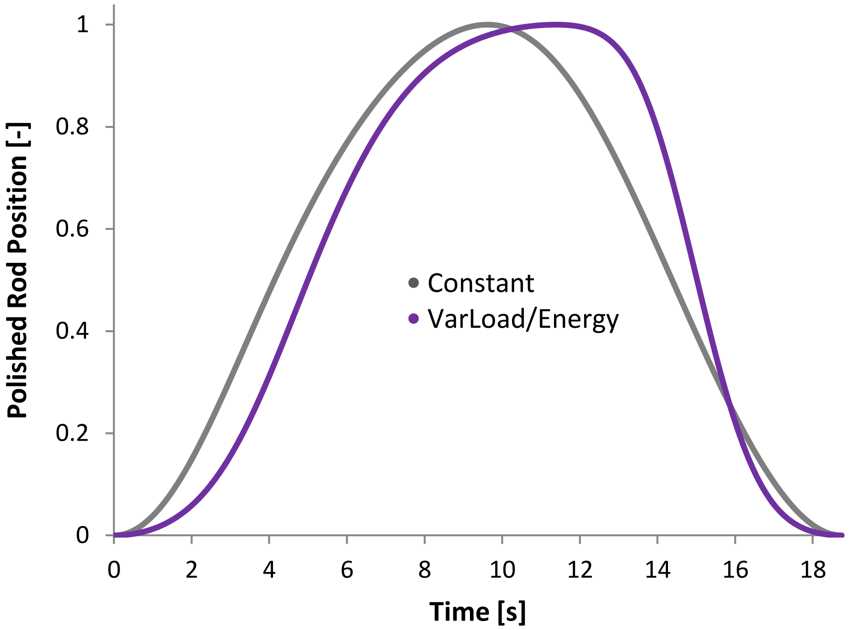

Figure 56: Scenario B: Comparison of the Polished Rod Position

As far as the peak polished rod load is concerned, the Constant case reaches a value of 46,708 N. By applying the VarLoad/Energy case, this value can be reduced by 1 % to 46,356 N. A comparison of the time history of the polished rod loads is shown in Figure 57

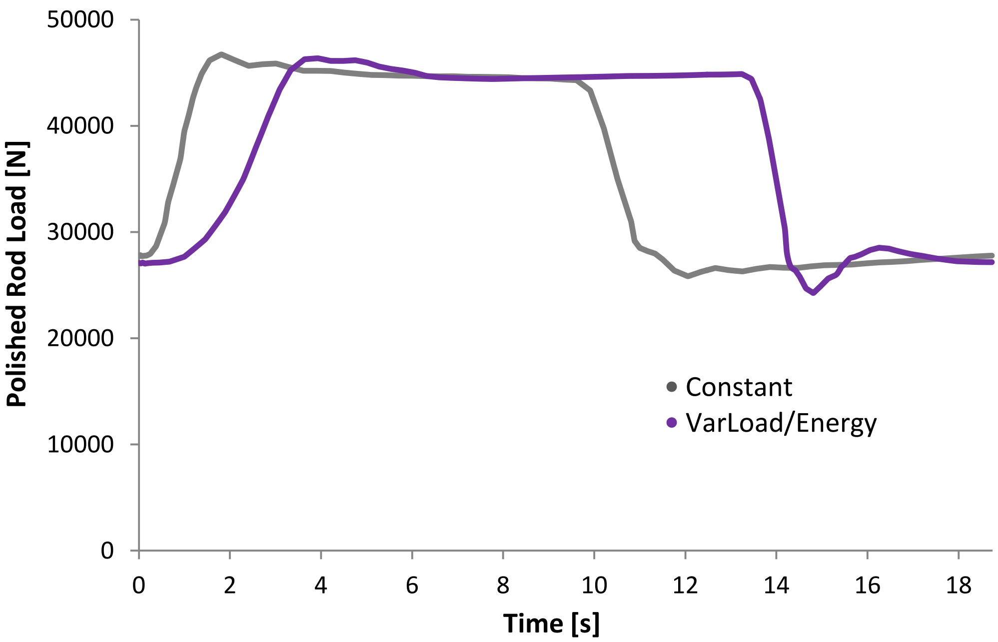

Figure 57: Scenario B: Comparison of the Polished Rod Loads

In addition, a comparison of the dynamometer cards is shown in Figure 58, with the polished rod loads being illustrated as a function of the polished rod displacement.

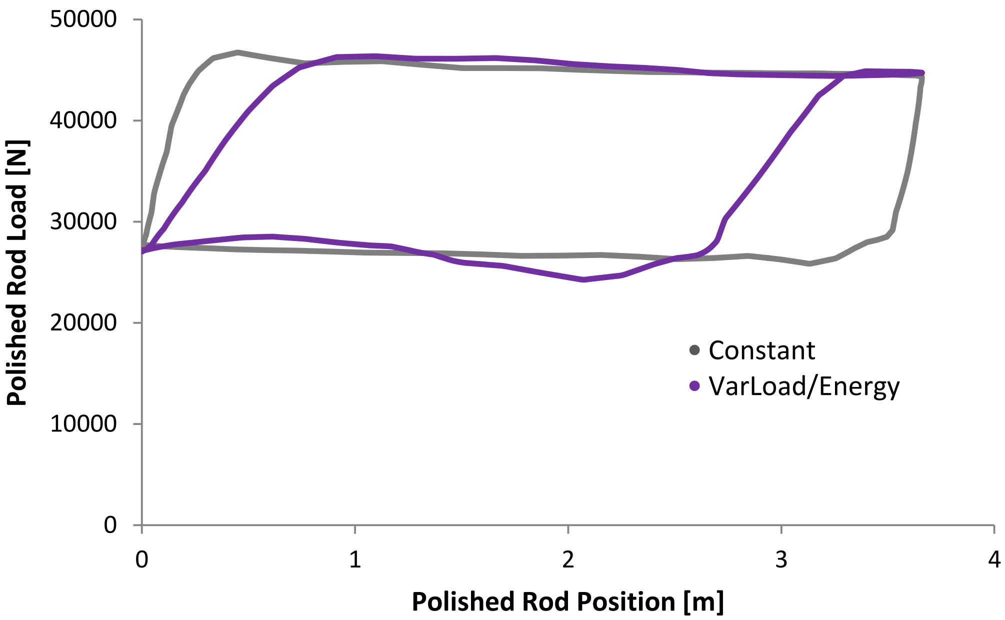

Figure 58: Scenario B: Comparison of the Dynamometer Cards

Both cases are simulated with two different counterweight settings: The MinTorque and the MinEnergy installation. An overview of the mounted counterweights, as well as the resulting maximum counterbalance torque is shown in Table 17.

Table 17: Scenario B: Comparison of the Installed Counterweights

Case	**MinTorque**		**MinEnergy**	
	Counterweights	*Counterbalance*	*Counterweights*	*Counterbalance*
Constant	4x OARO at 94.62 cm	73,896 N m	4x OARO at 136.27 cm	53,883 N m
VarLoad/Energy	4x OARO at 121.57 cm	60,947 N m	4x OARO at 121.57 cm	60,947 N m

5.3.1 MinTorque Counterweight Setting

As far as the MinTorque configuration is concerned, the Constant case leads to a peak power of 12.06 kW. For the VarLoad/Energy case, this value is increased by 18 % to 14.23 kW.

Considering a **two-quadrant motor** with a detent power meter, the Constant case results in an energy consumption of 5.30 kWh per hour and daily electricity costs of 10.18 €. For the VarLoad/Energy case these values can be decreased by 35 % to 3.47 kWh per hour as well as 6.66 € per day. A comparison of the energy consumption over the course of one stroke of both cases is illustrated in Figure 59.

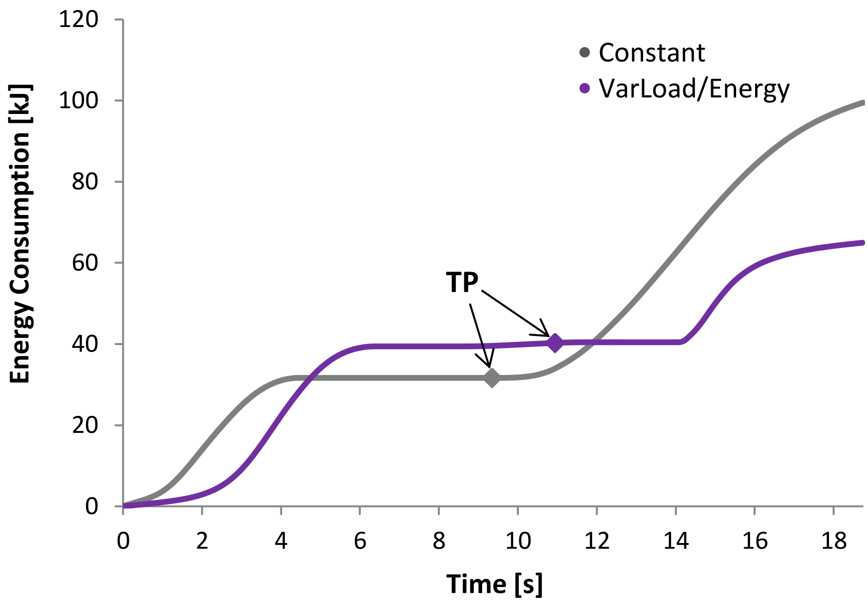

Figure 59: Scenario B: Comparison of the Energy Usage (MinTorque) with a 2Q Motor

With both cases resulting in an effective stroke length of 3.11 m the total production rate reaches a value of 14.63 m³/day and the oil production rate a value of 2.11 m³/day. Given that the dynamic fluid level reaches a depth of 827 m, the hydraulic power used for lifting the fluid column is 1.36 kWh per hour, leading to a total system efficiency of 25.59 % for the Constant case as well as 39.18 % for the VarLoad/Energy case. The electricity costs per gross volume pumped are 0.70 €/m³ for the Constant case and 0.45 €/m³ for the VarLoad/Energy case.

Considering a **four-quadrant motor** with a non-detent power meter, the Constant case results in an energy consumption of 4.23 kWh per hour and daily electricity costs of 8.12 €. For the VarLoad/Energy case these values can be decreased by 30 % to 2.96 kWh per hour as well as 5.68 € per day. The total system efficiency is 32.06 % for the Constant case as well as 45.79 % for the VarLoad/Energy case. The electricity costs per gross volume pumped are 0.56 €/m³ for the Constant case and 0.39 €/m³ for the VarLoad/Energy case. These results are equal for both MinTorque and MinEnergy installations, based on the regeneration of energy. A comparison of the energy consumption over the course one stroke of both cases is illustrated in Figure 60.

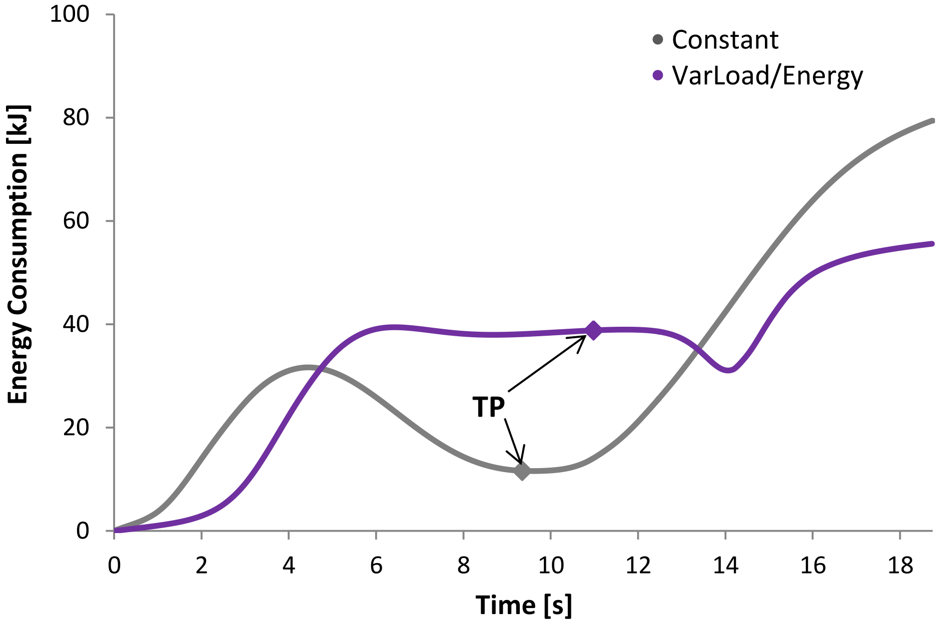

Figure 60: Scenario B: Comparison of the Energy Usage (MinTorque) with a 4Q Motor

5.3.2 MinEnergy Counterweight Setting

As far as the MinEnergy configuration is concerned, the Constant case leads to a peak power of 17.65 kW. For the VarLoad/Energy case, this value is decreased by 19 % to 14.23 kW.

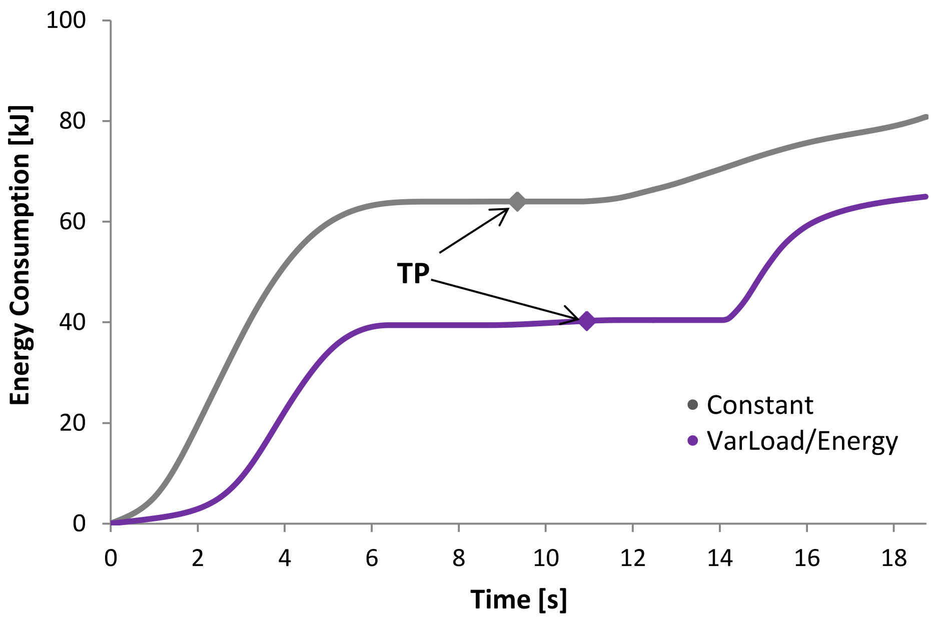

Figure 61: Scenario B: Comparison of the Energy Usage (MinEnergy) with a 2Q Motor

Considering a **two-quadrant motor** with a detent power meter, the Constant case results in an energy consumption of 4.31 kWh per hour and daily electricity costs of 8.28 €. For the VarLoad/Energy case these values can be decreased by 20 % to 3.47 kWh per hour as well as 6.66 € per day. The total system efficiency is 31.50 % for the Constant case as well 39.18 % for the VarLoad/Energy case. The electricity costs per gross volume pumped are 0.57 €/m³ for the Constant case and 0.45 €/m³ for the VarLoad/Energy case. A comparison of the energy consumption over the course of one stroke of both cases is illustrated in Figure 61.

The main outcomes of the two cases are summarized in Table 18, for both counterweight settings and the usage of a four-quadrant motor. In addition the results are compared to the ones with the simplified prediction of the polished rod loads.

Table 18: Scenario B: Overview and Comparison of the Results

3.2 SPM		**Abaqus Rodstring Simulation**		**Original Calculation Method**	
		Constant	*VarLoad/Energy*	*Constant*	*VarLoad/Energy*
	PRL [N]	46,708	46,356	44,749	43,569
MinTorque	P_{max} [kW]	12.06	14.23	11.53	13.45
	E_{cons} [kWh/h]	5.30	3.47	5.06	3.81
	CB_{max} [Nm]	73,896	60,947	69,187	56,238
MinEnergy	P_{max} [kW]	17.65	14.23	17.73	13.98
	E_{cons} [kWh/h]	4.31	3.47	4.03	3.78
	CB_{max} [Nm]	53,883	60,947	47,997	53,883
Energy Recovery	P_{max} [kW]	12.06	14.23	11.53	13.45
	E_{cons} [kWh/h]	4.23	2.96	3.98	3.65
	CB_{max} [Nm]	73,896	60,947	69,187	56,238

5.3.3 Technical Feasibility

Also the simulation cases with an average pumping speed of 3.2 spm are checked on technical feasibility of the pumping system, in consideration of the gearbox, the electric prime mover and the rod string. As far as the gear reducer is concerned, the peak net torques are not allowed to surpass the fixed gearbox rating of 36,155 N, once again. Table 19 shows the resulting peak net torques as well as the gearbox loading for both cases and counterweight settings. The exceeding loading factors are indicated in red.

Table 19: Scenario B: Comparison of the Peak Gearbox Torques and Loadings

Case	**MinTorque**		**MinEnergy**	
	Peak Torque	*Gearbox Loading*	*Peak Torque*	*Gearbox Loading*
Constant	27,522 N m	76.12 %	40,303 N m	111.47 %
VarLoad/Energy	32,174 N m	88.99 %	32,174 N m	88.99 %

The VarLoad/Energy case is accomplishable with the gear reducer currently in place for the counterweight setting that results in MinTorque and MinEnergy at the same time. However the Constant case is only feasible with the counterweights set to the MinTorque position, since for the MinEnergy scenario, the installation of a gearbox one size larger is required, 456 D with a torque rating of 51,521 N m or, since unavailable at OMV Austria, 640 D with a torque rating of 72,310 N m.

Also the minimum required motor size is determined once again, by calculating the average mechanical motor power and the cyclic load factor, to check if the installed 40 HP (30 kW) NEMA D motor is large enough. An overview of the calculated values and the required motor sizes is given in Table 20, for both cases and counterweight settings.

Table 20: Scenario B: Comparison of Required Motor Sizes

Case	**MinTorque**			**MinEnergy**		
	P_{Mot}	*CLF*	P_{Req}	P_{Mot}	*CLF*	P_{Req}
Constant	3.60 kW	1.72	6.21 kW	3.60 kW	1.62	5.83 kW
VarLoad/Energy	2.52 kW	1.99	5.03 kW	2.52 kW	1.99	5.03 kW

Since the required motor sizes are clearly below the nameplate power, the installed electric motor can be used for all simulation cases and counterweight settings.

Finally, the integrity of the rod string is analysed once more by checking the tensile strength of the polished rod as well as the occurrence of buckling that might lead to breaks or a decrease in fatigue endurance. The biggest rod loads act at the uppermost rod string section, namely the polished rod. With the peak polished rod loads of 46,708 N and 46,356 N, both cases stay below the tensile strength of the polished rod that is specified at 114 kN. Moreover, buckling does not occur for any case, since the contact forces between the tubing and the rod string are zero at any point in time, along the wellbore. Finally, based on the increased deviation between minimum and maximum loads for the optimized case, it is necessary to determine the fatigue endurance limits as well. They are calculated at the uppermost rod string section below the polished rod and can be determined with the modified Goodman diagram from chapter 2.1.2.1, under consideration of the rod string properties and the forces acting at polished rod. The cross section of the rod string is 387.95 mm², the tensile strength of the rod material 793 N/mm² and the safety factor is assumed to be 0.9. Table 21 shows the minimum and maximum loads acting at the uppermost rod string section for both cases as well as their corresponding stresses. In addition, the calculated fatigue endurance limits are presented.

Table 21: Scenario B: Comparison of the Fatigue Endurance Limits

	Constant	**VarLoad/Energy**
F_{max}	46,708 N	46,356 N
S_{max}	120.4 N/mm²	119.49 N/mm²
F_{min}	25,848 N	24,261 N
S_{min}	66.63 N/mm²	62.54 N/mm²
S_a	212.16 N/mm²	210.09 N/mm²
S_{max}/S_a	56.75 %	56.88 %

With the maximum stresses being clearly below the calculated allowable stresses, the fatigue endurance limit is not reached for any case.

5.3.4 Economic Profitability

The economic feasibility of the optimized case is checked again by calculating the payout time. The savings in operational expenditures equals the reduction in energy consumption times the averaged electricity price of 0.08 €/kWh and the total increase in capital expenditures amounts to 22,270 €, including purchase and installation costs of the 55 kW VSD as well as replacement costs for the prime mover sheave and counterweights. Without an available EMSR-Installation on site the total increase in capital expenditures rises to 42,270 €. An overview of the yearly energy savings in euros and the resulting payout time in years is given in Table 22 for the frequency-elastic case considering the MinTorque setting, the MinEnergy setting as well as the regenerative motor configuration.

Table 22: Scenario B: Comparison of the Energy Savings and Payout Time

Case	MinTorque		MinEnergy		Energy Recovery	
	Savings	*Payout*	*Savings*	*Payout*	*Savings*	*Payout*
VarLoad/ Energy	1,282 €	17.4 (33.0) y	589 €	37.8 (71.8) y	890 €	25.0 (47.5) y

5.4 Scenario C: Pumping Speed of 10 SPM

The third scenario is performed with an average pumping speed of 10 spm. The Constant case has a fixed angular crankshaft velocity of 1.047 rad/s. The VarLoad case has an upstroke ratio of 0.526 and a varying angular crankshaft speed between 0.714 rad/s at the turning points and 1.275 rad/s at the halfway point of the upstroke or 1.496 rad/s at the halfway point of the downstroke. The VarEnergy case has an upstroke ratio of 0.5 and a varying angular crankshaft speed between 0.598 rad/s at the turning points and 1.496 rad/s at the halfway point of the up- and downstroke. The resulting profile of the polished rod position for the three different cases is illustrated in Figure 62. Further input functions such as the angular velocity and acceleration of the crankshaft and walking beam can be seen in Appendix H.

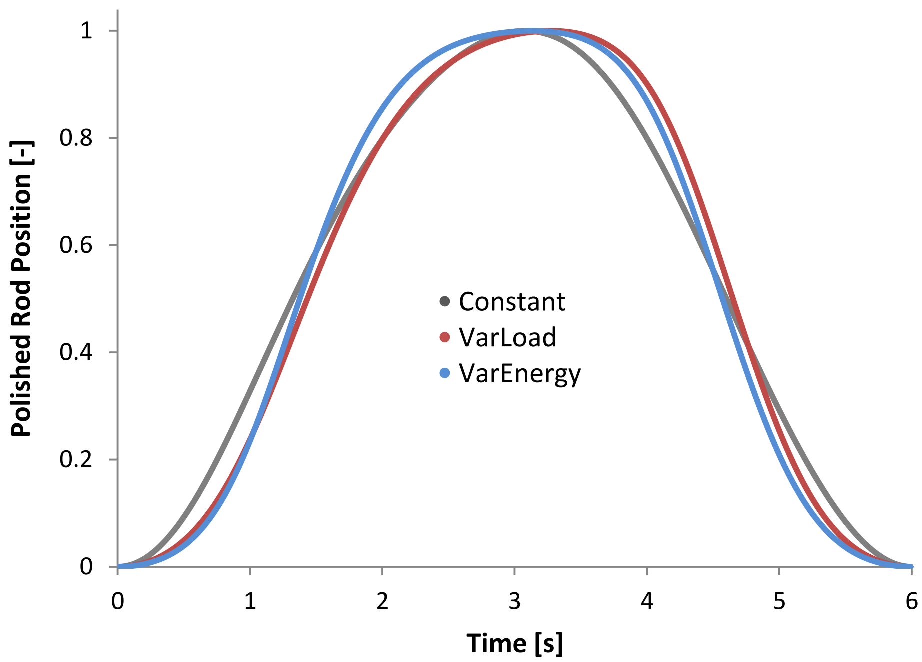

Figure 62: Scenario C: Comparison of the Polished Rod Position

As far as the peak polished rod load is concerned, the Constant case reaches a value of 64,043 N. By applying the VarLoad case, this value is slightly increased by 1 % to 64,777 N, despite an opposite forecast by the initial model and an even bigger increase of 8 % to 69,423 N can be witnessed regarding the VarEnergy case. A comparison of the time history of the polished rod loads is shown in Figure 63. In addition, a comparison of the dynamometer cards is shown in Figure 64, with the polished rod loads being illustrated as a function of the polished rod displacement.

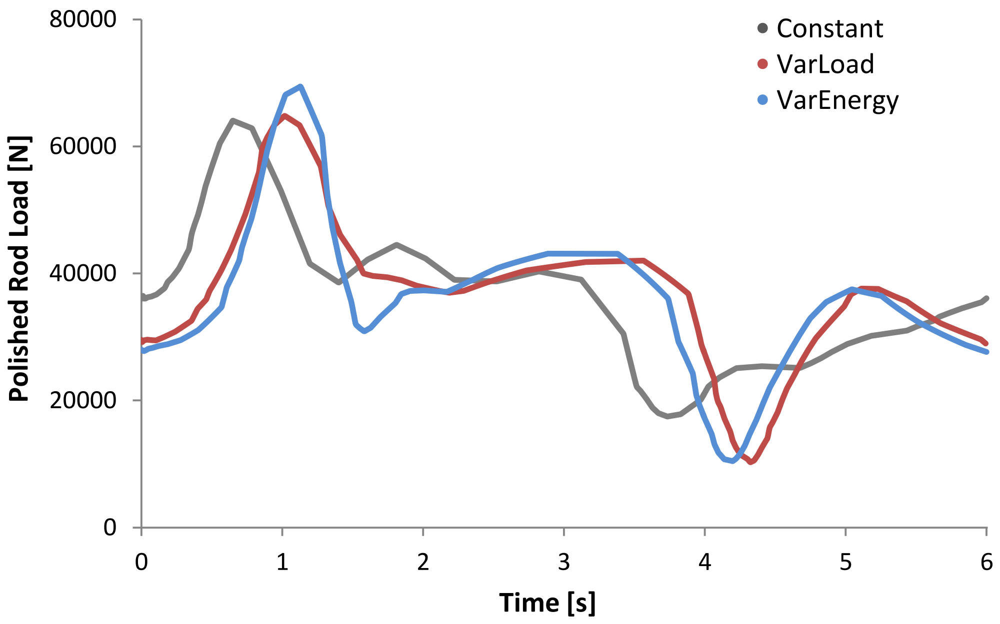

Figure 63: Scenario C: Comparison of the Polished Rod Loads

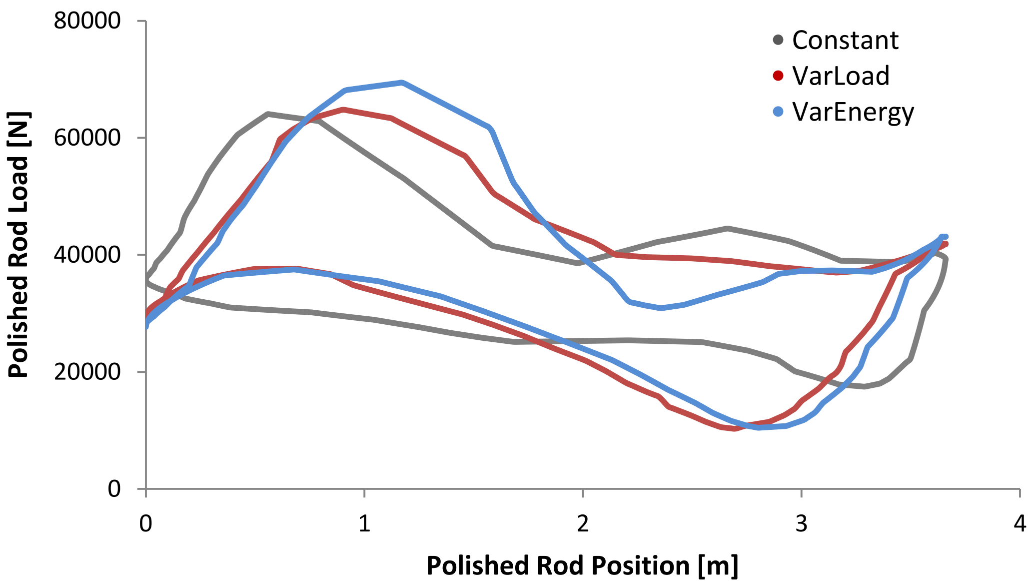

Figure 64: Scenario C: Comparison of the Dynamometer Cards

All three cases are simulated with two different counterweight settings: The MinTorque and the MinEnergy installation. An overview of the mounted counterweights, as well as the resulting maximum counterbalance torque is shown in Table 23.

Table 23: Scenario C: Comparison of the Installed Counterweights

Case	**MinTorque**		**MinEnergy**	
	Counterweights	*Counterbalance*	*Counterweights*	*Counterbalance*
Constant	4x OARO at 50.51 cm	95,085 N m	4x OARO at 143.62 cm	50,352 N m
VarLoad	4x OARO at 99.52 cm	71,541 N m	4x OARO at 138.72 cm	52,706 N m
VarEnergy	4x OARO at 84.81 cm	78,605 N m	4x OARO at 133.82 cm	55,061 N m

5.4.1 MinTorque Counterweight Setting

As far as the MinTorque configuration is concerned, the Constant case leads to a peak power of 70.79 kW. For the VarLoad case, this value is increased by 6 % to 75.17 kW and for the VarEnergy case by 11 % to 78.54 kW.

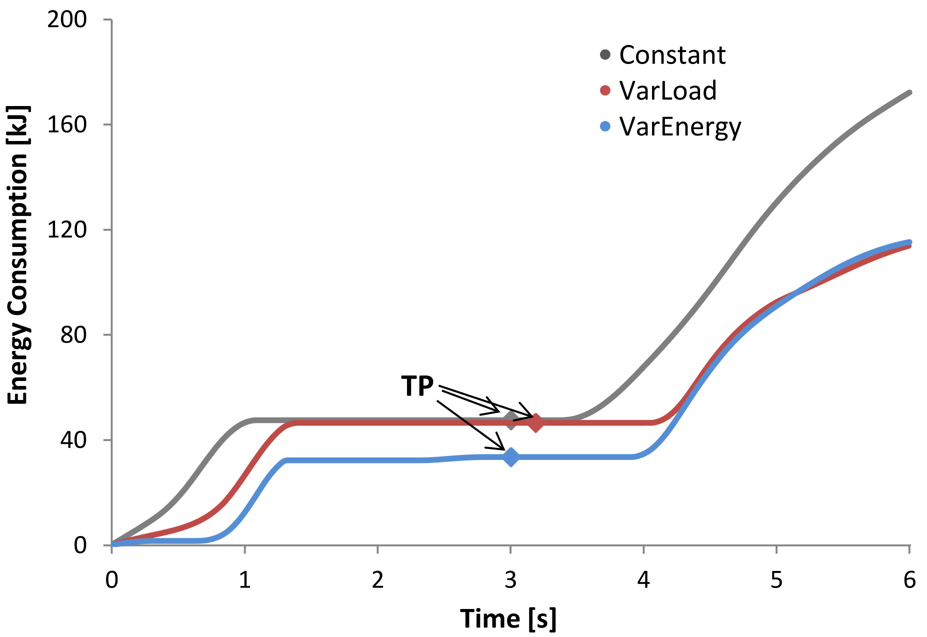

Figure 65: Scenario C: Comparison of the Energy Usage (MinTorque) with a 2Q Motor

Considering a **two-quadrant motor** with a detent power meter, the Constant case results in an energy consumption of 28.70 kWh per hour and daily electricity costs of 55.10 €. For the VarLoad case these values can be decreased by 34 % to 18.99 kWh per hour as well as 36.46 € per day and for the VarEnergy case by 33 % to 19.22 kWh per hour as well as 36.9 € per day. A comparison of the energy consumption over the course of one stroke of the three different cases is illustrated in Figure 65.

With all three cases resulting in an effective stroke length of 3.11 m the total production rate reaches a value of 45.71 m³/day and the oil production rate a value of 6.60 m³/day. Given that the dynamic fluid level reaches a depth of 827 m, the hydraulic power used for lifting the fluid column is 4.24 kWh per hour, leading to a total system efficiency of 14.78 % for the Constant case, 22.34 % for the VarLoad case and 22.07 % for the VarEnergy case. The electricity costs per gross volume pumped are 1.21 €/m³ for the Constant case, 0.80 €/m³ for the VarLoad case, and 0.81 €/m³ for the VarEnergy case.

Considering a **four-quadrant motor** with a non-detent power meter, the Constant case results in an energy consumption of 13.85 kWh per hour and daily electricity costs of 26.59 €. For the VarLoad case these values can be decreased by 15 % to 11.84 kWh per hour as well as 22.73 € per day and for the VarEnergy case by 21 % to 10.91 kWh per hour as well as 20.95 € per day. The total system efficiency is 30.64 % for the Constant case, 35.84 % for the VarLoad case and 38.89 % for the VarEnergy case. The electricity costs per gross volume pumped are 0.58 €/m³ for the Constant case, 0.50 €/m³ for the VarLoad case, and 0.46 €/m³ for the VarEnergy case. These results are equal for both MinTorque and MinEnergy installations, based on the regeneration of energy. A comparison of the energy consumption over the course one stroke of the three different cases is illustrated in Figure 66.

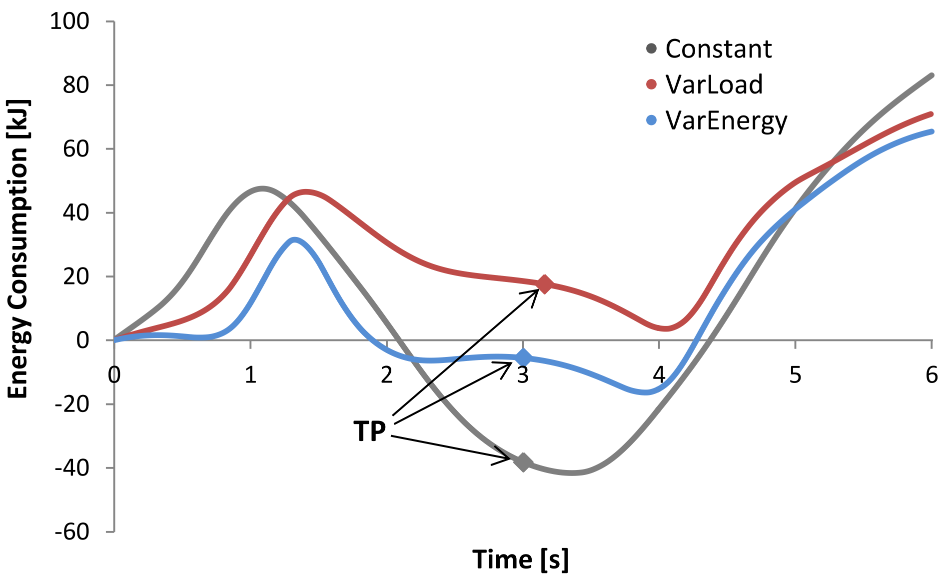

Figure 66: Scenario C: Comparison of the Energy Usage (MinTorque) with a 4Q Motor

5.4.2 MinEnergy Counterweight Setting

As far as the MinEnergy configuration is concerned, the Constant case leads to a peak power of 109.97 kW. For the VarLoad case, this value is decreased by 8 % to 100.80 kW and for the VarEnergy case increased by 12 % to 123.16 kW.

Considering a **two-quadrant motor** with a detent power meter, the Constant case results in an energy consumption of 18.52 kWh per hour and daily electricity costs of 35.56 €. For the VarLoad case these values can be decreased by 12 % to 16.26 kWh per hour as well as 31.22 € per day and for the VarEnergy case by 16 % to 15.55 kWh per hour as well as 29.86 € per day. The total system efficiency is 22.91 % for the Constant case, 26.10 % for the VarLoad case and 27.28 % for the VarEnergy case. The electricity costs per gross volume pumped are 0.78 €/m³ for the Constant case, 0.68 €/m³ for the VarLoad case, and 0.65 €/m³ for the VarEnergy case. A comparison of the energy consumption over the course of one stroke of the three different cases is illustrated in Figure 67.

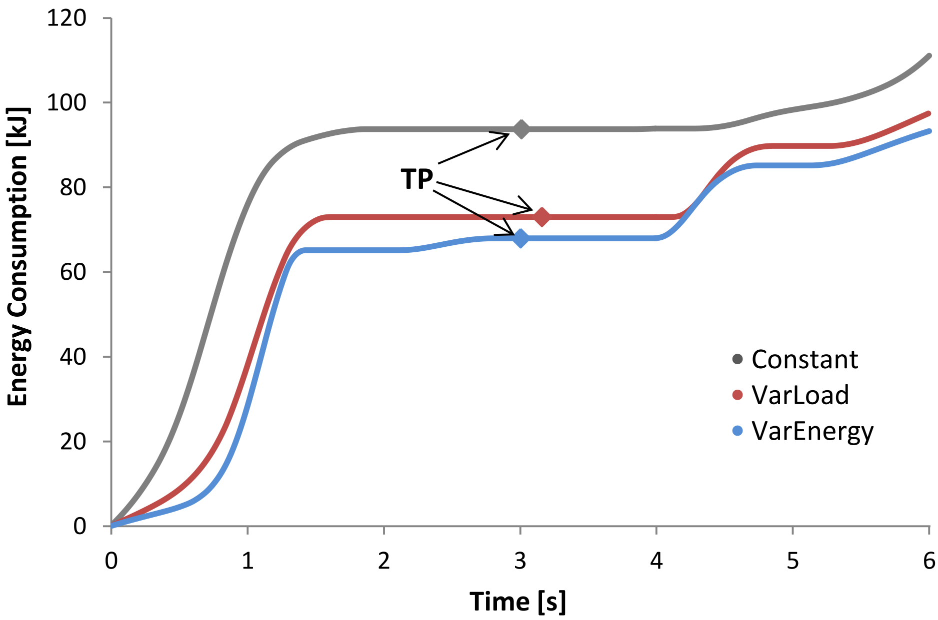

Figure 67: Scenario C: Comparison of the Energy Usage (MinEnergy) with a 2Q Motor

The main outcomes of the three different cases are summarized in Table 24, for both counterweight settings and the usage of a four-quadrant motor. In addition the results are compared to the ones with the simplified prediction of the polished rod loads.

Table 24: Scenario C: Overview and Comparison of the Results

10 SPM		**Abaqus Rodstring Simulation**			**Original Calculation Method**		
		Constant	*VarLoad*	*VarEnergy*	*Constant*	*VarLoad*	*VarEnergy*
	PRL [N]	64,043	64,777	69,423	59,505	56,698	59,747
MinTorque	P_{max} [kW]	70.79	75.17	78.54	70.56	69.88	71.76
	E_{cons} [kWh/h]	28.70	18.99	19.22	26.25	17.91	17.72
	CB_{max} [Nm]	95,085	71,541	78,605	82,136	55,061	62,124
MinEnergy	P_{max} [kW]	109.97	100.8	123.16	95.32	77.31	92.98
	E_{cons} [kWh/h]	18.52	16.26	15.55	20.14	17.83	16.77
	CB_{max} [Nm]	50,352	52,706	55,061	45,643	50,352	51,529
Energy Recovery	P_{max} [kW]	70.79	75.17	78.54	70.56	69.88	71.76
	E_{cons} [kWh/h]	13.85	11.84	10.91	13.51	11.53	10.64
	CB_{max} [Nm]	95,085	71,541	78,605	82,136	55,061	62,124

5.4.3 Technical Feasibility

Also the simulation cases with an average pumping speed of 10 spm are checked on technical feasibility of the pumping system, in consideration of the gearbox, the electric prime mover and the rod string. As far as the gear reducer is concerned, the peak net torques are not allowed to surpass the fixed gearbox rating of 36,155 N, once again. Table 25 shows the resulting peak net torques as well as the gearbox loading for all three cases for both counterweight settings. The exceeding loading factors are indicated in red.

Table 25: Scenario C: Comparison of the Peak Gearbox Torques and Loadings

Case	**MinTorque**		**MinEnergy**	
	Peak Torque	*Gearbox Loading*	*Peak Torque*	*Gearbox Loading*
Constant	51,714 N m	143.03 %	80,366 N m	222.28 %
VarLoad	51,466 N m	142.35 %	68,914 N m	190.61 %
VarEnergy	44,414 N m	122.84 %	69,014 N m	199.88 %

None of the cases can be accomplished with the gear reducer currently in place, since their peak net torques surpass the rating of the gearbox by far. All cases adjusted with the MinTorque counterweight setting require the installation of a 456 D gearbox, with a torque rating of 51,521 N m or, since unavailable at OMV Austria, a 640 D gearbox with a torque rating of 72,310 N m. The MinEnergy scenarios of the two optimized cases require the installation of a 640 D gearbox as well, however the MinEnergy scenario of the Constant case requires even a 912 D gearbox with a torque rating of 103,042 N m or, since unavailable at OMV Austria, a 1280 D gearbox with a torque rating of 144,621 N m.

Also the minimum required motor size is determined once again, by calculating the average mechanical motor power and the cyclic load factor, to check if the installed 40 HP (30 kW) NEMA D motor is large enough. An overview of the calculated values and the required motor sizes is given in Table 26, for all three cases considering both counterweight settings. The exceeding required motor sizes are indicated in red.

Table 26: Scenario C: Comparison of Required Motor Sizes

Case	**MinTorque**			**MinEnergy**		
	P_{Mot}	*CLF*	P_{Req}	P_{Mot}	*CLF*	P_{Req}
Constant	11.77 kW	3.40	40.01 kW	11.77 kW	2.62	30.88 kW
VarLoad	10.06 kW	2.73	27.5 kW	10.06 kW	2.68	26.94 kW
VarEnergy	9.27 kW	3.38	31.35 kW	9.27 kW	3.06	28.37 kW

Regarding the Constant case, the required motor size exceeds the size of the implemented electric motor for both counterweight settings, demanding the installation of a 60 HP (45 kW) motor for the MinTorque scenario and a 50 HP (37 kW) motor for the MinEnergy scenario. The VarLoad case can be performed for both counterweight settings with the current motor, however the VarEnergy case can only be conducted for the MinEnergy setting, since the MinTorque scenario requires the installation of a one size larger motor, 50 HP (37 kW).

Finally, the integrity of the rod string is analysed once more by checking the tensile strength of the polished rod as well as the occurrence of buckling that might lead to breaks or a decrease in fatigue endurance. The biggest rod loads act at the uppermost rod string section, namely the polished rod. With the peak polished rod loads of 64,043 N, 64,777 N and 69,423 N, all three cases stay below the tensile strength of the polished rod that is specified at 114 kN. Buckling does not occur at the Constant case, however for the VarLoad case, buckling can be observed at a true vertical depth (TVD) of 800 m and for the VarEnergy case at a TVD of 800 m and 807 m, each time during the downstroke. Finally, based on the increased deviation between minimum and maximum loads for the optimized cases, it is necessary to determine the fatigue endurance limits as well. They are calculated at the uppermost rod string section below the polished rod and can be determined with the modified Goodman diagram from chapter 2.1.2.1, under consideration of the rod string properties and the forces acting at polished rod. The cross section of the rod string is 387.95 mm², the tensile strength of the rod material 793 N/mm² and the safety factor is assumed to be 0.9. Table 27 shows the minimum and maximum loads acting at the uppermost rod string section for all three cases as well as their corresponding stresses. In addition, the calculated fatigue endurance limits are presented.

Table 27: Scenario C: Comparison of the Fatigue Endurance Limits

	Constant	**VarLoad**	**VarEnergy**
F_{max}	64,043 N	64,777 N	69,423 N
S_{max}	165.08 N/mm²	166.97 N/mm²	178.95 N/mm²
F_{min}	17,486 N	10,288 N	10,462 N
S_{min}	45.07 N/mm²	26.52 N/mm²	26.97 N/mm²
S_a	201.24 N/mm²	191.85 N/mm²	192.08 N/mm²
S_{max}/S_a	81.99 %	87.03 %	93.16 %

With the maximum stresses being clearly below the calculated allowable stresses, the fatigue endurance limit is not reached for any case.

5.4.4 Economic Profitability

The economic feasibility of the optimized cases is checked again by calculating the payout time. The savings in operational expenditures equals the reduction in energy consumption times the averaged electricity price of 0.08 €/kWh and the total increase in capital expenditures amounts to 22,270 €, including purchase and installation costs of the 55 kW VSD as well as replacement costs for the prime mover sheave and counterweights. Without an available EMSR-Installation on site the total increase in capital expenditures rises to 42,270 €. An overview of the yearly energy savings in euros and the resulting payout time in years is given in Table 28 for the frequency-elastic cases considering the MinTorque setting, the MinEnergy setting as well as the regenerative motor configuration.

Table 28: Scenario C: Comparison of the Energy Savings and Payout Time

Case	**MinTorque**		**MinEnergy**		**Energy Recovery**	
	Savings	*Payout*	*Savings*	*Payout*	*Savings*	*Payout*
VarLoad	6,805 €	3.3 (6.2) y	1,584 €	14.1 (26.7) y	1,409 €	15.8 (30.0) y
VarEnergy	6,644 €	3.4 (6.4) y	2,081 €	10.7 (20.3) y	2,060 €	10.8 (20.5) y

5.5 Comparison of the Scenarios

Although the designed pumping system is not entirely suitable for the 10 spm scenario, for instance, the optimized cases of each pumping speed scenario show a similar trend and allow a general prediction of the improvements and deteriorations of frequency-elastic operations compared to constant ones. The first thing that can be noticed is that the influence of the peak polished rod loads on the energy consumption is relatively small. Both VarLoad and VarEnergy cases alter the peak loads only by a small percentage, once a decrease and once an increase, however the resulting reduction in energy usage is comparatively large. This shows that an adequate distribution of the polished rod loads during one cycle is more important than minimized peak loads. The fact that the VarLoad case of the 10 spm scenario even increases the peak load is most likely caused by the more complex prediction of the dynamic forces with the Abaqus simulation, together with the limited speed variation for faster pumping speeds based on the free rod fall velocity. The second trend that can be observed is the shift in required counterbalance torque. In general, higher counterbalance torques are needed to reach MinTorque conditions and lower ones to minimize the energy consumption. For the constant cases these two torques drift far apart, however for the two optimized cases this torque difference is drastically reduced. Especially the VarLoad cases show the closest gap that is even decreasing with lower pumping speeds. Thus, for example, the VarLoad case of the 3.2 spm scenario accomplishes MinTorque and MinEnergy conditions with the same counterbalance torque. This facilitates the pick of the optimum counterweights, since both selection criteria are satisfied with the same or almost the same setting.

As far as the gearbox loading is concerned, different patterns are identified. On the one hand, for the MinTorque installation the gearbox loading is only changed by a small amount, when applying the optimized cases. Some cases lead to a slight increase and others to a slight decrease in gearbox loading, however the selection of the proper gear reducer size is not affected. On the other hand, for the MinEnergy installation a more distinct trend is seen. The gearbox loading is clearly reduced for all optimized cases, especially the VarLoad cases, which might lead to a reduction in required gearbox size. As an example, both optimized cases of the 10 spm scenario reduce the required size from a 1280 D to a 640 D gearbox and consequently the associated investment costs for the pumping unit from 123,363 € to 80,315 €. [54] A similar behavior is observed for the required motor size, where both optimized cases result in a reduction, once more, in particular the VarLoad case. In contrast to the gearbox loading, the reduction is not only seen for the MinEnergy but also for the MinTorque scenario, which again might save some capital investment costs. The 10 spm scenario serves again as example, with the VarLoad case reducing the required motor size from 60 HP to 40 HP and consequently the associated motor costs from 7,495 € to 5,277 €. [55]

The most important outcome of the simulation scenarios is the energy consumption and the electricity costs. Here again, a clear trend is detectable, namely a reduction of these parameters for both optimized cases and all pumping speeds, by a quite similar percentage.

Accordingly, for the VarLoad case the reduction ranges between 34 % and 37 % concerning the MinTorque installation, and between 12 % and 20 % concerning the MinEnergy installation. In addition, for the VarEnergy case the reduction ranges between 30 % and 33% concerning the MinTorque installation and between 16 % and 21 % concerning the MinEnergy installation. This means that the potential of energy savings is nearly the same for both the VarLoad and VarEnergy case, with the first one showing slightly larger savings for MinTorque counterweight settings and the second one for MinEnergy counterweight settings. This observation means that the operational expenditures can be significantly reduced and consequently the system efficiency increased, by the usage of frequency-elastic operations, regardless of the average pumping speed or the counterweights adjustment.

Possible weaknesses of the optimization principle expose when carrying out the analysis of the contact forces between the rod and tubing string. Although it is proved that the slower speed scenarios, namely the one with 3.2 spm and 5 spm, have no problems with the occurrence of buckling, the 10 spm scenario demonstrates that the likelihood of this unwanted effect during the downstroke is increased when applying the variable speed cases. This requires a case-by-case feasibility study, in terms of buckling prediction, and if necessary the installation of additional sinker bars at the bottom of the rod string, in particular for faster pumping speeds.

In the light of all the relevant circumstances, it can be said that the VarLoad case shows the best performance and is technical feasible without further ado, for low and intermediate pumping speeds. To sum up the benefits, the following outcome can be achieved with this operating mode: The peak polished rod loads are decreased by an average of 2 %. The average reduction of counterbalance torque difference between the MinTorque and the MinEnergy scenario is 98 %, meaning that both conditions are fulfilled with almost the same counterweight setting. For the MinEnergy installation, the gearbox loading is reduced by an average of 22 % and the required motor size by 13 %. The mean reduction of the energy consumption and electricity costs is 36 % for the MinTorque setting, 18 % for the MinEnergy setting and 30 % for a regenerative motor configuration. The occurrence of buckling is not expected and the fatigue endurance limit is not reached.

6 Start-up Scenarios

6.1 Sand Production

In the petroleum industry, sand production describes the phenomenon of solid particles being produced together with reservoir fluids and poses one of the biggest challenges to a production engineer during the lifecycle of a well. In general the occurrence of sand production depends on the following components: The strength and geomechanical properties of the reservoir rock, regional stresses as well as local loads imposed on the wellbore caused by the fluid flow, a reduced pore pressure or the presence of water. Since estimates show that more than 70 % of the world's oil and gas reserves are located in poorly consolidated reservoirs, the possibility of sand production needs to be considered for almost every well and taken into consideration for the production and completion design. Otherwise several complications or additional costs might arise and face the responsible production engineers: [56, pp. 1-2] [57, p. 227] [58, p. 65]

- Formation damage or collapse by the flowing sand grains
- Wellbore instability or casing collapse
- Failure of both downhole and surface equipment
- Lost production and work over costs due to shut-in and equipment replacement
- Costs of separating sand from the produced fluids
- Environmental concerns and additional expenses due to sand disposal

6.1.1 Preventing Sand Production

Basically there are two approaches to prevent or control the impact of sand production. The first one is by predicting the occurrence of sand production as a function of bottomhole flowing pressure and adapting the production operation and the second one is by optimizing the completion design and using downhole equipment specifically dedicated for this purpose.

The foundation of the sand production prediction is a geomechanical model of the reservoir formation that includes the determination of the rock strength with UCS (unconfined compressive strength) or TWC (thick wall cylinder) measurements of core plugs and the characterization of regional and effective stresses with density logs, leak-off tests as well as an estimation of the pore pressure. This information allows for the calculation of the critical bottomhole flowing pressure as a function of yield strength, effective tangential stress and pore pressure, which should not be undercut to avoid a destabilization of the formation and the resulting mobilization of sand grain particles. As a consequence the allowable pressure drawdown can be predicted, in order to make a decision about the downhole pump design as well as the maximum flowrate and pumping speed.

As far as the completion design is concerned, there are three common practices applied in terms of sand control. On the one hand, special perforation techniques are used, such as oriented perforating where the wellbore is only perforated in one direction, namely along the maximum stress, which delays or even avoid the occurrence of sand production. On the other hand, downhole equipment can be installed, such as gravel packs that consist of sand screens filled up with gravel, five to seven times the size of the median sand particles, stabilizing the formation and preventing solids from entering the wellbore, or downhole pumps with a farr plunger that has a unique design allowing for the production of certain amounts of sand particles without the plunger getting stuck in the pump barrel. [59, pp. 129-147, 149, 180-183] [60]

6.1.2 Sand Production during Start-ups

The most critical phase of the lifecycle of a well in terms of sand production is the start-up, at the beginning of operations or after a well intervention. Even if the production system is designed below the allowable pumping speed and flow rate, defined by the critical bottomhole pressure and drawdown, immediate sand production might occur and force the downhole equipment to fail after a couple of days. The reason for this is that abrupt changes in flow rate lead to oscillations of the bottomhole hole flowing pressure and disturbed near-wellbore formation stresses that might initiate rock material failure and as a consequence sand production. Another important aspect is the high water cut after workover operations in the near-wellbore formation. Despite using bridging material during well interventions, it is still possible that a certain amount of workover fluid is lost through the perforations and disperses in the near-wellbore region. The resulting higher water cut has several impacts on the stability of the formation and the mobilization of sand particles. First of all a high water cut causes a chemical interaction between the rock matrix and the water, and depending on the mineralogy, especially the cement mineralogy, this weakens the overall strength of the rock material. Furthermore, an increase in water saturation reduces the capillary bonding effect between the originally water-wet sand grains and increases drag forces induced by the relative permeability effect. In general, failed and disaggregated sand is held together by capillary cohesion forces but with an increase in water cut these forces are extinguished and the failed sand grains will get mobilized much easier. [56, pp. 1-2] [57, p. 228] [61, p. 2]

Nowadays, it is common practice at OMV, to put sand sensitive wellbores back on operation by using the three frequency steps that can be installed at the electric prime mover, starting with the lowest frequency and ending with the highest frequency, resulting in the designed production rate. The motor adjustments are carried out manually and the length and timing of each frequency step is chosen based on long-time experience of the responsible engineers. This work will give an additional approach to design the start-up of a sand sensitive well by installing a continuous start-up ramp with a VSD controller, based on the operation and fluid data of a sample well.

6.2 Start-up Ramp with the Usage of a VSD

For the design of an illustrative start-up ramp, the data of another sample well, called Well 2, is provided by OMV Austria GmbH, which is located near Gaenserndorf and produces from a sand sensitive horizon. The well is equipped with a LUF 640 pumping unit, a tapered rod string with a 1 in and a 7/8 in section, as well as a 25-175 RHAC-21-4 subsurface pump, set in a 2 7/8 in tubing at a measured depth of 1239 m. With a water cut of 87.65 % the operation is designed with a pumping speed of 4.59 spm to prevent the occurrence of sand production and together with an effective stroke length of 4.13 m as well as a pump efficiency of 87 %, the well has an average production rate of 36.85 m³ per day. After a well intervention in February, 2016, where 17 m³ of workover fluid were lost into the formation, the well was put back into operation by using increasing frequency steps of the 60 HP (45 kW) electric motor to avoid the start-up effects described in chapter 6.1.2. The start-up lasted until the 8th of March and was a success since the well has not failed so far and is still in operation (July, 2016). A drawing of the well schematic of Well 2 can be seen in Appendix I. [30]

6.2.1 Operation and Fluid Data of the Sample Well

To understand the start-up behaviour of the sample well the following data can be obtained from the internal well database of OMV Austria GmbH: The pumping speed, the effective motor frequency, the daily production as well as the water cut. All parameters are measured at the production site in suitable time intervals and are summarized in two tables shown in Appendix J. In addition, the values of the water cut are illustrated in Figure 68 on a time scale showing the first 50 days since operation start. [30]

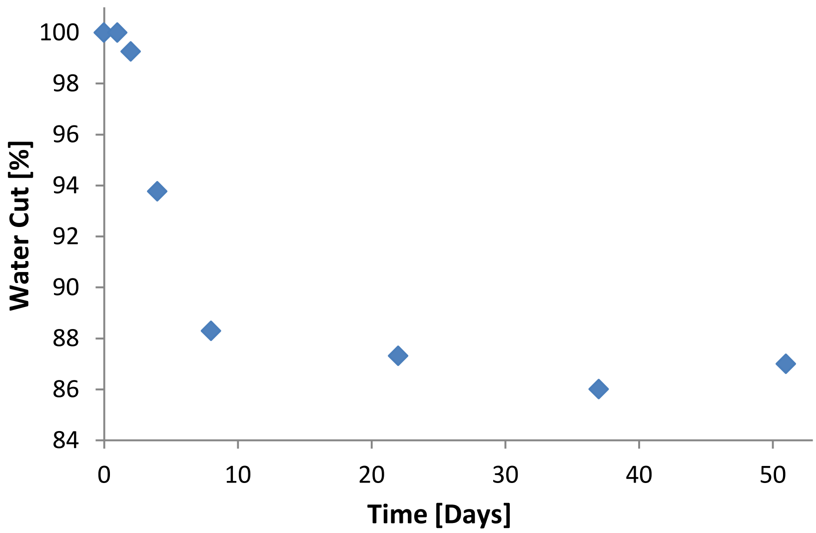

Figure 68: Water Cut as a Function of Operating Days

The graph shows that the water cut reaches a value of almost 100 % in the first two days. The reason for this phenomenon is that after the well intervention, the wellbore is entirely filled with the workover fluid that is produced in the first period of the start-up. From day two to 22 a continuously decreasing water cut can be observed that is, however, still higher than the actual water cut of the formation fluid. This is caused by the amount of workover fluid that is still present in the wellbore and the mixing of the formation fluids with the lost workover fluids in the near-wellbore region of the reservoir. After 22 days of production the workover fluid is pumped out again and the water cut has stabilized to its actual value of 87.65 %, besides small variation.

6.2.2 Design of the Start-up Ramp

Based on this data, an additional approach for the start-up can be designed, in case the well is equipped with a VSD unit. The basic concept of the start-up ramp is to start the operation at the minimum allowable pumping speed and keep this value constant until the system reaches its dynamic operational conditions and the workover fluid in the wellbore is pumped out again. Afterwards the velocity is linearly increased day by day, to reach the designed pumping speed of 4.59 spm when the remaining and lost workover fluid is pumped out and the water cut falls back to its original value of 87.65 %. Subsequently, the start-up period ends and the system is operated constantly at 4.59 spm as specified in the design sheet. In addition to the calculation sequence described in this chapter, an extract of the used Excel sheet can be seen in Appendix K.

For the first period the pumping speed is set to a value of 2.5 spm, based on the limitations of the pumping unit as already discussed in chapter 4.5.1.2, which results in a production rate of 20.07 m³/day. The volume that needs to be pumped to reach dynamic conditions equals the annulus area between casing and tubing times the depth of the dynamic fluid level. With an inner casing diameter of 161.7 mm, an outer tubing diameter of 88.9 mm and a fluid level of 652 m, the volume reaches a value of 9.34 m³. Furthermore, the volume that needs to be pumped to clean the entire wellbore from the workover fluid equals the volume of the casing annulus as well as the volume between tubing and rod string. With a casing length of 1470 m, a tubing length of 1239 m, a 1 in rod string length of 484 m as well as a 7/8 in rod string length of 777 m, the volume reaches a value of 27.6 m³. The time needed to fulfil both conditions with a constant pumping speed of 2.5 spm is 33 hours and by rounding up to full days the first period of the start-up is designed to last two days.

For the second period, the task is to determine the optimum number of days as well as the pumping speed increase per day to reach the formation water cut at the end of the ramp. Therefore it is necessary to calculate the cumulative volume pumped, from the original start-up scenario, until the actual water cut has established. This can be done by looking at the time history of the water cut and the monthly production data shown in Table 29.

Table 29: Monthly and Cumulative Production [30]

Month	Monthly Production [m³]	Cumulative Production [m³]
February, 2016	385.1	385.1
March, 2016	1060.0	1445.1
April, 2016	1130.2	2575.3
May, 2016	1157.5	3732.8

With the original water cut being established on March 8, the volume pumped is determined by subtracting 23 times the average production rate of 36.85 m³/day from 14451.1 m³, the cumulative production at the end of March. This results in a volume of 597.55 m³ and by subtracting 40.15 m³, the volume that is already pumped in the first period, 557.41 m³ of fluids needs to be produced during the ramp phase of the start-up. For a linearly increasing pumping speed from 2.5 spm to 4.59 spm, it will take 19.58 days or, rounded up, 20 days to produce this amount of liquid, which leads to a pumping speed increase of 0.1 spm/day. The resulting start-up ramp, shown with the pumping speed as a function of operating days, is illustrated in Figure 69.

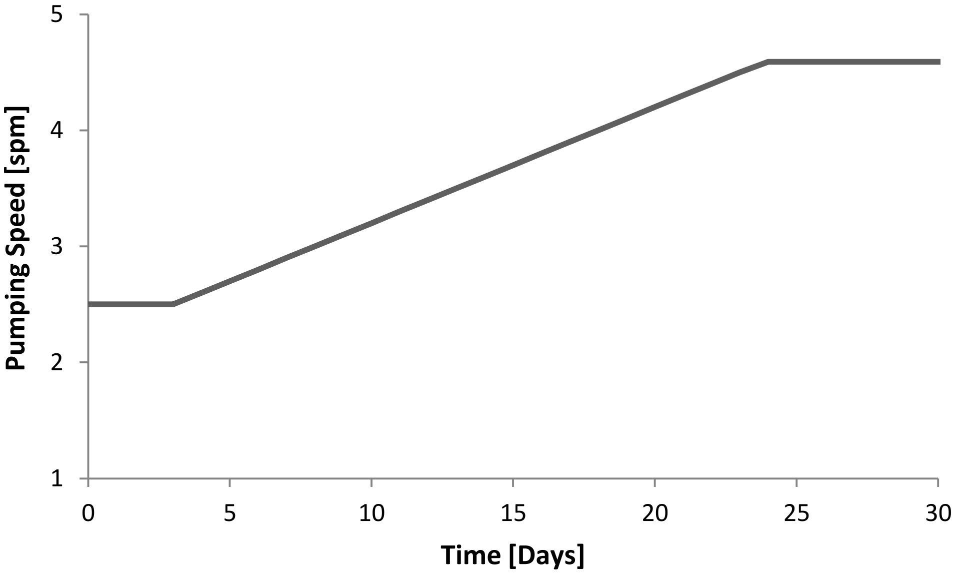

Figure 69: Start-up Ramp: Pumping Speed as a Function of Operating Days

The overall duration of the designed start-up is 22 days and equals therefore the length of the original procedure. The major advantages of implementing a VSD-driven start-up ramp for putting a well back on operation is that the jumps in flow rate and consequently in bottomhole flowing pressure are reduced to a minimum: On the one hand by operating the well constantly at the minimum allowable pumping speed during the most critical phase of the start-up and on the other hand by linearly increasing the pumping speed in small steps day by day, with a decreasing water cut. This reduces the risks of immediate rock failure and as a result the abrupt breakdown of downhole equipment caused by moving sand particles. In addition, the start-up ramp can be preinstalled on the VSD controller, which eliminates the need of manually frequency adjustments of the electric prime mover on-site. The start-up ramp has to be calculated for each future well individually and can be adjusted and fasten up by performing frequent water cut analysis.

7 Conclusion and Recommendations

In conclusion, it can be said that this thesis proves that the performance of a SRP can be considerably improved when the system is equipped with a VSD and operated frequency-elastic. It is shown that the energy efficiency of the pump and consequently the amount of operational expenditures can be significantly reduced by altering the pumping speed within each stroke.

To determine the optimum function of the drive speed and to point out the potential for efficiency enhancement, an integrated model is built that describes in detail the whole working process of a sucker rod pumping system. The first part of the presented method is the prediction of the motion and forces of the sucker rod string with a one-dimensional damped wave equation and Hooke's law. This approach calculates the shift in rod displacement and weight along several points from the bottom to the top of the string under consideration of the elastic behaviour and linear mass of the rod material. The damped wave equation requires the input of two boundary conditions: On the one hand, the plunger load at the bottom of the rod string, which depends mainly on the hydrostatic net pressure of the liquid column in the tubing and on the other hand, the motion of the polished rod that can be determined with an updated version of Svinos' exact kinematic analysis of the pumping unit by calculating the position, velocity and acceleration at each link from the rotating crankshaft to the reciprocating polished rod. The main outcome of the damped wave equation is the distribution of the polished rod loads during one stroke cycle that are then used, together with the counterbalance effect of crank arms and counterweights as well as inertial torques of the pumping unit's components, to determine the torque and power requirements at the gearbox. Subsequently, the electrical power input and energy consumption of the prime mover is predicted by taking additionally the power losses into account, which occur in the gearbox, the V-belt drive, the pumping unit and the electric motor.

At this point, the stated model is applied by using the data of a sample well that is operated conventionally with a constant drive speed. The resulting distributions of the polished rod loads and the energy consumption are then analysed in detail to find a crankshaft velocity profile for an optimized operation of the SRP. The chosen profile is described with two harmonic cosine functions, one for the up- and one for the downstroke. It is designed to have the same velocities in the turning points and to have the same average pumping speed as the conventional operation. These functions can be then adjusted automatically to minimize once the peak polished rod load and once the energy consumption by changing the time ratio of the upstroke as well as the maximum downstroke velocity within the scope of the limitations imposed by the pumping unit, the gearbox and the drive units.

This optimization principle is then adopted, together with a more exact prediction of the polished rod loads, for three different pumping speeds that represent the theoretical operating range of the pumping unit. For each scenario, two optimized and the conventional operation are simulated and compared among one another in consideration of the MinTorque and MinEnergy counterweight setting as well as a regenerative motor configuration. In addition, each simulation case is analysed on technical feasibility for the current well installation and economic profitability based on the increase in capital expenditures of frequency-elastic operations. All speed scenarios show a similar trend in potential for improvement, with the best case of the 5 spm scenario resulting in the following outcomes:

The peak polished rod loads are decreased by 2 % and the difference in required counterbalance torque between the MinTorque and MinEnergy setting by 96 %. For the MinTorque setting, the peak power is increased by 18 % and the gearbox loading by 12 %, yet the energy consumption and electricity costs are reduced by 37 %. This raises the total system efficiency from 23 % to 36 %. For the MinEnergy setting, the peak power is decreased by 19 %, the gearbox loading by 23 % and the energy consumption and electricity costs by 17 %. This raises the total system efficiency from 30 % to 36 %. In case the electric motor allows for the regeneration of energy, the energy consumption and electricity costs can be decreased by 30 %, which raises the total system efficiency from 32 % to 46 %.

Although it is shown that frequency-elastic operations substantially reduce the energy consumption without exceeding the technical limits of the system's components, the economic viability of these operations depends mainly on the implementation practices of a VSD system on the well site and varies widely from operator to operator. Moreover, the electricity costs and consequently the amount of savings influence strongly the profitability, which depends again on the operator and the available power grid. Nevertheless, further research and investigation of frequency-elastic operations should be conducted, since the framework conditions might change in the future and since it is certainly possible to reduce the associated implementation costs. Apart from that, many SRP driven wells are already equipped with VSDs due to complex reservoir and inflow characteristics, which would minimize the increase in capital expenditures to almost zero. Finally, this thesis also shows that the purchase and installation of a VSD can be used to optimise and automate the start-up of a SRP by preinstalling a start-up ramp and linearly increasing the pumping speed in small steps day-by-day. This eliminates the need of manually frequency adjustments on the well site and reduces the risk of abrupt failure of the downhole equipment caused by sand production.

As a next step, it is recommended to verify the results of this thesis by performing experimental studies in the field. It will be necessary to analyse in particular the efficiency changes in the surface equipment of the SRP system, since they are mostly estimated with empirical values in this thesis and assumed to be constant. Especially the impact on the efficiencies of the electric motor and the V-belt drive should be investigated in detail when applying frequency-elastic operations, to be able to update the presented model and give a more accurate prediction of the improvement potential as well as the reduction in energy consumption and operational expenditures.

8 References

[1] N. J. Mitra and A. Kumar, Principles of Artificial Lift, Allied Publishers Pvt. Ltd, 2012.

[2] J. F. Lea and H. V. Nickens, “Selection of Artificial Lift (SPE 52157),” in *SPE Mid-Continent Operations Symposium*, Oklahoma City, Oklahoma, 1999.

[3] G. Takacs, Sucker-Rod Pumping Handbook - Production Engineering Fundamentals and Long-Stroke Rod Pumping, Waltham, Massachusetts : Elsevier Inc., 2015.

[4] R. v. Flatern, “Rod Pump Systems,” 2016. [Online]. Available: http://www.slb.com/~/media/Files/resources/oilfield_review/defining_series/Defining-Rod-Pumps.ashx. [Accessed 7 December 2016].

[5] Human Development Ltd., “Describe and Monitor Pumpjack and Prime Mover,” June 2008. [Online]. Available: http://docplayer.net/15000891-Describe-and-operate-beam-pump.html. [Accessed 7 December 2016].

[6] “PetroWiki,” Society of Petroleum Engineers, [Online]. Available: http://petrowiki.org/Prime_mover_for_sucker-rod_pumping_unit. [Accessed 21 December 2016].

[7] Lufkin Oilfield Products Group, *General Catalog 2008/2009,* Houston, Texas, 2007.

[8] J. D. Clegg, “Production Operations Engineering,” in *Petroleum Engineering Handbook*, Richardson, Texas, Society of Petroleum Engineers, 2007.

[9] “Sucker-Rod,” [Online]. Available: http://www.sucker-rod.com/img/sucker-rod.jpg. [Accessed 14 December 2016].

[10] API, “API Specification for Sucker Rods,” in *API Spec. 11B, 26th Edition*, 1998.

[11] G. Takacs, “Subsurface Pumps,” IEEE GlobalSpec, [Online]. Available: http://www.globalspec.com/reference/78795/203279/subsurface-pumps. [Accessed 10 December 2016].

[12] “Artificial Lift - Sucker Rod Pumps,” [Online]. Available: http://infohost.nmt.edu/~petro/faculty/Kelly/sec4.pdf. [Accessed 10 December 2016].

[13] API, “API Specification for Subsurface Sucker Rod Pumps and Fittings,” in *API Spec. 11AX, 12th Edition*, 2012.

[14] B. Welk, Interviewee, *Purchase Price and Installation Costs of VSDs at OMV Austria GmbH.* [Interview]. January 2017.

[15] “Wikipedia,” [Online]. Available: https://en.wikipedia.org/wiki/Induction_motor. [Accessed 12 December 2016].

[16] D. Manney, “Watts New - The official blog for L&S Electric,” 22 March 2013. [Online]. Available: http://www.lselectric.com/4-quadrant-motor-control-2-quadrant-operation/. [Accessed 8 February 2017].

[17] R. Okrasa, Adjustable Speed Drive - Reference Guide, Canada: Ontario Hydro, 1997.

[18] “VFD Fundamentals,” Kilowatt Classroom , 2003. [Online]. Available: http://controltrends.org/wp-content/uploads/2010/10/VFFundamentals.pdf. [Accessed 12 December 2016].

[19] “Electrical Engineering Stack Exchange,” [Online]. Available: http://electronics.stackexchange.com/questions/163239/running-ac-synchronous-motor-with-dc. [Accessed 12 December 2016].

[20] “PetroWiki,” Society of Petroleum Engineers, [Online]. Available: http://petrowiki.org/Alternating_current_motor_drives. [Accessed 13 December 2016].

[21] Schneider Electric, “Schneider Electric Product Catalog - MX eco,” [Online]. Available: http://www.schneider-electric.at/de/product-range/2521-mx-eco/?parent-category-id=2900. [Accessed 10 February 2017].

[22] TMEIC Corporation, “Drive Solutions for the Oil and Gas Industry,” 2011. [Online]. Available: https://www.tmeic.com/Repository/Others/Oil-Gas%20Brochure%20rev-address-lo-res.pdf. [Accessed 13 December 2016].

[23] G. Sam, M. Kaestenbauer, C. Burgstaller and E. Chevelcha, “Fully Automated Fluid Level Measurement Tool (SPE 145434),” in *SPE Asia Pacific Oil and Gas Conference and Exhibition* , Jakarta, Indonesia, 2011.

[24] C. Li, Z. Liu, Z. Yang and Y. Wang, “The Application of One VSD Driving Multi-ESPs Technology in Offshore Heavy Oil Field (SPE 64619),” in *SPE International Oil and Gas Conference and Exhibition*, Bejing, China, 2000.

[25] C. Guffey, J. Rogers and L. Hester, “Field Testing of Variable-Speed Beam-Pump Computer Control (SPE 20123),” *SPE Production Engineering,* pp. 155-160, May 1991.

[26] Unico Inc., “LRP - Linear Rod Pump,” [Online]. Available: http://regalaustralia.com.au/mktg/marketing/pdfs/LRP_flyer.pdf. [Accessed 13 December 2016].

[27] R. Peterson, T. Smigura, C. Brunings, W. Quijada and A. Gomez, “Production Increases at PDVSA Using an Improved SRP Control (SPE 103157),” in *SPE Annual Technical Conference and Exhibition* , San Antonio, Texas, 2006.

[28] K. Palka and A. Czyz, “Optimizing Downhole Fluid Production of Sucker Rod Pumps Using Variable Motor Speed (SPE 113186),” in *SPE Western Regional and Pacific Section AAPG Joint Meeting* , Bakersfield, California, 2008.

[29] Schlumberger, “UniStar - Downhole Protection VSD System,” [Online]. Available: slb.com/rodlift. [Accessed 12 December 2016].

[30] OMV Austria GmbH, *GDB - Internal Well Database,* Gaenserndorf, May, 2016.

[31] J. G. Svinos, “Exact Kinematic Analysis of Pumping Units (SPE 12201),” in *58th Annual Technical Conference and Exhibition*, San Francisco, California, 1983.

[32] API, “API Specification for Pumping Units,” in *API Spec. 11E, 19th Edition*, 2013.

[33] S. G. Gibbs, “Predicting the Behavior of Sucker-Rod Pumping Systems (SPE 588),” *Journal of Petroleum Technology,* pp. 769-778, 1963.

[34] S. G. Gibbs, “The Wave Equation as Applied to Rod Pumping,” in *Rod Pumping - Modern Methods of Design, Diagnosis and Surveillance*, BookMasters Inc., 2012, pp. 33-58.

[35] T. A. Everitt and J. W. Jennings, “An Improved Finite-Difference Calculation of Downhole Dynamometer Cards for Sucker-Rod Pumps (SPE 18189),” *SPE Production Engineering,* pp. 121-127, February 1992.

[36] H. P. Krenn, Technisches Handbuch für Sondenbehandlung/Workover, Gaenserndorf: OMV Austria GmbH.

[37] S. G. Gibbs, “Method of Determining Sucker Rod Pump Performance”. USA Patent 3,343,409, 26 September 1967.

[38] C. Langbauer, Sucker Rod Anti - Buckling System Analysis, Leoben: Montanuniversitaet Leoben, 2015.

[39] G. Takacs, L. Kis and A. Koncz, “The calculation of Gearbox Torque Components on Sucker-Rod Pumping Units Using Dynamometer Card Data,” *J Petrol Explor Prod*

Technol, pp. 101-110, 2016.

[40] G. Takacs and G. Ladanyi, “Calculation of Gearbox Torques Considering Inertial Effects,” *Geosciences and Engineering Vol 1,* pp. pp. 283-291, 2012.

[41] “Steel W-Shape Section Data,” [Online]. Available: http://engr.bd.psu.edu/rxm61/MET210/CourseSupplements/Steel%20W-Shape%20Section%20Data.pdf. [Accessed 23 November 2016].

[42] F. W. Gipson and H. W. Swaim, “The beam pumping design chain,” in *Proc 31st Annual Southwestern petroleum short course*, Lubbock, Texas, 1985.

[43] Theta Oilfield Services Inc., *RODSTAR-D/V Modern Design and Simulation of Rod Pumping Systems for Deviated or Vertical Wells,* La Habra, California, 2011.

[44] Eurostat, “Electricity Prices for Industrial Consumers,” Eurostat, 2016. [Online]. Available: http://appsso.eurostat.ec.europa.eu/nui/show.do?dataset=nrg_pc_205&lang=en. [Accessed 23 November 2016].

[45] J. P. Byrd, “High Volume Pumping with Sucker Rods (SPE 2104),” in *SPE Eight Secondary Recovery Symposium*, Wichita Falls, Texas, 1968.

[46] S. Tredinnick, “Variable Speed Pumping: How Low Can I Go,” *District Energy,* pp. 50-51, Third Quarter 2006.

[47] S. Waner and S. R. Costenoble, Applied Calculus, Sixth Edition, Boston, Massachusetts: Brooks/Cole, Cengage Learning, 2014.

[48] Excel Support, “Define and solve a problem by using Solver,” Microsoft Excel, [Online]. Available: https://support.office.com/en-US/article/Define-and-solve-a-problem-by-using-Solver-9ed03c9f-7caf-4d99-bb6d-078f96d1652c. [Accessed 30 November 2016].

[49] GoHz Inc., “GoHz.com,” 25 June 2015. [Online]. Available: http://www.gohz.com/what-is-regenerative-braking-in-vfd. [Accessed 24 January 2017].

[50] Lufkin Automation, “Pumps and Service,” 2011. [Online]. Available: http://pumpsandservice.com/userfiles/files/REGEN.pdf. [Accessed 24 January 2017].

[51] H. Wittel, D. Muhs, D. Jannasch and J. Voßiek, Roloff/Matek Maschinenelemente - Normung Berechnung Gestaltung, Wiesbaden: Springer Vieweg, 2013.

[52] A. C. Ugural, Mechanical Design of Machine Components, Boca Raton, Florida : CRC Press Taylor and Francis Group, 2015.

[53] Klein, Einführung in die DIN-Normen, Berlin: DIN Deutsches Institut für Normung e.V., 2008.

[54] G. Schreiber, Interviewee, *Pumping Unit Costs and V-Belt Installations at OMV Austria GmbH.* [Interview]. January 2017.

[55] WEG, "Electric Motors Catalog," [Online]. Available: http://ecatalog.weg.net/redirect/index.asp?p_Categoria=42&p_Produto=431&p_Table=YES. [Accessed 15 January 2017].

[56] B. Wu and C. P. Tan, "Effect of Water-Cut on Sand Production (SPE 92715)," in *Asia Pacific Oi l& Gas Conference and Exhibition* , Jakarta, Indonesia , 2005.

[57] A. Nouri, H. Vaziri, H. Belhaj and R. Islam, "Sand-Production Prediction: A New Set of Criteria for Modeling Based on Large-Scale Transient Experiments and Numerical Investigation (SPE 90273)," *SPE Journal,* pp. 227-237, June 2006.

[58] B. Ikporo and O. Sylvester, "Effect of Sand Invasion on Oil Well Production: A Case Study of Garon Field in the Niger Delta," *The International Journal of Engineering and Science,* pp. 64-72, 2015.

[59] J. Bellarby, Well Completion Design, Amsterdam, The Netherlands: Elsevier, 2009.

[60] Muth Pump LLC, "Farr Plunger," Muth Pump, [Online]. Available: http://www.muthpump.com/farr-plunger/. [Accessed 5 January 2017].

[61] M. Schietz, Optimization of Well Start-Up, Leoben: Montanuniversitaet Leoben, 2009.

9 Nomenclature

Symbol	Definition	Unit
A	Distance between the saddle bearing and horsehead	m
a	Amplitude of the angular crankshaft speed function	rad/s
A_B	Cross section of the V-belt	m^2
A_{rod}	Cross section of the rod string	m^2
A_{pl}	Cross section of the plunger	m^2
AR	Polished rod acceleration	m/s^2
BV	V-belt velocity	m/s
C	Distance between the equalizer and saddle bearing	m
c	Damping coefficient	1/s
CLF	Cyclic load factor	-
d	Vertical shift of the angular crankshaft speed function	rad/s
d_{DS}	Vertical shift of the angular speed function during the downstroke	rad/s
d_{GB}	Diameter of the gearbox sheave	mm
d_{PM}	Diameter of the prime mover sheave	mm
E	Young's modulus of steel	N/m^2
e	Distance between the prime mover and gearbox sheave	m
E_B	Elastic modulus of the V-belt material	N/m^2
E_{cons}	Energy consumption	J, kWh/h
E_{hydr}	Hydraulic energy used for lifting	kWh/h
F	Rod Load	N
F_{max}	Maximum Rod Load	N
F_{min}	Minimum Rod Load	N
f	Frequency of the AC power	Hz
F'_1	Tight side tension force of the V-belt	N
F_{b1}	Bending force in the V-belt around the prime mover sheave	N
F_c	Centrifugal force of the V-belt	N
F_d	Damping force	N
F_x, $F_{x+\Delta x}$	Tension forces of one rod element	N
G	Height of the gearbox	m
g	Gravitational constant	m/s^2
H	Height of the saddle bearing	m
I	Horizontal distance between the gearbox and saddle bearing	m
I_{rot}	Mass moment of inertia of the rotating components	kg m^2
I_{SB}	Mass moment of inertia of the oscillating components	kg m^2
K	Distance between the gearbox and saddle bearing	m
L	Distance between the wrist pin and saddle bearing	m
L_{dyn}	Dynamic fluid level from the surface	m
L_{rod}	Length of the rod string	m

m	Mass of one rod element	kg
m^*	Linear mass density of the rod string	kg/m
N	Instantaneous pumping speed	spm
N_{avg}	Average pumping speed	spm
N_{crit}	Critical pumping speed	spm
N_{mot}	Instantaneous motor speed	rpm
N_{syn}	Synchronous motor speed	rpm
P	Length of the pitmans	m
p	Number of poles	-
P_e	Electrical power input	W, kW
P_{max}	Peak electrical power	W, kW
P_{mot}	Average mechanical motor power	kW
P_{req}	Required motor size	kW
PL	Plunger load	N
PL_{DS}	Plunger load during the downstroke	N
PL_{US}	Plunger load during the upstroke	N
PR	Polished rod position	-
PRL	Polished rod load	N
p_{tb}	Tubing pressure at the wellhead	Pa
Q_{tot}	Total production rate	m^3/day
R	Distance between the gearbox and wrist pin bearing	m
R_{US}	Ratio of the upstroke	-, %
S	Stroke length	m
S_{max}	Maximum Rod Stress	N/mm^2
S_{min}	Minimum Rod Stress	N/mm^2
s	Motor slip	-, %
S_{eff}	Effective stroke length	m
S_x, $S_{x+\Delta x}$	Mechanical stresses of one rod element	N/m^2
SU	Structural unbalance	N
T	Time span of one stroke	s
t	Time	s
t_0	Phase shift of the angular crankshaft speed function	s
T_a	Tensile strength of the rod material	N/mm^2
t_B	Effective belt thickness	mm
T_{CB}	Counterbalance torque	N m
T_{CBmax}	Maximum counterbalance torque	N m
T_{DS}	Time span of the downstroke	s
T_{ia}	Articulating inertial torque	N m
T_{ir}	Rotary inertial torque	N m
T_{mot}	Motor torque	N m
T_{net}	Net torque	N m
T_{rod}	Rod torque	N m

T_{US}	Time span of the upstroke	s
TF	Torque factor	m
t_t	Transition time of the plunger load	s
u	Rod displacement	m
v_s	Speed of sound through the rod material	m/s
VR	Polished rod velocity	m/s
W	Weight of the rod string	N
x	Distance from the surface	m
Z	Speed reduction ratio of the gearbox	-
α	Crank angle between the 12 o'clock and bottom stroke position	rad
β_1	Contact angle between the prime mover sheave and the V-belt	rad
γ	Crank angle between the reference line and bottom stroke position	rad
Δt	Time step	s
Δx	Length of one rod element	m
η_{mech}	Surface mechanical efficiency	-, %
η_{mot}	Motor efficiency	-, %
η_{pump}	Pump efficiency	-, %
η_{surf}	Total efficiency of the surface equipment	-, %
θ	Crank angle from the 12 o'clock position	rad
θ_2	Crank angle from the bottom of the stroke position	rad
θ_3	Angle of the pitman from the reference line	rad
θ_4	Angle of the walking beam from the reference line	rad
$\dot{\theta}_2$	Angular crankshaft velocity	rad/s
$\dot{\theta}_3$	Angular pitman velocity	rad/s
$\dot{\theta}_4$	Angular walking beam velocity	rad/s
$\dot{\theta}_{maxDS}$	Maximum angular crankshaft velocity during the downstroke	rad/s
$\dot{\theta}_{TP}$	Angular crankshaft velocity in the turning points of the stroke	rad/s
$\ddot{\theta}_2$	Angular crankshaft acceleration	rad/s^2
$\ddot{\theta}_3$	Angular pitman acceleration	rad/s^2
$\ddot{\theta}_4$	Angular walking beam acceleration	rad/s^2
μ	Dimensionless friction factor of the V-belt	-
μ'	Theoretical friction factor of the V-belt	-
ν	Dimensionless damping factor	-
ρ_B	Density of the V-belt material	kg/m^3
ρ_{mix}	Density of the fluid mixture	kg/m^3
ρ_{st}	Density of steel	kg/m^3
σ_{max}	Maximum stress in the V-belt	N/m^2
φ	Groove angle of the sheaves	rad
ψ	Angle of the walking beam from the reference line	rad
ψ_B	Angle of the walking beam at the bottom of the stroke	rad
ψ_T	Angle of the walking beam at the top of the stroke	rad

Appendices

Appendix A

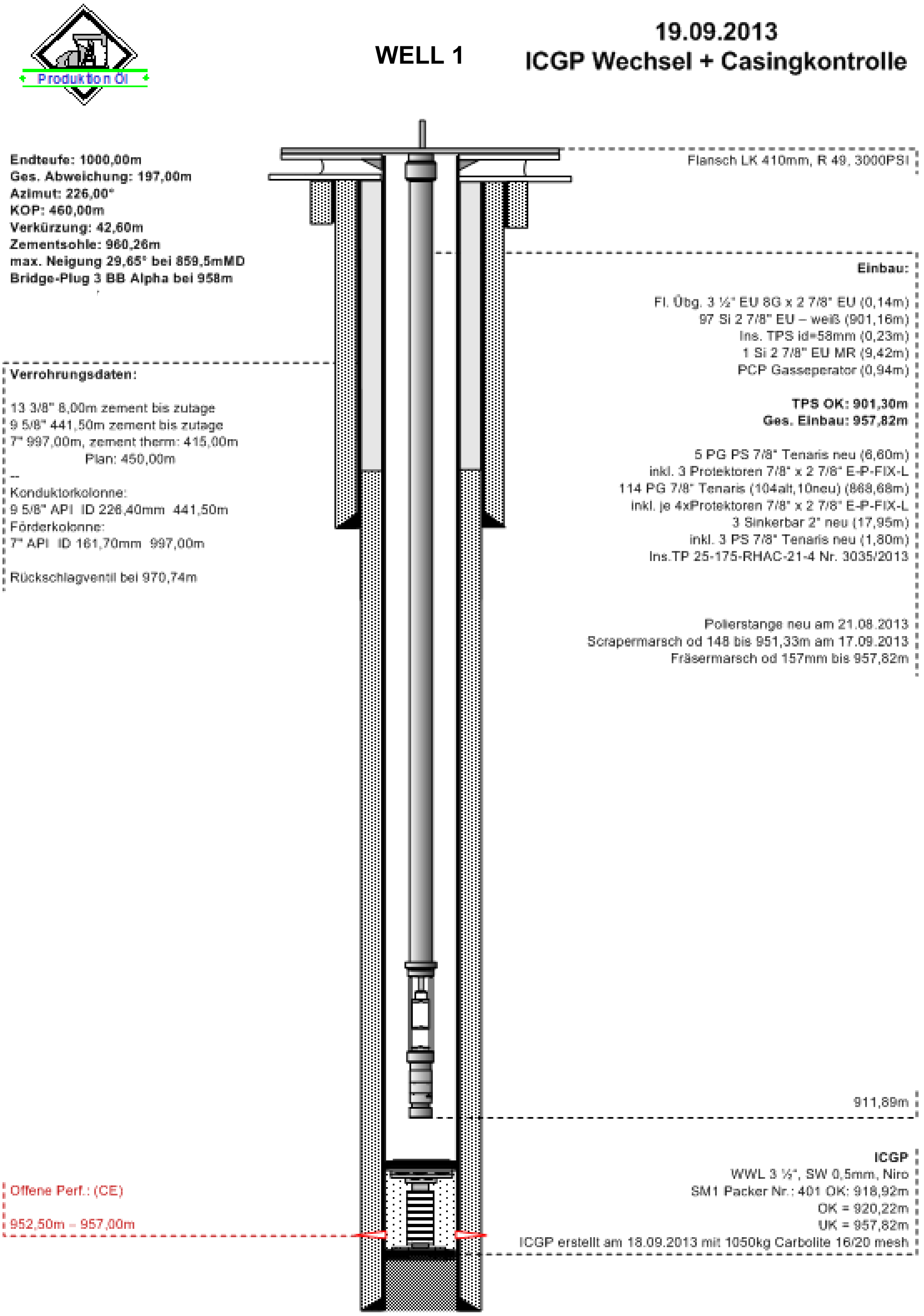

Figure 70: Wellbore Schematic of Well 1

Appendix B

```
%CALCULATION OF THE POLISHED ROD LOADS IN MATLAB

function u=polished_rod_loads

    %Rod Material Definition
    E=2.06E11;                        %Elastic modulus [N/m²]
    rho_st=7850;                      %Steel density [kg/m³]

    %Downhole Equipment Definition
    L=900;                            %Rod string length [m]
    dr=7/8*25.4/1000;                 %Rod diameter [m]
    wr=3.56;                          %Linear mass density [kg/m]
    dp=1.75*25.4/1000;                %Plunger Diameter [m]

    %Fluid Data
    rho_o=920;                        %Oil density [kg/m³]
    rho_w=1000;                       %Water density [kg/m³]
    WC=0.8555;                        %Water cut [-]

    %Operational Parameters
    SPM=4.19;                         %Average pumping speed [spm]
    FL=827;                           %Dynamic fluid level [m]
    WHP=4E5;                          %Wellhead pressure [Pa]
    df=0.14;                          %Damping factor [-]
    tt=0.47;                          %Transition time [s]

    %Transition time is imported and depends on the instantaneous
    %pumping speed in the turning points

    %Parameter Calculation
    T=60/SPM;                         %Stroke cycle duration [s]
    Ar=dr^2*pi()/4;                   %Rod cross section area [m²]
    Ap=dp^2*pi()/4;                   %Plunger cross section area [m²]
    vs=sqrt(E/rho_st);                %Speed of sound in steel [m/s]
    rho_m=WC*rho_w+(1-WC)*rho_o;      %Fluid Mixture density [kg/m³]
    B=-(WHP+rho_m*9.81*L);            %Buoyancy [-]
    FW=(WHP+9.81*rho_m*FL)*(Ap-Ar);   %Fluid weight [N]

    %Time of the upstroke
    R=0.5;                            %For constant speed scenarios
    Tup=T*R;

    %For variable speed scenarios the upstroke ratio R is imported
    %from the optimization sheet

    %Element definition
    dx=50;                            %Space increment [m]
    dt=dx*0.5/a;                      %Time increment [s]
    m=round(L/dx);                    %Number of space increments
    n=round(T/dt);                    %Number of time increments
    Fg=wr*dx*9.81;                    %Weight of one rod section [N]
```

```
%Coefficient Definition
c1=pi()*df/2/L*a;
c2=vs^2;



%NUMERICAL SOLUTION OF THE WAVE EQUATION

%Definition of the time vector
t_v=zeros(1,n);

for j=1:n
    t_v(j)=dt*(j-1);
end

%Initial conditions
u=zeros(m,n);                   %Displacement [m]
F=zeros(m,n);                   %Load [N]

%Surface boundary condition
u(1,:)=polished_rod_position(T,n);

%Bottom boundary condition
PL=zeros(1,n);                  %Plunger load vector

for j=2:n
    t=t_v(j);
    dFW=(FW-B)/tt;
    if t<=tt
        PL(j)=dFW*t+B;
    elseif t<(Tup) && t>tt
        PL(j)=FW;
    elseif t>(Tup) && t<(Tup+tt)
        PL(j)=FW-dFW*(t-Tup);
    else
        PL(j)=B;
    end
end



%FINITE DIFFERENCE METHOD

%Displacement
for j=2:n-1
    for i=2:m-1
        if i==(m-1)
            u(i+1,j)=-PL(j)/E/Ar*dx+u(i,j);
        end
        u(i,j+1)=((c1*dt*dx^2*u(i,j)+dx^2*(2*u(i,j)-u(i,j-1))+
        c2*dt^2*(u(i+1,j)-2*u(i,j)+u(i-1,j)))/((1+c1*dt)*dx^2));
    end
end
```

```
    %Loads
    F(end,:)=PL;

    for i=1:m-1
        for j=1:n
            F(i,j)=(-u(i+1,j)+u(i,j))/dx*E*Ar;
        end
    end

    %Total Loads
    for i=1:m
        Ft(i,:)=F(i,:)+Fg*(m-i);
    end

    %Export of the polished rod loads
    t=transpose(t_v);
    xlswrite('WELL1.xlsx',t(:,1),'load','A3');
    PRL=transpose(Ft);
    xlswrite('WELL1.xlsx',PRL(:,1),'load','B3');

end



%IMPORT OF THE POLISHED ROD MOTION

function PR=polished_rod_position(T,n)

    PR=xlsread('WELL1.xlsx','crank_v','X18:X2951');

    %The polished rod position is imported for both constant
    %and variable speed scenarios

end
```

Appendix C

INPUT DATA

Strokes per minute:	4,2	Fluid level	
Run time (hrs/day):	24,0	(m from surface):	827
Tubing pres. (kPa):	400	(m over pump):	73
Casing pres. (kPa):	490	Stuf.box fr. (N):	445
		Pol. rod. diam.	1.5" (38.1 mm)

Fluid Properties		Motor & Power Meter	
Water cut:	85,6%	Power meter	Detent
Water sp. gravity:	1	Elect. cost:	$,3/KWH
Oil density (g/cm³):	0,92	Type:	NEMA D
Fluid sp. gravity:	0,9884	Size:	40 hp (29,42 KW)

CALCULATED RESULTS (TOTAL SCORE: 78% GRADE: B-)

Production rate (m³/D):	22	Peak pol. pod load (N):	45824
Oil production (m³/D):	3,2	Min. pol. rod load (N):	21551
Strokes per minute:	4,19	MPRL/PPRL:	0.47
System eff. (Motor->Pump):	26%	Unit struct. loading:	40%
Permissible Load Power (kW):	13	PRHP / PLHP:	0,34
Fluid load on pump (N):	12361	Buoyant rod weight (N):	27818
Pol. Rod Power (kW):	4,4	N/No: ,052 ,	Fo/SKr: ,036

Prime Mover Speed Variation
Speed variation not considered

Pumping Unit:Lufkin Conventional - New

API Size: C-320-256-144 (Unit ID: CL27)	
Crank hole number:	# 1 (out of 4)
Calculated stroke length (cm):	370,5
Crank rotation with well to right:	CCW
Max. cb moment (N-m):	53209
Structural unbalance (N):	-1779
Crank offset angle (degrees):	0,0

Torque analysis and electricity consumption

	BALANCED (Min. Energy)	BALANCED (Min Torq)	EXISTING
Peak g'box torq.(N-m):	27608	26154	35556
Gearbox loading:	76,4%	72,3%	98,3%
Cyclic load factor:	1,439	1,436	1,627
Max. cb moment (N-m):	62748,2	64865,73	53208,61
Counterbalance effect(N):	34311	35529	28824
Daily electr.use (Kwh/Day):	185	189	193
Monthly electric bill:	$1695	$1733	$1762
Electr.cost per m³ fluid:	$2,521	$2,577	$2,620
Electr.cost per m³ oil:	$17,445	$17,831	$18,129

Tubing And Pump Information

Tubing O.D. (mm):	73,025	Upstr. rod-tbg fr. coeff.:	0,800
Tubing I.D. (mm):	62,001	Dnstr. rod-tbg fr. coeff.:	0,800
Pump depth (m):	900	Tub.anch.depth (m):	900
Pump conditions:	Full	Pump load adj. (N):	0
Pump type:	Insert	Pump vol. efficiency:	66%
Plunger size (mm)	44,5	Pump friction (N):	890

Tubing, Pump And Plunger Calculations

Tubing stretch (cm):	,0
Prod. loss due to tubing stretch (m³/D):	,0
Gross pump stroke (cm):	357,9
Pump spacing (cm from bottom):	22,5
Minimum pump length (m):	4,9
Recommended plunger length (m):	,6

Rod string design / Rod string stress analysis (service factor: 0,9)

Diameter (mm)	Rod Grade	Length (m)	Min. Tensile Strength (kPa)	Stress Load %	Top Maximum Stress (kPa)	Top Minimum Stress (kPa)	Bot. Minimum Stress (kPa)	Stress Calc. Method
22.2	D (API)	879	792897	40.1%	116972	56697	1824	API MG
+# 50.8	Norris D (nn)	21	689476	4.7%	5914	-1356	-439	API MG

+requires slimhole couplings. sinker bar has no elevator neck.
NOTE: Displayed bottom minimum stress calculations do not include buoyancy effects (top minimum and maximum stresses always include buoyancy).

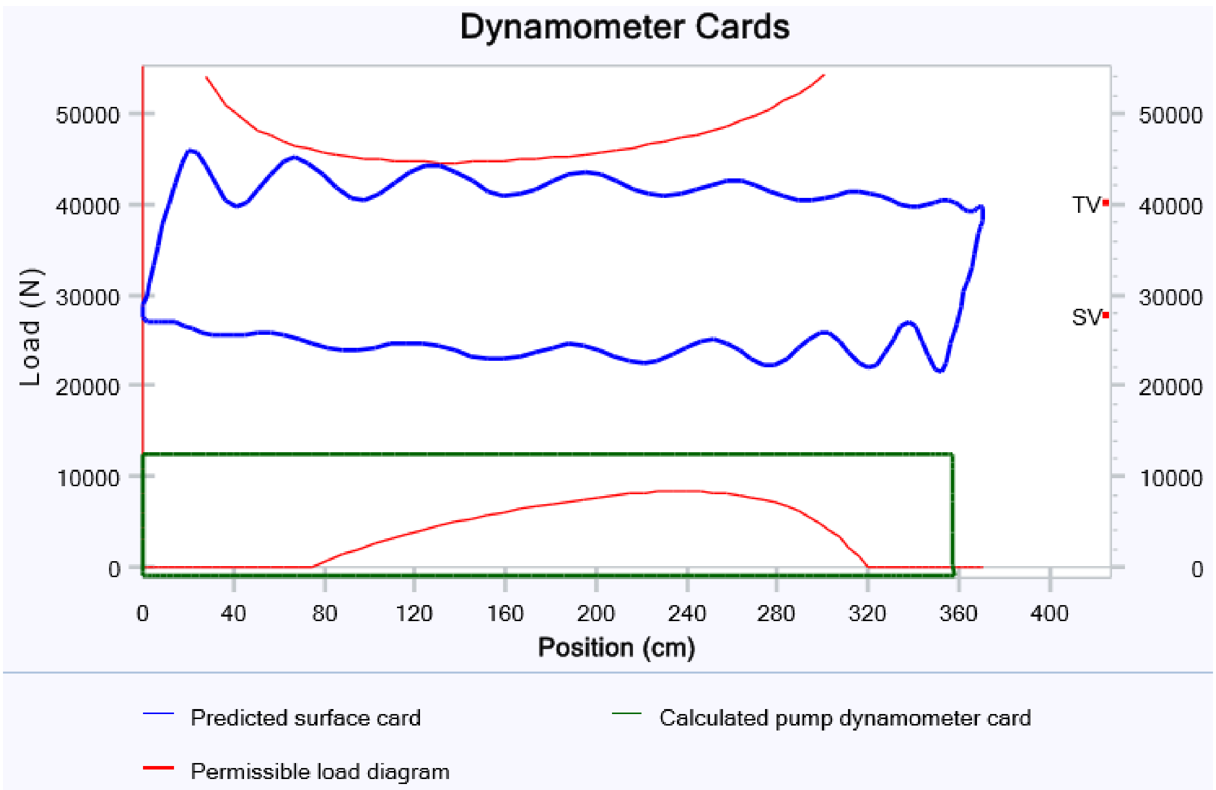

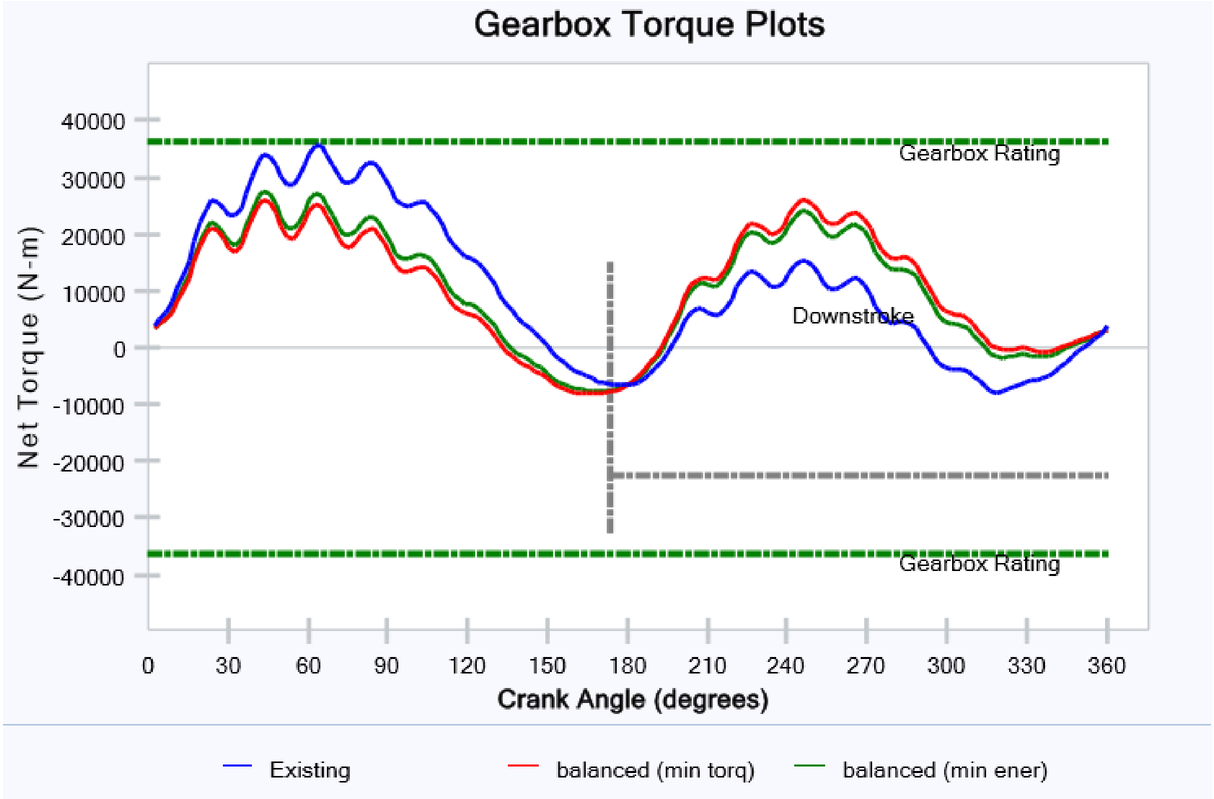
Gearbox Torque Plots
40000
30000
20000
10000
0
-10000
-20000
-30000
-40000
Net Torque (N-m)
Gearbox Rating
Downstroke
Gearbox Rating
0
30
60
90
120
150
180
210
240
270
300
330
360
Crank Angle (degrees)
Existing
balanced (min torq)
balanced (min ener)

Appendix D

```
%CALCULATION OF TORQUE AND POWER REQUIREMENTS IN MATLAB

%General Information
SPM=4.19;                              %Average Pumping speed [spm]
T=60/SPM;                              %Stroke cycle duration [s]
n=1000;                                %Number of data points
t_v=linspace(0,T,n);                   %Time vector
nsurf=0.765;                           %Surface efficiency [-]

%Definition of the output scenarios
Pmax=[];                               %Peak power [kW]
E_d=[];                                %Energy detent meter [kWh/h]
E_nd=[];                               %Energy nondetent meter [kWh/h]


%Import of the polished rod loads, crank velocity, crank
%acceleration, walking beam velocity and walking beam acceleration
t=xlsread('WELL1.xlsx','load','A3:A2936');
PRL=xlsread('WELL1.xlsx','load','B3:B2936');
theta2_p=xlsread('WELL1.xlsx','crank_v','AF18:AF2951') ;
theta2_pp=xlsread('WELL1.xlsx','crank_v','AG18:AG2951') ;
theta4_p=xlsread('WELL1.xlsx','crank_v','AH18:AH2951') ;
theta4_pp=xlsread('WELL1.xlsx','crank_v','AI18:AI2951') ;

%Interpolation of the crank velocity, crank acceleration, walking
beam velocity and walking beam acceleration
theta2_p_i=interp1(t,theta2_p,t_v,'linear','extrap');
theta2_pp_i=interp1(t,theta2_pp,t_v,'linear','extrap');
theta4_p_i=interp1(t,theta4_p,t_v,'linear','extrap');
theta4_pp_i=interp1(t,theta4_pp,t_v,'linear','extrap');

%Pumping unit dimensions
A = 4.57;
C = 3.05;
I = 3.05;
P = 3.67;
H = 6.6;
G = 2.82;
R = 1.19;
SU=-1780;
K=((H-G)^2+I^2)^0.5;
d=asin(I/K)-0.0405;
gamma=d-acos(((P+R)^2+K^2-C^2)/2/K/(R+P));

l_b=C+A;                               %Length of walking beam [m]
mb=260*l_b;                            %Mass of walking beam [kg]

l_p=P;                                 %Length of pitman [m]
mp=15*l_p*2;                           %Mass of pitman [kg]

l_e=1;                                 %Length of equalizer [m]
me=82*l_e;                             %Mass of equalizer [kg]
```

```
l_h=5;                                  %Distance horsehead to SB [m]
mh=(mb*(l_b/2-C)-B*A/9.81-
(me+mp)*C)/l_h;                         %Mass of horsehead [kg]

Mc=45000;                               %Moment of cranks [Nm]
l_c=2.3;                                %Length of cranks [m]
mc=Mc/9.81*2/l_c;                       %Mass of cranks [kg]


%Counterweight Installation
for kk=0:100

     l_cw=3;                            %Distance from CWs to GB [m]
     mcw=2*kk*20;                       %Variable mass of CWs [kg]

     %Inertial effects
     mo=mb+mh+me+mp/2;                  %Mass of oscillating parts [kg]
     Io=(me+mp/2)*C^2+mh*l_h^2+
     1/12*mb*l_b^2+mb*(l_b/2-C)^2;      %I of oscillating parts [kgm²]

     Mrot=Mc+mp/2*R*9.81;               %Moment of rotating parts [Nm]
     Irot=mp/2*R^2+1/3*mc*l_c^2;        %I of rot parts [kgm²]

     Mcw(kk+1)=mcw*9.81*(l_cw);         %Variable moment of CWs [Nm]
     Icw=mcw*(l_cw)^2;                  %I of CWs [kgm²]


     %Definition of the angular velocity vector
     omega_i=zeros(1,length(t_v));

     for k=1:length(t_v)-1
          omega_i(k+1)=omega_i(k)+theta2_p_i(k)*(t_v(k+1)-
          t_v(k))+theta2_pp_i(k)/2*(t_v(k+1)-t_v(k))^2;
     end


     %Calculation of the polished rod velocity and torque factor
     VR=A*theta4_p_i;
     TF=VR./theta2_p_i;


     %Interpolation of the polished rod loads
     omega=2*pi/T.*t(:,1);
     PRL_i= interp1(omega,PRL(:,1),omega_i);


     %Torque calculation
     Trod=-TF.*(PRL_i+SU);
     Tia=TF*Io/A.*theta4_pp_i;
     Tir=-Irot*theta2_pp_i-Icounter*theta2_pp_i;
     Tcb=-(Mcounter(kk+1)+Mrot)*sin(omega_i-gamma);
     Tnet(kk+1,:)=Trod+Tcb+Tir+Tia;
```

```
      %Power requirement
      for i=1:n
            Power(i)=Tnet(kk+1,i)*omega_i(i)/nsurf;
      end

      %Peak power
      Pmax(kk+1)=max(Power)/1000;


      %Energy consumption with a detent meter
      sumE_d=0;

      for i=1:length(Power)-1
            if Power(i)>0
                  sumE_d=sumE_d+Power(i)*T/n;
            end
      end

      E_d(kk+1)=sumE_d*SPM*60*2.778*10^-7;


      %Energy consumption with a non-detent meter
      sumE_nd=0;

      for i=1:length(Power)-1
            sumE_nd=sumE_nd+Power(i)*T/n;
      end

      E_nd(kk+1)=sumE_nd*SPM*60*2.778*10^-7;

end



%SIMULATION SCENARIOS

%Minimum peak torque/power scenario
[c,d]=min(Pmax);

Mcb_min_T=(Mcw(d)+Mrot)
Pmax_min_T=c
E_min_T=E_d(d)

%Minimum energy scenario
[a,b]=min(E_d);

Mcb_min_E=(Mcw(b)+Mrot)
Pmax_min_E=Pmax(b)
E_min_E=a

%Energy recovery scenario
E_rec=min(E_nd)
```

Appendix E

Maximum Stress in the V-Belt

ConCar Power Band
DIN 7753-1 SPC 22

V-Belt Drive Characteristics			Power Band Properties			Calculated Values		
d_{PM}	240	mm	ρ_B	1200	kg/m³	μ'	1.71	-
d_{GB}	1130	mm	E_B	300	N/mm²	β_1	147.70	°
e	1.6	m	A_B	267.75	mm²	F_{b1}	1606.50	N
φ	34	°	t_B	4.8	mm	$(F_1'+F_c)_{max}$	2290.62	N
L_B	5.6	m	μ	0.5	-	σ_{max}	14.56	N/mm²

Time [s]	T_{net} [Nm]	T_{mot} [Nm]	N [spm]	N_{mot} [rpm]	BV [m/s]	F_1' [N]	F_c [N]	F_1+F_c [N]
0.00	5227.04	40.95	2.338	331.63	4.17	345.48	5.58	351.06
0.01	5256.68	41.19	2.339	331.64	4.17	347.44	5.58	353.02
0.03	5286.45	41.42	2.339	331.67	4.17	349.41	5.58	354.99
0.04	5316.42	41.65	2.339	331.72	4.17	351.39	5.58	356.98
0.06	5346.53	41.89	2.340	331.79	4.17	353.38	5.59	358.97
0.07	5376.79	42.13	2.340	331.88	4.17	355.38	5.59	360.97
0.09	5407.24	42.37	2.341	331.99	4.17	357.40	5.59	362.99
0.10	5437.88	42.61	2.342	332.13	4.17	359.42	5.60	365.02

...

2.52	33085.22	259.22	3.976	563.82	7.09	2186.79	16.13	2202.92
2.54	33373.35	261.48	3.988	565.61	7.11	2205.83	16.23	2222.06
2.55	33627.28	263.47	4.001	567.40	7.13	2222.62	16.33	2238.95
2.57	33713.77	264.15	4.014	569.18	7.15	2228.33	16.44	2244.77
2.58	33730.88	264.28	4.026	570.96	7.17	2229.46	16.54	2246.00
2.59	33809.47	264.89	4.039	572.73	7.20	2234.66	16.64	2251.30
2.61	33940.34	265.92	4.051	574.49	7.22	2243.31	16.75	2260.05
2.62	34075.17	266.98	4.063	576.24	7.24	2252.22	16.85	2269.07
2.64	34229.18	268.18	4.076	577.99	7.26	2262.40	16.95	2279.35
2.65	34369.96	269.29	4.088	579.72	7.29	2271.70	17.05	2288.76
2.67	34396.55	269.49	4.100	581.45	7.31	2273.46	17.15	2290.62
2.68	34384.41	269.40	4.112	583.17	7.33	2272.66	17.26	2289.91
2.69	34378.39	269.35	4.124	584.88	7.35	2272.26	17.36	2289.62
2.71	34240.82	268.27	4.136	586.59	7.37	2263.17	17.46	2280.63
2.72	33926.54	265.81	4.148	588.28	7.39	2242.40	17.56	2259.96
2.74	33486.85	262.37	4.160	589.97	7.41	2213.33	17.66	2230.99
2.75	32996.04	258.52	4.172	591.64	7.43	2180.89	17.76	2198.65
2.77	32567.83	255.17	4.184	593.31	7.46	2152.59	17.86	2170.45
2.78	32206.78	252.34	4.195	594.96	7.48	2128.73	17.96	2146.69
2.80	31848.12	249.53	4.207	596.61	7.50	2105.02	18.06	2123.08
2.81	31462.76	246.51	4.218	598.24	7.52	2079.55	18.16	2097.71
2.82	31054.56	243.31	4.230	599.87	7.54	2052.57	18.26	2070.83
2.84	30634.87	240.02	4.241	601.48	7.56	2024.83	18.36	2043.19
2.85	30313.17	237.50	4.253	603.08	7.58	2003.57	18.45	2022.02

...

Appendix F

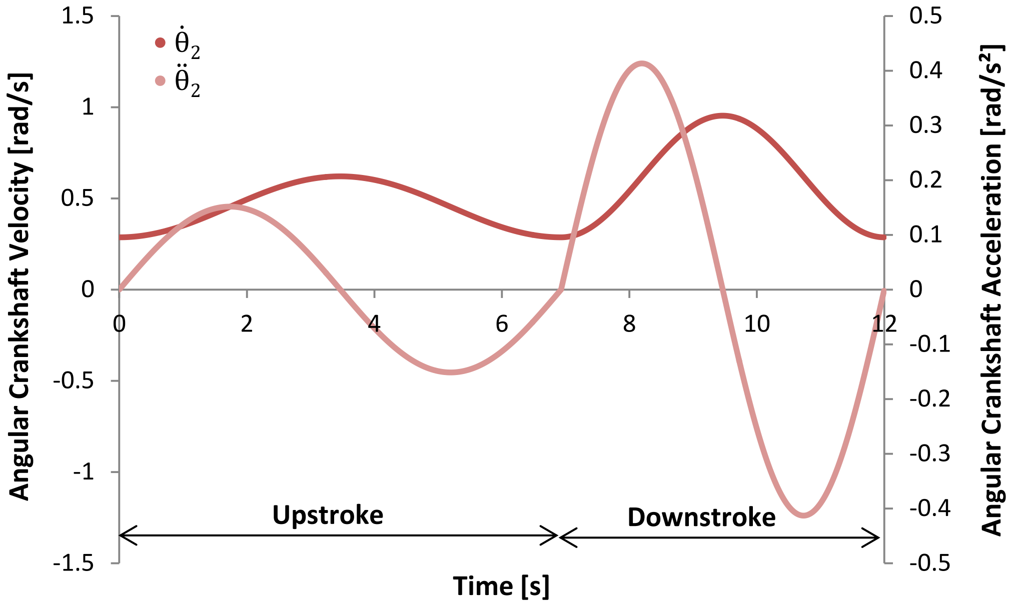

Figure 71: Scenario A: Angular Crank Velocity and Acceleration of the VarLoad Case

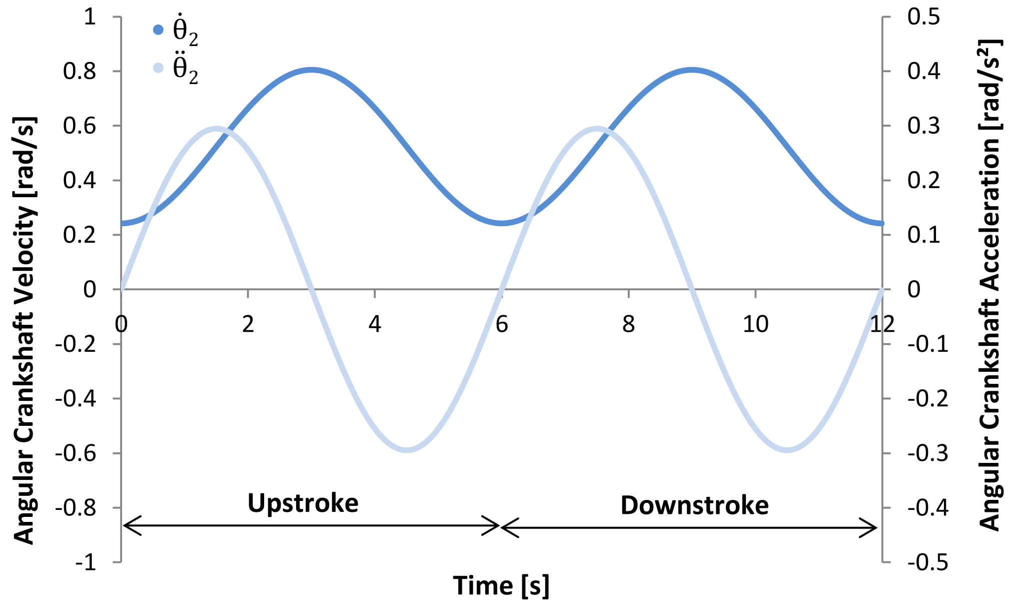

Figure 72: Scenario A: Angular Crank Velocity and Acceleration of the VarEnergy Case

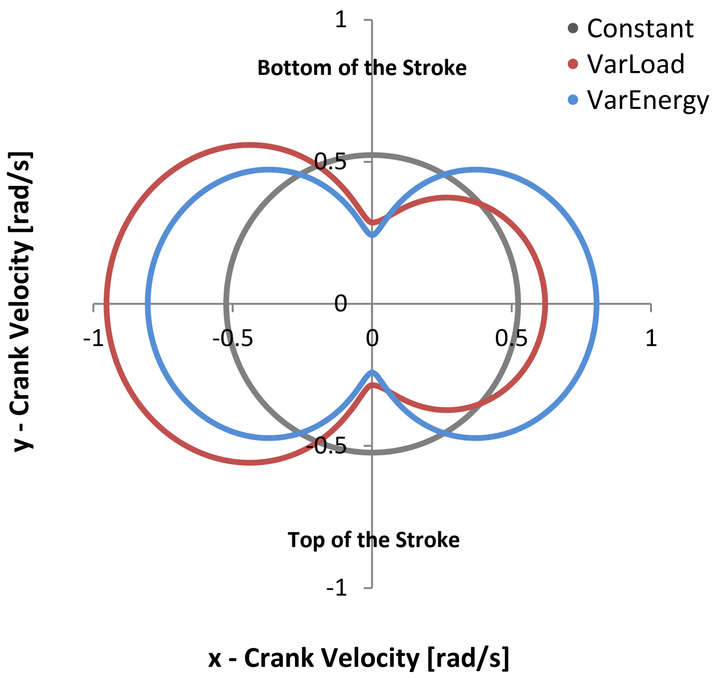

Figure 73: Scenario A: Comparison of the Angular Crank Velocity on a Radial Diagram

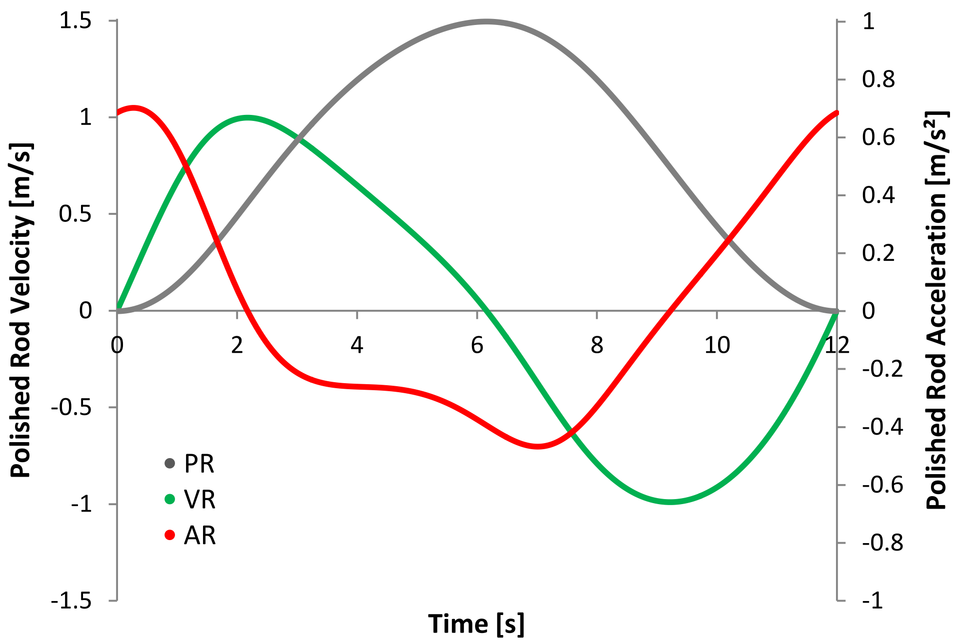

Figure 74: Scenario A: Polished Rod Motion of the Constant Case

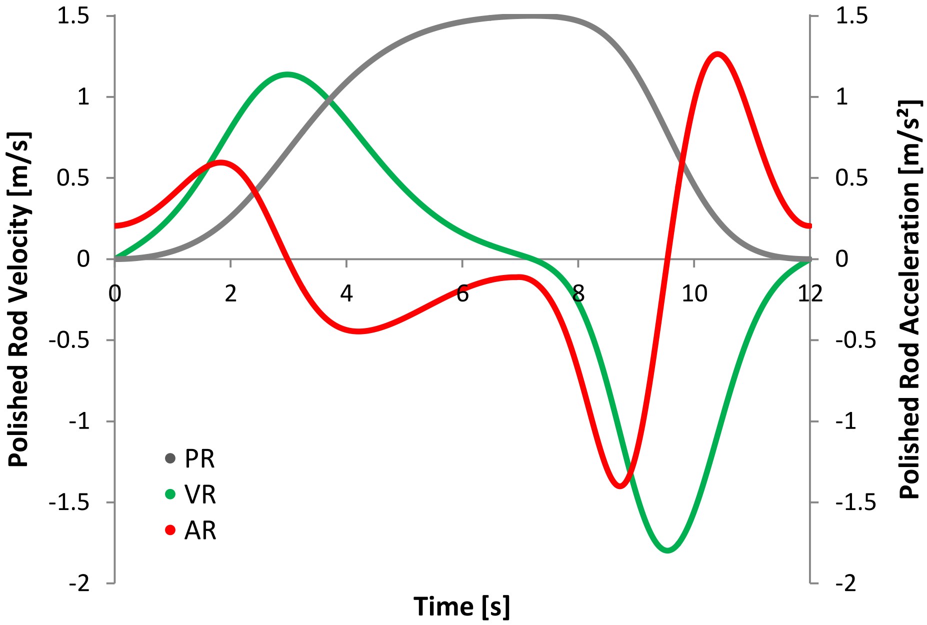

Figure 75: Scenario A: Polished Rod Motion of the VarLoad Case

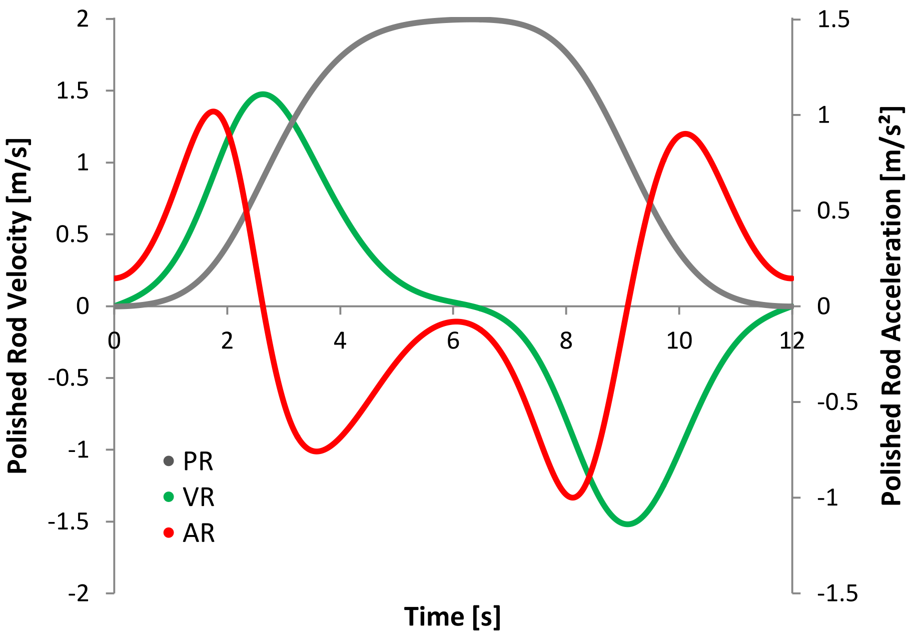

Figure 76: Scenario A: Polished Rod Motion of the VarEnergy Case

Appendix G

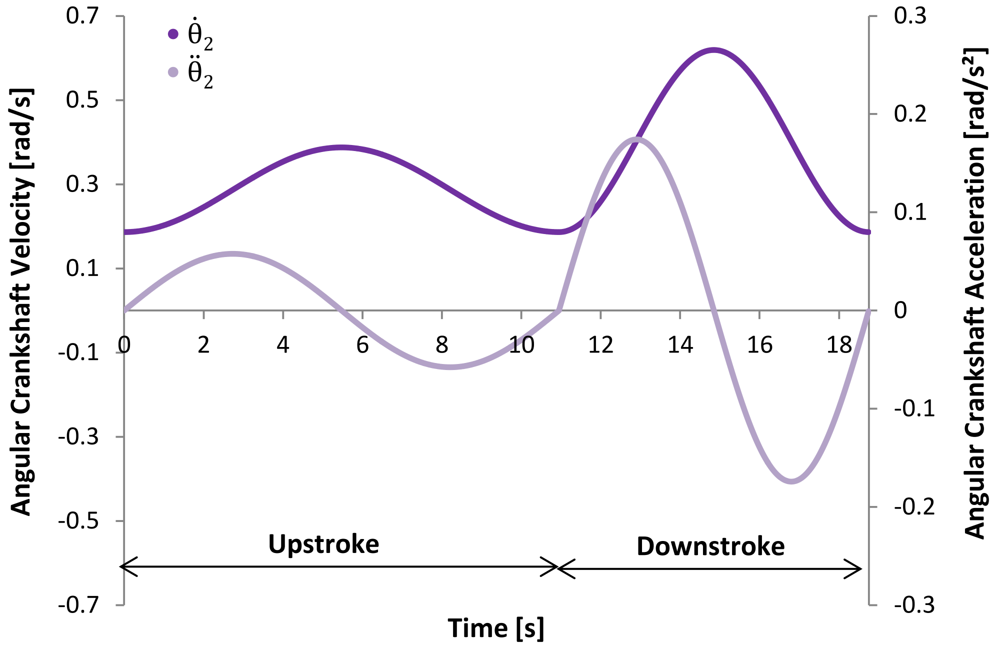

Figure 77: Scenario B: Angular Crank Velocity and Acceleration of the VarLoad/E Case

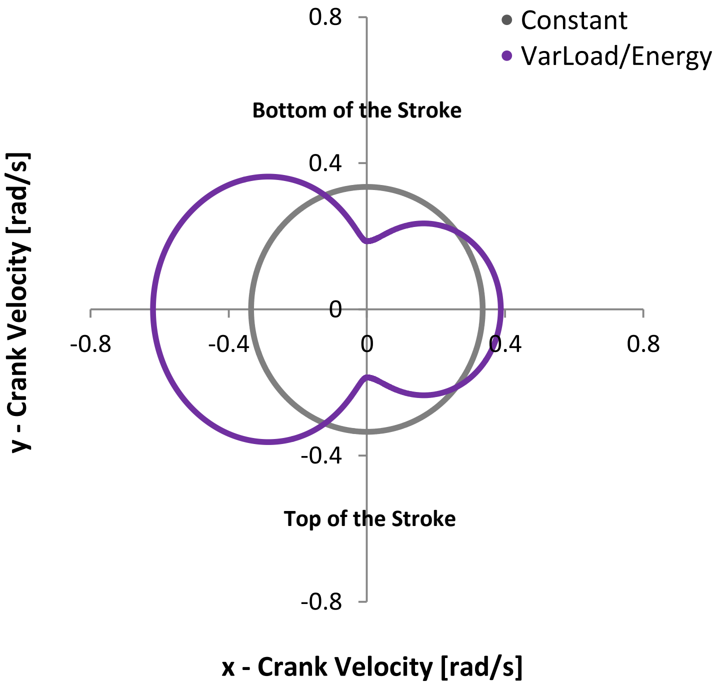

Figure 78: Scenario B: Comparison of the Angular Crank Velocity on a Radial Diagram

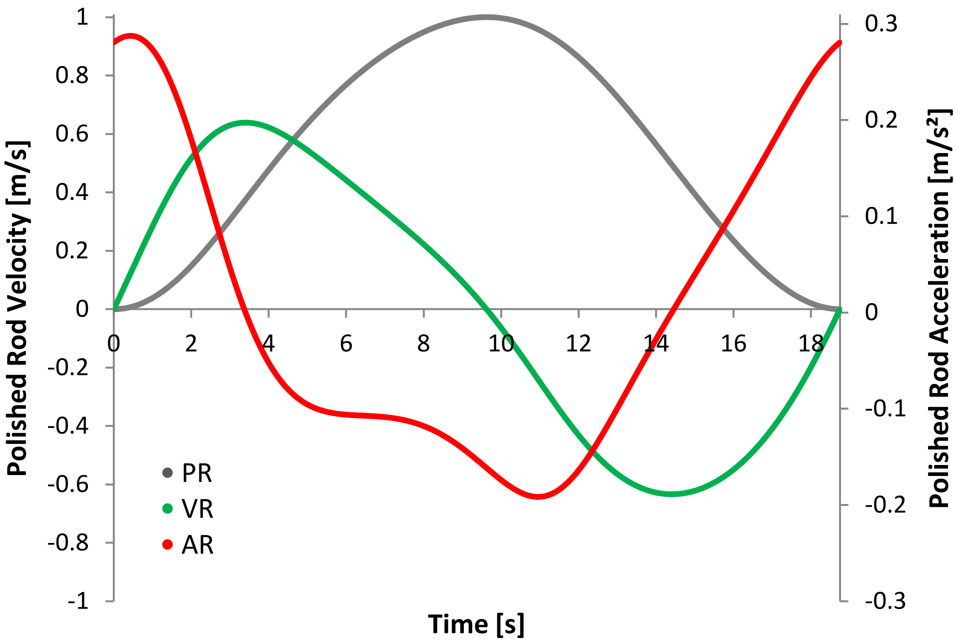

Figure 79: Scenario B: Polished Rod Motion of the Constant Case

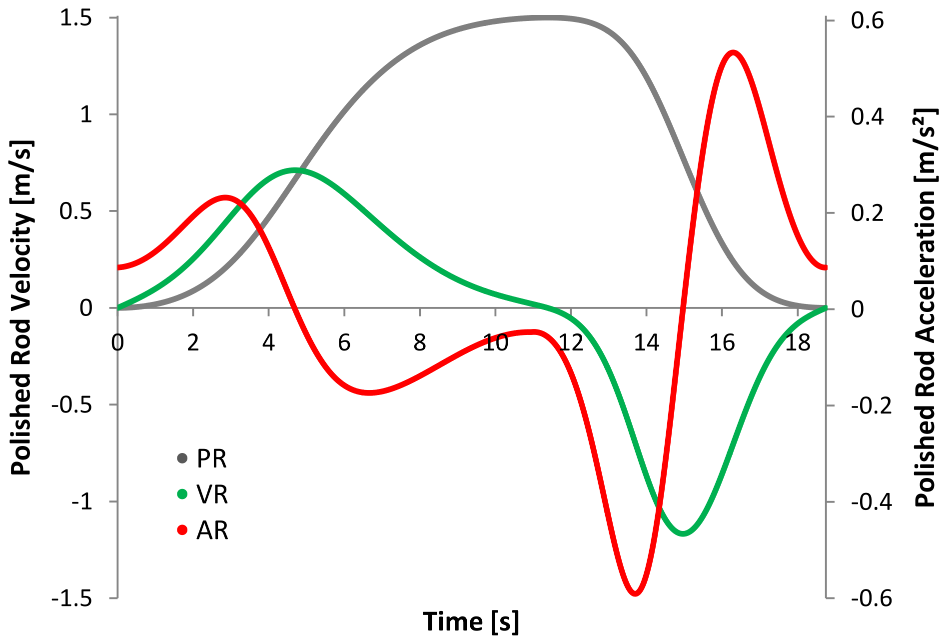

Figure 80: Scenario B: Polished Rod Motion of the VarLoad/Energy Case

Appendix H

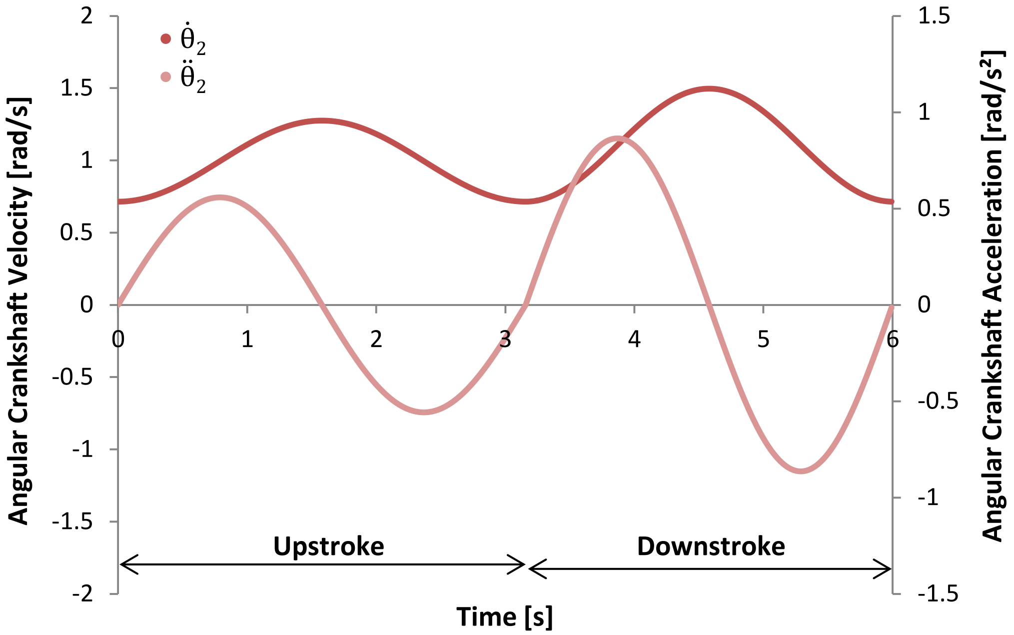

Figure 81: Scenario C: Angular Crank Velocity and Acceleration of the VarLoad Case

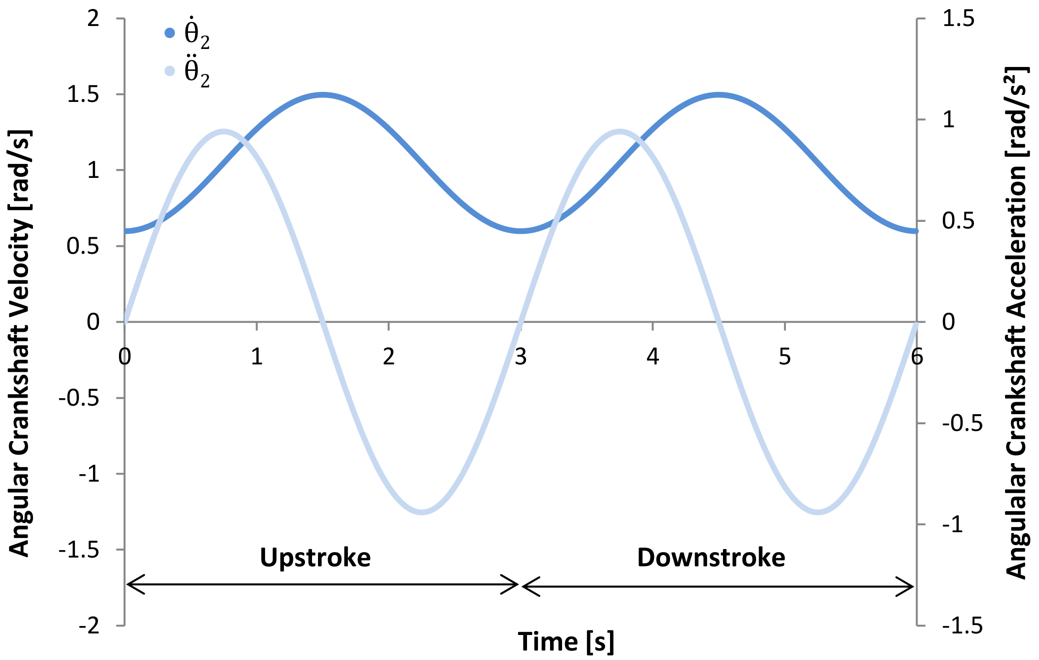

Figure 82: Scenario C: Angular Crank Velocity and Acceleration of the VarEnergy Case

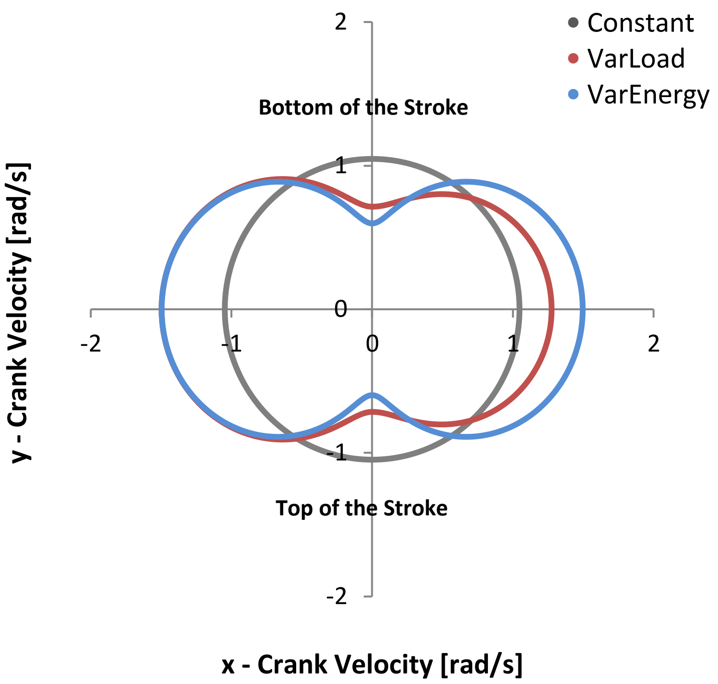

Figure 83: Scenario C: Comparison of the Angular Crank Velocity on a Radial Diagram

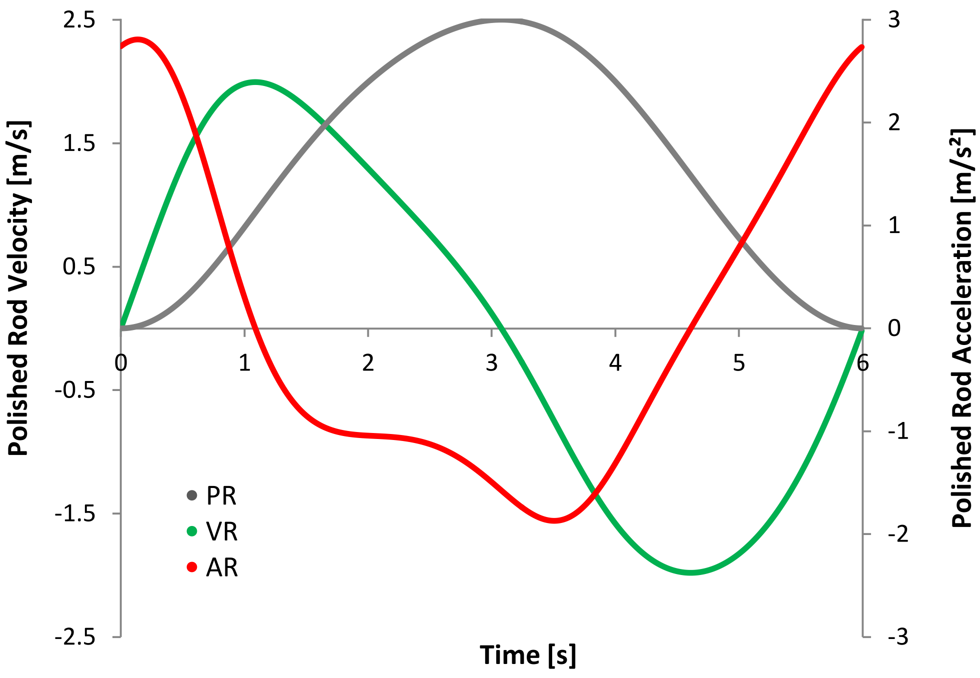

Figure 84: Scenario C: Polished Rod Motion of the Constant Case

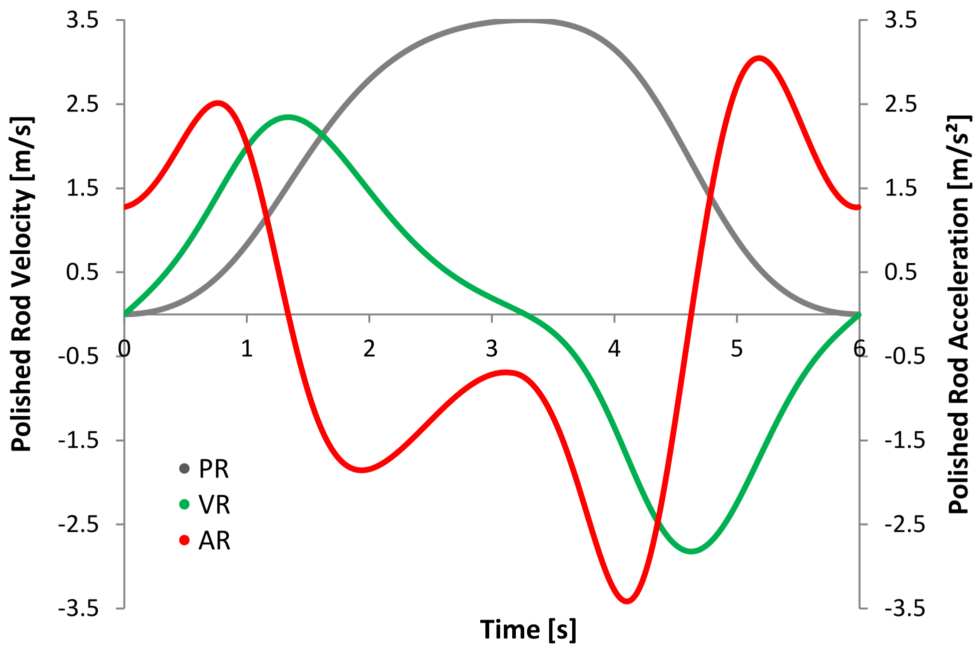

Figure 85: Scenario C: Polished Rod Motion of the VarLoad Case

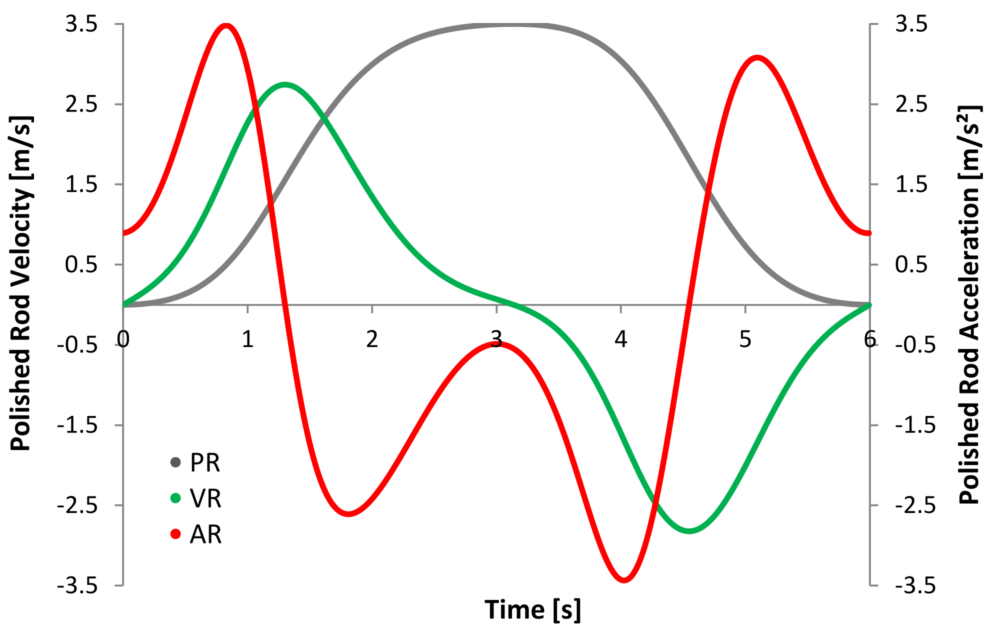

Figure 86: Scenario C: Polished Rod Motion of the VarEnergy Case

Appendix I

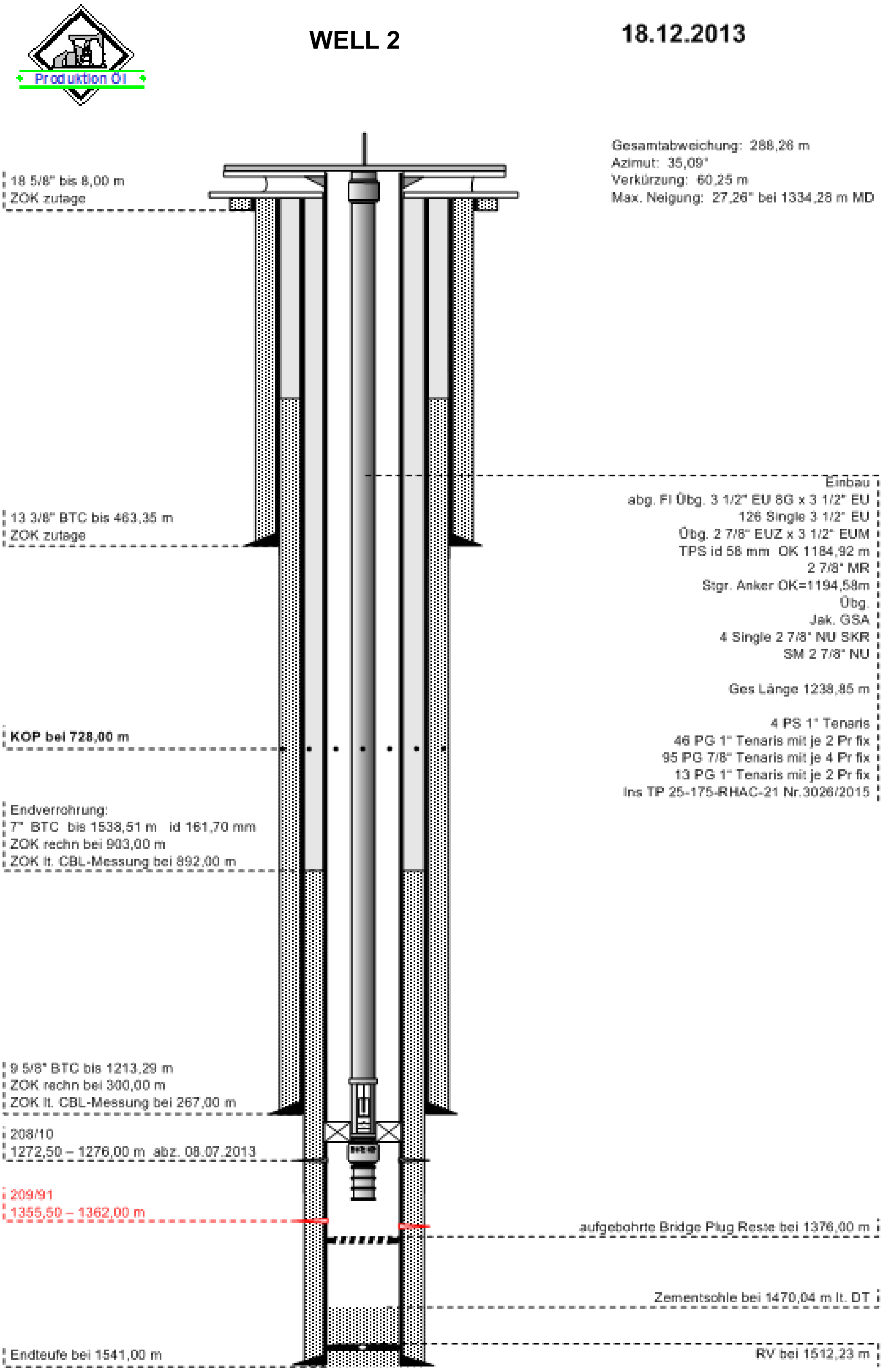

Figure 87: Wellbore Schematic of Well 2

Appendix J

Table 30: Operational Data of Well 2 [30]

Date	Frequency [%]	Pumping Speed [spm]
18.02.2016	10.03	1.3
19.02.2016	20.33	2.63
22.02.2016	23.23	3.01
23.02.2016	25.46	3.3
29.02.2016	25.42	3.29
01.03.2016	29.42	3.81
02.03.3016	30.38	3.94
06.03.2016	30.37	3.93
07.03.2016	33.98	4.4
08.03.2016	35.1	4.55
04.04.2016	28.85	3.74
06.04.2016	34.54	4.47
07.04.2016	33.16	4.3
08.04.2016	35.56	4.61
11.04.2016	34.34	4.45
31.05.2016	30.11	3.9
02.06.2016	35.47	4.59
02.07.2016	33.95	4.4

Table 31: Production Data of Well 2 [30]

Date	Daily Production [m³]	Water Cut [%]
18.02.2016	22	100
19.02.2016	22.1	99.26
21.02.2016	22	93.76
25.02.2016	26.7	88.29
10.03.2016	37	87.31
25.03.2016	37.8	86
08.04.2016	37.7	87
28.04.2016	37	87.07
23.05.2016	38.1	87.51
01.06.2016	28.6	87.52
02.06.2016	38.1	87.51
16.06.2016	38.8	87.85
06.07.2016	37.2	88.18
24.07.2016	38.7	87.28

Appendix K

Design of the Start-up Ramp

Input Parameters			Wellbore Completion			Calculated Values		
N_{min}	2.5	spm	D_{rod1}	25.4	mm	V_{Step1}	27.60	m³
N_{des}	4.59	spm	D_{rod2}	22.2	mm	t_{Step1}	33	hours
L_{dyn}	652	m	ID_{csg}	161.7	mm	$\approx t_{Step1}$	2	days
WC	87.65	%	OD_{tbg}	88.9	mm	cor. V_{Step1}	40.15	m³
Q_{tot}	36.85	m³/day	ID_{tbg}	76.0	mm	V_{Step2}	557.41	m³
S_{eff}	4.13	m	L_{rod1}	484	m	t_{Step2}	467	hours
η_{pump}	87	%	L_{rod2}	777	m	t_{Step2}	20	days
t_{Start}	22	days	L_{csg}	1470	m	ΔN_{Step2}	0.1	spm/day
V_{start}	597.55	m³	L_{tbg}	1239	m	t_{Start}	22	days

Operational Data

Month		Monthly Production		Cumulative Production	
February	2016	385.1	m³	385.1	m³
March	2016	1060.0	m³	1445.1	m³
April	2016	1130.2	m³	2575.3	m³
May	2016	1157.5	m³	3732.8	m³